Investigations of $1/f$ flux noise in superconducting quantum circuits

by

Steven L. Sendelbach

A dissertation submitted in partial fulfillment of
the requirements for the degree of

Doctor of Philosophy

(Physics)

at the

UNIVERSITY OF WISCONSIN–MADISON

2013

Date of final oral examination: December 19, 2012

The dissertation is approved by the following members of the Final Oral Committee:
Robert F. McDermott, Associate Professor, Physics
Mark A. Eriksson, Professor, Physics
Mark Rzchowski, Professor, Physics
Maxim G. Vavilov, Associate Professor, Physics
Chang-Beom Eom, Professor, Materials Science and Engineering

UMI Number: 3549802

All rights reserved

INFORMATION TO ALL USERS
The quality of this reproduction is dependent upon the quality of the copy submitted.

In the unlikely event that the author did not send a complete manuscript
and there are missing pages, these will be noted. Also, if material had to be removed,
a note will indicate the deletion.

UMI 3549802

Published by ProQuest LLC (2013). Copyright in the Dissertation held by the Author.

Microform Edition © ProQuest LLC.
All rights reserved. This work is protected against
unauthorized copying under Title 17, United States Code

ProQuest LLC.
789 East Eisenhower Parkway
P.O. Box 1346
Ann Arbor, MI 48106 - 1346

ACKNOWLEDGMENTS

It is a pleasure to take a few paragraphs to thank some of the people who have made this thesis possible.

My greatest debt of gratitude is owed to my Ph.D. advisor, Robert McDermott. He was always very willing and able to explain every detail of the project. His style of leadership by example was also very patient and effective. It is difficult to underestimate how much I learned from him; I could not have asked for a better advisor.

I would also like to thank my student colleagues who all made the graduate experience much more enjoyable and fulfilling. I would like to especially like to thank David Hover who has been with me since the beginning. Always there for commiserating about life or a quick qubit tutorial I am not sure what I would have done without him.

I would also like to thank my family. My parents, Lee and JoLee Sendelbach, were very supportive throughout. However busy she may be, my mother was always available to listen to problems or successes and offer advice. I would also like to thank my wife Amanda for her patience during the thesis writing process and for pretending to enjoy a few date nights in the lab. Her help was more valuable than she knows.

Contents

ABSTRACT

We have performed experiments to uncover the source of excess low frequency flux noise in superconducting circuits. We report measurements of the temperature dependence of the quasistatic flux in SQUID circuits demonstrating a high density, $\approx 5 \times 10^{17}/\mathrm{m}^2$, of unpaired spins on the superconductor surface. We have also characterized the temperature dependent susceptibility of the surface spins. The susceptibility fluctuates with a $1/f$ spectrum and the fluctuations are correlated with the flux noise. Finally, we describe experiments that, for the first time, demonstrate a reduction in flux noise magnitude by engineering the metal-dielectric interface.

Chapter 0

Introduction

This study of $1/f$ flux noise occurs in the context of efforts to develop superconducting quantum computers. A superconducting qubit is like a macroscopic artificial atom with discrete energy levels that can be addressed by microwaves to drive transitions between states. Many important features of quantum computing have already been demonstrated in these systems, including the generation and manipulation of superposition states, the violation of Bell's inequality [1], and an implementation of Shor's algorithm [2]. Recent advances in error correcting codes for quantum computation have demonstrated a practical way to allow a large number of qubits to compensate for poor coherence time as long as individual qubits can operate above some error threshold [3]. Still, the number of physical qubits that is needed to make one logical qubit scales inversely with decoherence time. It has been shown that low frequency $1/f$ flux noise is a dominant source of decoherence in phase, flux, and transmon types of qubits [4, 5]. Because these are among the most promising candidates for scalable quantum computers, much effort has been directed at developing materials and methods to try to understand and eliminate sources of $1/f$ flux noise.

$1/f$ noise refers to a random process whose power spectral density, $S(f)$, shows an increase in power at low frequencies, which follows a $1/f^{\alpha}$ law with $\alpha \approx 1$. It is also referred to as

flicker noise or pink noise. $1/f$ noise is surprisingly common in physical systems. It has been observed not only in condensed matter systems, such as transistors and metallic thin films, but also in annual rainfall statistics, traffic flow, and even flood levels of the Nile river [6, 7]. $1/f$ noise has eluded attempts at a general explanation. Each source has a separate and system-dependent description.

A pioneering study of flux noise in superconducting circuits was conducted by Wellstood *et al.* in the late 1980s [8]. This group focused on SQUIDs with the intent of creating an exquisitely sensitive amplifier for the readout of Weber bars for gravity wave detection. Several noise sources had been identified in SQUIDs cooled to mK temperatures [9]. The white noise of the device decreased with decreasing temperature; however, an excess low frequency noise, which showed a $1/f$ spectrum at low frequency, did not decrease significantly with temperature in the accessible range, nor was it possible to eliminate by any modulation scheme. The flux noise power magnitude showed very little variation with the materials, temperature, or geometry of the devices, and no microscopic explanation of the noise mechanism or source was identified. Since that time, this has remained an open problem in condensed matter physics.

The SQUIDs studied by Wellstood and the qubits fabricated today have a lot in common. In particular, they are both thin film devices made from superconducting material with the Josephson junction as the crucial nonlinear element. They are also both sensitive to flux noise. Qubits, however, operate in a much narrower range of temperatures and materials; thus, for the purposes of studying flux noise, the SQUID is the preferred platform.

In the experiments described here, we demonstrate for the first time the existence of a high density $5 \times 10^{17}/\mathrm{m}^2$ of magnetic defect states residing on or near the surface of superconducting thin film devices. It is now believed that the excess low frequency flux noise is due to fluctuations of these surface spins.

We also describe measurements on the fluctuations of the spin susceptibility in time.

The susceptibility fluctuations show a $1/f$ spectrum at low frequency and are correlated at low temperature with the fluctuations in the flux. The susceptibility is also recorded as a function of temperature, showing large jumps at discrete temperatures. These data highlight possible interactions between the spins and guide the development of improved theoretical models of the flux noise.

Finally, we demonstrate a significant reduction in low frequency flux noise power by engineering the interface between the superconducting metal of the SQUID washer and the encapsulating dielectric material. SQUID devices that are encapsulated in silicon nitride show a greater than factor 20 reduction in flux noise power compared to conventional oxide encapsulated devices. The residual noise appears to be due to the small fraction of the SQUID loop that is unencapsulated. We expect that this reduction in flux noise power will improve qubit decoherence times by more than a factor of 4. Such an improvement would represent a major step forward toward scalable superconducting qubit technology.

Bibliography

[1] M. Ansmann, H. Wang, R. Bialczak, M. Hofheinz, E. Lucero, M. Neeley, A. O'Connell, D. Sank, M. Weides, J. Wenner, A. Cleland, and J. Martinis, Nature **461**, 504 (2009).

[2] E. Lucero, R. Barends, Y. Chen, J. Kelly, M. Mariantoni, A. Megrant, P. OMalley, D. Sank, A. Vainsencher, J. Wenner, T. White, Y. Yin, A. Cleland, and J. Martinis, Nature Physics (2012).

[3] A. G. Fowler, M. Mariantoni, J. Martinis, and A. N. Cleland, Phys. Rev. A **86**, 032324 (2012).

[4] F. Yoshihara, K. Harrabi, A. Niskanen, Y. Nakamura, and J. Tsai, Phys. Rev. Lett. **97**, 167001 (2006).

[5] R. Bialczak, R. McDermott, M. Ansmann, M. Hofheinz, N. Katz, E. Lucero, M. Neeley, A. O'Connell, H. Wang, A. Cleland, and J. Martinis, Phys. Rev. Lett. **99**, 187006 (2007).

[6] M. Keshner, Proceedings of the IEEE **70**, 212 (1982).

[7] B. R. Frieden and R. J. Hughes, Phys. Rev. E **49**, 2644 (1994).

[8] F. Wellstood, C. Urbina, and J. Clarke, Appl. Phys. Lett. **50**, 772 (1987).

[9] J. Clarke, Proceedings of the IEEE **77**, 1208 (1989).

Chapter 1

Superconducting qubit fundamentals

A superconducting qubit logically behaves similar to a superconducting anharmonic resonator. Thanks to the low loss of the superconductor, the system will behave quantum mechanically with discrete energy levels that can exist in superposition states, provided the thermal energy is smaller than the smallest energy needed to excite the oscillator ($k_B T << \hbar\omega_0$). A qubit needs two quantum states to represent the logical 0 and 1 states of the computer. A harmonic oscillator has plenty of states but each state is at a harmonic, or integer multiple, of the fundamental frequency ω_0. This means it is impossible to address only the 0 and 1 states with an excitation at ω_0 without exciting other states. In order to make a qubit, the 0 and 1 states must be isolated from the higher energy states. For that, an anharmonic resonator is required. Thankfully, nature has provided us with a lossless element with a nonlinear inductance, the Josephson junction. The Jospehson junction is the crucial ingredient to making an anharmonic superconducting resonator, and therefore, a qubit.

The Josephson junction is generally two superconducting reservoirs separated by a weak link through which Cooper pairs are able to tunnel. Typically, this is realized by controlling an oxidation of an aluminum thin film to a thickness of ~ 1 nm followed by growing a second thin film, which creates an Al-AlOx-Al junction. The governing equations for the Josephson

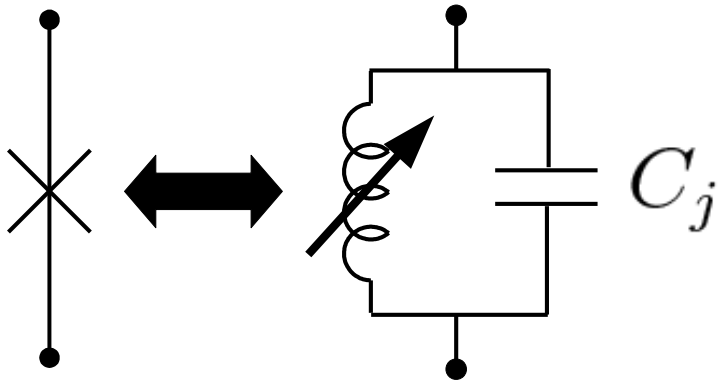

Figure 1.1: A current biased Josephson junction behaves like a parallel LC resonator with an adjustable inductance.

junction are [1]

$$I = I_0 \sin\delta \tag{1.1a}$$

$$V = \frac{\Phi_0}{2\pi}\frac{d\delta}{dt}, \tag{1.1b}$$

where I_0 is the junction critical current, δ is the superconducting phase difference across the junction, and Φ_0 is the magnetic flux quantum ($\Phi_0 \equiv h/2e \approx 2.068 \times 10^{-15}$ Tm^2).

If we differentiate the dc Josephson relation (1.1a) and merge with the ac relation (1.1b), we can write an equation for the effective inductance L_J of the junction as follows:

$$L_J = \frac{\Phi_0}{2\pi I_0 \cos\delta}. \tag{1.2}$$

The inductance is strongly non-linear, diverging near $\cos\delta = 0$. Because of the structure of the junction itself, there is also a capacitance in parallel with the inductance. A single junction biased with a current below the critical current forms a non-linear LC resonator, which can be made into a qubit.

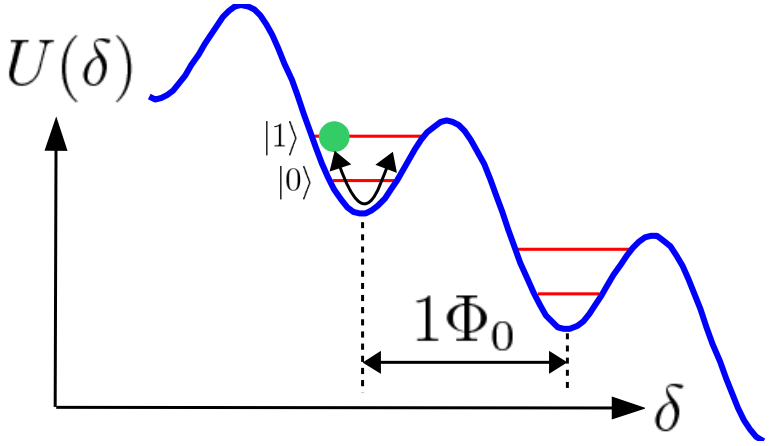

Figure 1.2: Tilted washboard potential. Shown are the first two oscillator states in the local minima with a phase particle oscillating back and forth.

1.1 Qubit operating principles

The quantum mechanical nature of the current biased Josephson junction was established in experiments in the 1980s involving measurements of the escape rate of a junction from its zero voltage state [2]. To understand the operation of a qubit, it is useful to consider the dynamics of the junction.

By setting the current through the junction equal to an applied bias current I and eliminating V in favor of δ using the Josephson relations (1.1), we obtain a differential equation for δ:

$$C\left(\frac{\Phi_0}{2\pi}\right)^2 \ddot{\delta} + \frac{\partial U(\delta)}{\partial \delta} = 0 \tag{1.3}$$

where

$$U(\delta) = -(I_0\Phi_0/2\pi)[\cos\delta + (I/I_0)\delta]. \tag{1.4}$$

This equation is recognized as being the same as the equation of motion for a particle of mass $C(\Phi_0/2\pi)^2$ traveling in the potential $U(\delta)$. The potential has the form of a tilted washboard with the cos term providing the periodic ridges and the current bias providing the slope (Figure 1.2). When cooled to a sufficiently low temperature, the phase particle can

settle into a local minimum where the dynamics of the system are analogous to a harmonic oscillator with discrete energy levels, except the energy difference between the levels are not all equal. It is in this regime where the qubit resides. The qubit 0 and 1 states are mapped to the ground state and the first excited state of the nonlinear oscillator and transitions can be stimulated by excitations with the right energy, E_{10}.

This correspondence is not only useful for intuitively understanding the junction dynamics, but also for transforming the equations into a quantum mechanical model. The velocity of the phase particle is $\dot{\delta}$, and the kinetic energy has a simple form in terms of the charge Q across the junction. $KE = \frac{1}{2C}Q^2$. Thus the Hamiltonian of the junction has the form [3]:

$$H = \frac{1}{2C}\hat{Q}^2 - \frac{I_0\Phi_0}{2\pi}\cos\hat{\delta} - \frac{I\Phi_0}{2\pi}\hat{\delta}. \tag{1.5}$$

The quantization is described by the commutation relation between $\hat{Q}$ and $\hat{\delta}$, which are analogous once again to the momentum and position of an oscillator with the result $[\hat{Q}, \hat{\delta}] = 2ei$.

The simple current biased Josephson junction qubit described above is not used in practice due to excessive quasiparticle generation during the measurement. Current designs of the phase qubit incorporate the junction into a superconducting loop, and a flux is used to current bias the junction. [4, 5]. Loops are also inherent in the design of flux qubits [6]. In this case, the Hamiltonian for the circuit becomes:

$$H = \frac{1}{2C}\hat{Q}^2 + \frac{1}{2L}\left(\Phi_b - \frac{\Phi_0}{2\pi}\hat{\delta}\right)^2 - \frac{I_0\Phi_0}{2\pi}\cos\hat{\delta}. \tag{1.6}$$

This loop makes these devices susceptible to flux noise. The flux noise is transformed into a current noise through the loop inductance.

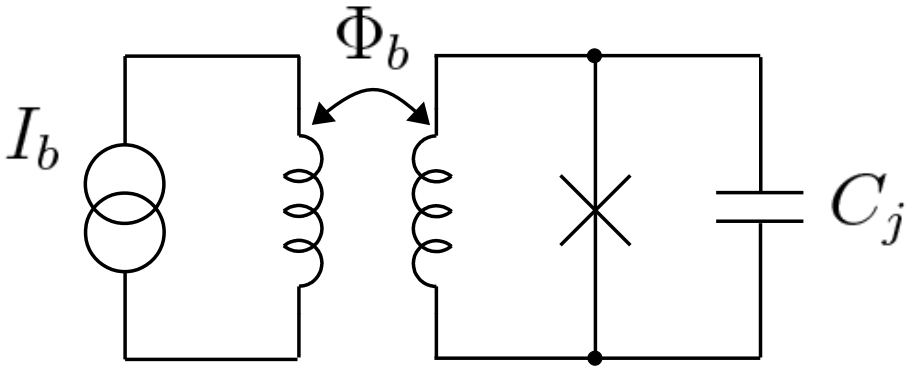

Figure 1.3: Schematic diagram for a flux biased phase qubit.

1.1.1 Qubit control

The state of a qubit is often represented by the position of a vector on a sphere called the Bloch sphere. The $|0\rangle$ state is on the south pole, the $|1\rangle$ state is on the north pole, and an equal superposition is on the equator.

Using a qubit for computations implies the ability to control and measure the position of this vector. Control in the phase qubit presents itself in the form of rotations of the state vector around the three axes of the Bloch sphere. The rotations are performed by the control current, as can be seen from the Hamiltonian (1.5) following [3]. Consider the current from the Hamiltonian:

$$I = I_{dc} + \Delta I \tag{1.7}$$

$$= I_{dc} + I_{lf}(t) + I_{\mu wc}(t)\cos(\omega_{10}t) + I_{\mu ws}(t)\sin(\omega_{10}t), \tag{1.8}$$

where $\hbar\omega_{10}$ is the energy difference between the 0 and 1 state, E_{10}. By inserting this into the Hamiltonian, treating ΔI as a perturbation, moving into a rotating frame, and rewriting in terms of Pauli matrices, the following expression is obtained for the Hamiltonian in the

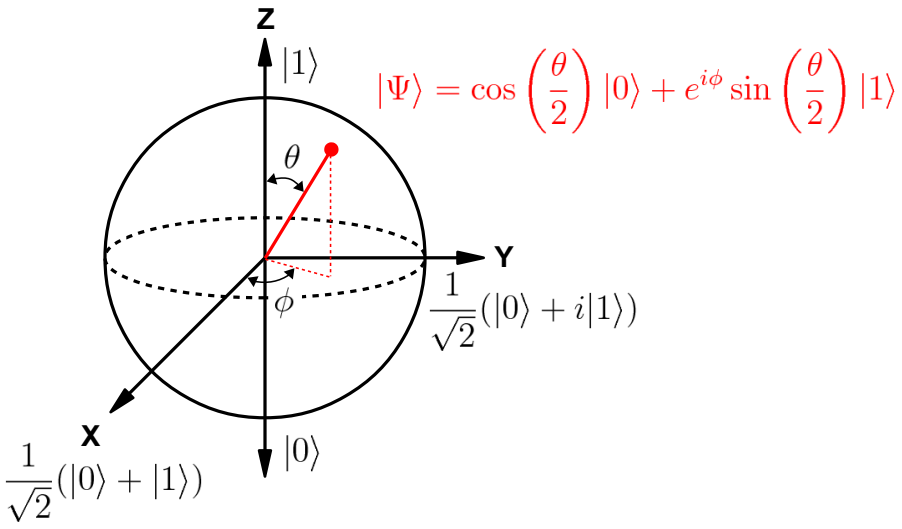

Figure 1.4: The Bloch sphere representation of a quantum two level system. Any pure single qubit state can be represented as a vector from the origin to a point on the surface of the sphere.

$|0\rangle, |1\rangle$ basis:

$$\begin{aligned} H &= \hat{\sigma_x} I_{\mu wc}(t) \sqrt{\hbar/2\omega_{10}C/2} \\ &+ \hat{\sigma_y} I_{\mu ws}(t) \sqrt{\hbar/2\omega_{10}C/2} \\ &+ \hat{\sigma_z} I_{lf}(t)(\partial E_{10}/\partial I_{dc})/2. \end{aligned} \tag{1.9}$$

A low frequency bias pulse changes the spacing between the levels, and therefore the precession rate, around the $\hat{z}$ axis. In the rotating frame, this appears as a $\hat{z}$ rotation. An excitation at the resonant frequency corresponds to a control vector in the equatorial plane of the Bloch sphere, and the phase of the excitation determines the direction of the control vector. Since cos and sin are 90 degrees out of phase, they define the $\hat{x}$ and $\hat{y}$ axis rotations. It is clear that, in this way, the state of the qubit can be completely controlled by the application of appropriate quasistatic and microwave control currents for appropriate lengths of time.

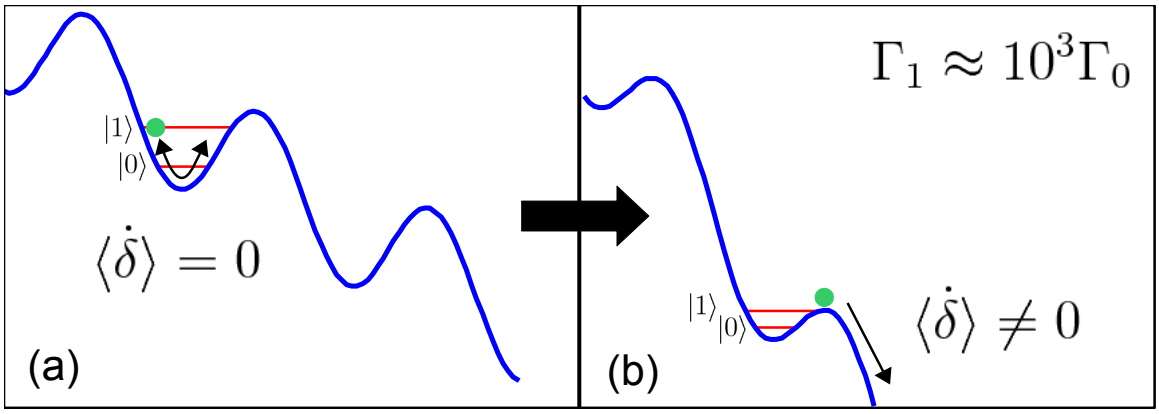

Figure 1.5: In panel (a), the tilt is shallow and the well is deep, leading to a very small tunneling rate from both the $|0\rangle$ state (Γ_0) and the $|1\rangle$ state (Γ_1). In panel (b), the potential has tipped so that Γ_1 is large but Γ_0 remains small. This allows the particle to fall down the potential only if in the $|1\rangle$ state causing a voltage to appear across the junction. (not drawn to scale)

1.1.2 Qubit readout

For the sake of completeness, we include a discussion of qubit readout, the final requirement for a practical qubit. Generally, we must generate a large classical signal, which depends on the quantum state of the qubit. For the phase qubit, this turns out to be relatively easy. The potential for the phase particle has the form of a tilted washboard with the tilt being controlled by the bias current (Equation 1.4). As the washboard tilts, the local minima become shallower. At some critical point, a particle in the higher energy $|1\rangle$ state will tunnel out of the well and fall down the potential, but the particle in the lower energy $|0\rangle$ state will still be trapped. (see Figure 1.5) Recalling the second Josephson relation (Equation 1.1), the running state with its time varying phase will generate a voltage that can be detected. This voltage, or absence thereof, is the measurement. In practice, this measurement scheme is not often employed because the voltage state generates large numbers of long-lived quasiparticles [7] which can lead to decoherence during the next cycle of the experiment. More information on other designs for readout that sidestep the quasiparticle generation issue can be found in [5, 8].

1.2 Qubit decoherence

In an ideal qubit, state information would only evolve according to the Hamiltonian (Equation 1.9) with perfectly experimentally controlled control currents. A real qubit, however, loses its state information over time; in other words, it experiences decoherence. Decoherence can be thought of as random rotations around the three axes of the Bloch sphere caused by noise in the parameters that control the qubit [3]. In the case of the current biased phase qubit, the control parameter is the bias current (see Equation 1.5). Decoherence is often characterized by two parameters called T_1 and T_2, which describe lengths of time over which information is preserved. T_1 describes the lifetime of a qubit state prepared at the north pole of the Bloch sphere (in the $|1\rangle$ state), and T_2 describes the lifetime of a qubit state prepared on the equator of the Bloch sphere. These two times are not completely independent. A qubit prepared at the pole of the Bloch sphere is sensitive to both $\hat{x}$ and $\hat{y}$ rotations, but not $\hat{z}$ rotations. Without loss of generality, we may assume that a qubit prepared on the equator of the Bloch sphere is prepared along the $\hat{x}$ axis. Such a state is sensitive to $\hat{z}$ and $\hat{y}$ rotations only. Both T_1 and T_2 are sensitive to $\hat{y}$ rotations, and that coupling leads to the following relation:

$$\frac{1}{T_2} = \frac{1}{2T_1} + \frac{1}{T_\phi}, \tag{1.10}$$

where T_ϕ is related to the transverse $\hat{z}$ rotation that affects the phase ϕ of the qubit state and is called the pure dephasing rate.

To measure T_1, the qubit is prepared in the $|1\rangle$ state by an $\hat{x}$ rotation pulse timed to cause the state vector to rotate from the initial $|0\rangle$ state to the $|1\rangle$, an angle of π on the Bloch sphere. Following a wait time, t_w, after the π pulse, the state of the qubit is measured. This sequence is repeated for different wait times t_w; for each value of t_w, the occupation

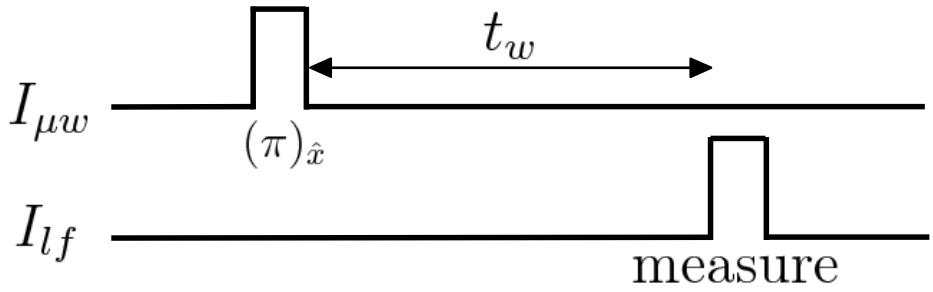

Figure 1.6: Pulse sequence for T_1 measurement. The qubit starts in the $|0\rangle$ state.

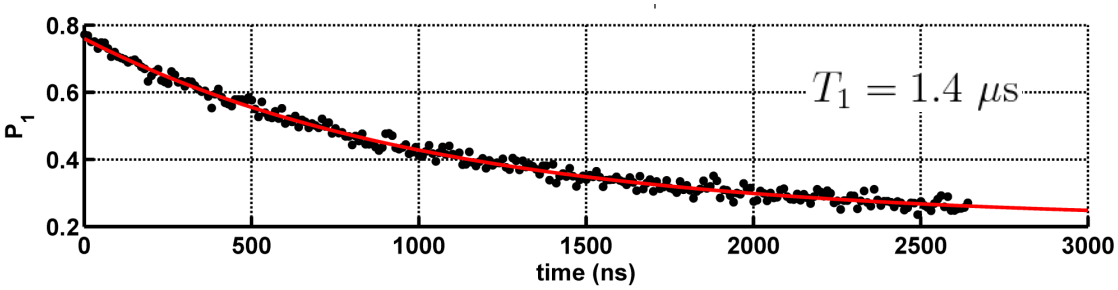

Figure 1.7: Qubit T_1 measurement. Occupation probability of the qubit $|1\rangle$ state decays exponentially with time constant equal to T_1. This data is from a long lifetime phase qubit with crystalline silicon capacitor dielectric courtesy of U. Patel.

probability of the $|1\rangle$ state is recorded. One finds that the probability of the qubit being in the $|1\rangle$ state decays exponentially with a time constant of T_1.

To characterize dephasing, one performs a Ramsey decay experiment. For a Ramsey decay experiment, the qubit is prepared on the equator of the Bloch sphere using a $\pi/2$ $\hat{y}$ pulse. Once there, a $\hat{z}$ pulse is applied to cause the Bloch vector to precess around the $\hat{z}$ axis for a time t_w, after which an $\hat{x}$ measurement is performed by first making a $\pi/2$ $\hat{y}$ rotation followed by a normal $\hat{z}$ measurement. The sequence is then repeated many times to determine the probability of ending in the $\hat{x}$ state as a function of t_w. The probability of the qubit being in the $\hat{x}$ state will oscillate with t_w from 1 when the state vector is pointing in the $\hat{x}$ direction to 0 when the state vector is pointing in the $-\hat{x}$ direction. The envelope of the oscillation will also decay with t_w and the characteristic time of that decay is called T_2^*. T_2^* is

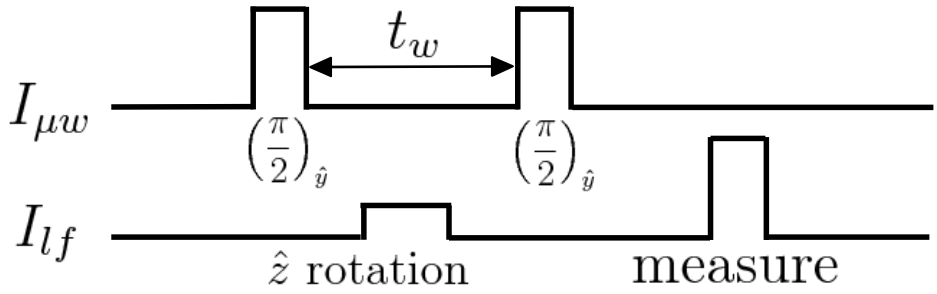

Figure 1.8: Pulse sequence for T_2^* measurement. The qubit starts in the $|0\rangle$ state. A $\pi/2$ pulse followed by a $\hat{z}$ measurement is equivalent to a measurement along the $\hat{x}$ axis

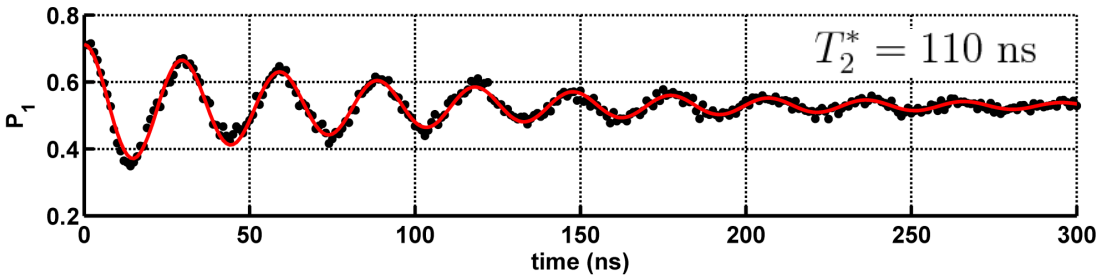

Figure 1.9: Qubit T_2^* measurement. Probability of the qubit being in the $|1\rangle$ state oscillates with a decay superimposed on top. This data is from the same crystalline silicon qubit, but shows a T_2^* time that is not improved by using the crystalline dielectric. This indicates T_2^* is still limiting performance. Figure courtesy of U. Patel.

closely related to T_2 and has contributions from two types of fluctuations: one from random phase kicks of the Bloch vector (T_2 proper) and the other is from random variations in the precession frequency between different realizations of the sequence. The former is present in every sequence in the same way and is therefore sometimes referred to as homogeneous broadening. The latter is due to very low frequency bias noise, which leads to offsets that are approximately constant over one repetition of the experiment but different for different repetitions. This source is referred to as inhomogeneous broadening.

In order to measure T_2, one can eliminate inhomogeneous effects by employing a spin echo sequence. In this sequence, a π pulse around the $\hat{x}$ axis is symmetrically placed between the preparation and measurement pulses in the Ramsey sequence. This π pulse reverses all

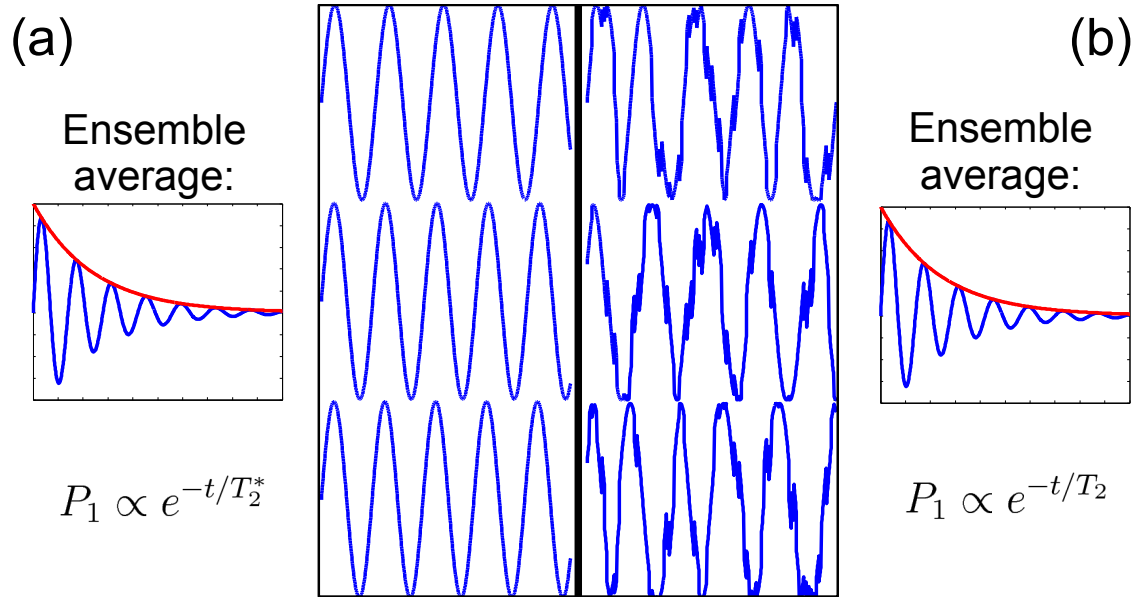

Figure 1.10: (a) shows ensemble members for a T_2^* measuremen. The decay is due to averaging members that differ in frequency, but the frequency is constant for each. (b) shows ensemble members where there are random phase kicks that result in decoherence; the resulting decay time is T_2.

evolution with respect to the $\hat{x}$ axis, and a constant rotation will cancel itself out, leaving only the homogeneous component, T_2.

T_1 involves a transition from a high energy state to a low energy state, and therefore, it involves an exchange of energy with the environment. The dissipation from the environment can be modeled as an effective admittance of a non-ideal current source, which provides the qubit bias. Specifically, it can be shown rigorously that T_1 is essentially the RC decay time of the qubit junction [3]:

$$\frac{1}{T_1} = \frac{\Re\{Y(\omega_{10})\}}{C}, \tag{1.11}$$

where $Y(\omega_{10})$ is the admittance of the bias circuitry at the qubit transition frequency and C is the junction capacitance. The dominant source of energy loss in current generation phase qubits is loss from two level system (TLS) defects in the capacitor dielectric [9]. These losses limit the T_1 times of the best specimens to $\sim$ 1.6 μs. More information on the material

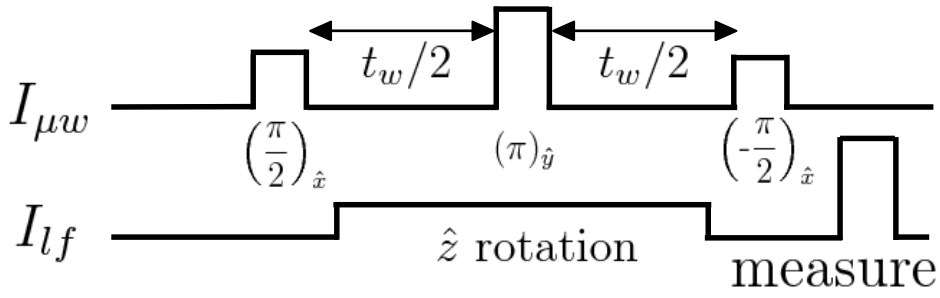

Figure 1.11: Pulse sequence for T_2 measurement. The qubit starts in the $|0\rangle$ state. This is the same as the Ramsey sequence but with a $\hat{y}$ π pulse symmetrically placed in the middle to refocus any inhomogeneous broadening.

origin of decoherence from TLS defects can be found in [10].

As restrictive as T_1 is T_2^* is always shorter: $\sim$ 120 ns for the longest-lived phase qubits. This indicates that the pure dephasing rate is the dominant source of overall decoherence. From the phase qubit Hamiltonian (Equation 1.9), a random $\hat{z}$ rotation (dephasing) is the result of a low frequency bias fluctuation.

Josephson junctions themselves exhibit a certain amount of critical current noise in the voltage state, as has been studied for many years in the context of developing low noise SQUIDs [11]. Subsequent results show that there is also noise of the same magnitude through a junction in the zero voltage state, such as is the case with a qubit [12]. This noise will give rise to dephasing; however, experiments have determined the typical magnitude of the noise [11]:

$$S_{I_0}(1\text{Hz}) = (10^{-6} I_0)^2/\text{Hz}, \tag{1.12}$$

for a 100 μm^2 junction at 4 K. It has been found that the noise scales with temperature as T^2 and inversely with area [13, 14]. Calculations show that critical current noise is too small to limit qubits [3, 10]

There is another possible source of bias noise, flux noise inductively coupled to a loop containing the junction. In this case $S_I = S_\Phi/L$, where L is the inductance of the loop.

1.3 $1/f$ flux noise in qubits

It is possible to directly measure bias noise with qubits using various techniques. Bialczak *et al.* used the resonant response of the qubit to directly measure the flux noise spectral density [15]. The experiment involves driving the qubit slightly off of ω_{10} and measuring the occupation probability of the $|1\rangle$ state as a function of time. Any low frequency current shifts the resonance, causing the $|1\rangle$ state occupation probability to rise or fall depending on the direction of the shift. The Fourier transform of the P_1 time series corresponds to the flux noise. Furthermore, by correlating the noise at a positive bias current with noise at a negative bias current, it is possible to distinguish flux noise from critical current noise. The results show that the noise is flux like.

It is also possible to estimate the noise magnitude by carefully measuring the envelope of the Ramsey fringes and assuming something about the spectral shape [16, 17, 18]. The Ramsey decay envelope $f_R(t)$ can be calculated as:

$$f_R(t) = \exp\left(-\frac{t^2}{2}\left(\frac{\partial\omega_{10}}{\partial\Phi}\right)^2 \int_{-\infty}^{\infty} d\omega S_\Phi(\omega)\ \mathrm{sinc}^2\left(\frac{\omega t}{2}\right)\right). \tag{1.13}$$

For a white spectrum of noise, $S_\Phi(\omega) = const$, the decay is an exponential function. However, for a $1/f$ decay function

$$S_\Phi(\omega) = \frac{A}{\omega}, \quad \omega_l < |\omega| < \omega_h \tag{1.14}$$

where ω_l is a low frequency cutoff, and ω_h is a high frequency cutoff, the Ramsey decay envelope takes on a Gaussian form

$$f_R(t) = \exp\left(-\frac{t^2}{2}\left(\frac{\partial\omega_{10}}{\partial\Phi}\right)^2 \times 2A\ln(\frac{\omega_h}{\omega_l})\right). \tag{1.15}$$

Therefore, by measuring a Gaussian decay envelope and assuming the noise has a $1/f$ spectral

shape, it is possible to estimate the magnitude of the noise.

The magnitude of the noise inferred from both of these experiments ($\sim 5-10\ \mu\Phi_0/\sqrt{\mathrm{Hz}}$) is compatible with the flux noise previously measured in SQUIDs at milikelvin temperatures [19]. Because the qubits so closely relate to SQUIDs, and the flux noise from each has very similar properties, it is reasonable to assume that the noise is from the same source. The results from this thesis on SQUIDs should also apply immediately to qubits.

Bibliography

[1] M. Tinkham, *Introduction to superconductivity* (Dover Publications, 31 East 2nd Street, Mineola, NY 11501-3852, 2004).

[2] J. Clarke, A. Cleland, M. Devoret, D. Esteve, and J. Martinis, Science **239**, 992 (1988).

[3] J. Martinis, S. Nam, J. Aumentado, K. M. Lang, and C. Urbina, Phys. Rev. B **67**, 094510 (2003).

[4] J. Martinis, S. Nam, J. Aumentado, and C. Urbina, Phys. Rev. Lett. **89**, 117901 (2002).

[5] R. W. Simmonds, K. M. Lang, D. A. Hite, S. Nam, D. P. Pappas, and J. Martinis, Phys. Rev. Lett. **93**, 077003 (2004).

[6] J. Martinis, Quantum information processing **8**, 81 (2009).

[7] K. Lang, S. Nam, J. Aumentado, C. Urbina, and J. Martinis, Applied Superconductivity, IEEE Transactions on **13**, 989 (2003).

[8] M. Steffen, S. Kumar, D. DiVincenzo, G. Keefe, M. Ketchen, M. B. Rothwell, and J. Rozen, Appl. Phys. Lett. **96**, 102506 (2010).

[9] J. Martinis, K. Cooper, R. McDermott, M. Steffen, M. Ansmann, K. Osborn, K. Cicak, S. Oh, D. Pappas, R. Simmonds, and C. C. Yu, Phys. Rev. Lett. **95**, 210503 (2005).

[10] R. McDermott, Applied Superconductivity, IEEE Transactions on **19**, 2 (2009).

[11] B. Savo, F. C. Wellstood, and J. Clarke, Appl. Phys. Lett. **50**, 1757 (1987).

[12] M. Mück, M. Korn, C. Mugford, J. Kycia, and J. Clarke, Appl. Phys. Lett. **86**, 012510 (2005).

[13] F. Wellstood, C. Urbina, and J. Clarke, Appl. Phys. Lett. **85**, 5296 (2004).

[14] L. Faoro and L. B. Ioffe, Phys. Rev. B **75**, 132505 (2007).

[15] R. Bialczak, R. McDermott, M. Ansmann, M. Hofheinz, N. Katz, E. Lucero, M. Neeley, A. O'Connell, H. Wang, A. Cleland, and J. Martinis, Phys. Rev. Lett. **99**, 187006 (2007).

[16] F. Yoshihara, K. Harrabi, A. Niskanen, Y. Nakamura, and J. S. Tsai, Phys. Rev. Lett. **97**, 167001 (2006).

[17] K. Kakuyanagi, T. Meno, S. Saito, H. Nakano, K. Semba, H. Takayanagi, F. Deppe, and A. Shnirman, Phys. Rev. Lett. **98**, 047004 (2007).

[18] G. Ithier, E. Collin, P. Joyez, P. Meeson, D. Vion, D. Esteve, F. Chiarello, A. Shnirman, Y. Makhlin, J. Schriefl, and G. Schön, Phys. Rev. B **72**, 134519 (2005).

[19] F. Wellstood, C. Urbina, and J. Clarke, Appl. Phys. Lett. **50**, 772 (1987).

Chapter 2

$1/f$ flux noise

The first challenge in understanding flux noise is understanding the origin of the $1/f^{\alpha}$ spectral shape. One possible explanation comes from postulating the existence of a collection of two level systems (TLS), and allowing those TLS to fluctuate randomly between two states. The appearance of the $1/f$ spectrum follows naturally from a few more plausible assumptions. This development follows the review from Dutta and Horn [1] and Weissman [2].

A single TLS fluctuates randomly between its two states, generating a so-called random telegraph signal. If the TLS changes back and forth with some characteristic time τ, the spectrum for the random telegraph signal [3] will take on a Lorentzian form

$$S(\omega)_{TLS} \propto \frac{\tau}{1+\omega^2\tau^2}. \tag{2.1}$$

If a large number of such Lorentzian *independent* TLS with some distribution of characteristic times $D(\tau)$ are superimposed, then the spectrum has the general form

$$S(\omega)_{TLS} \propto \int \frac{\tau}{1+\omega^2\tau^2} D(\tau)\mathrm{d}\tau. \tag{2.2}$$

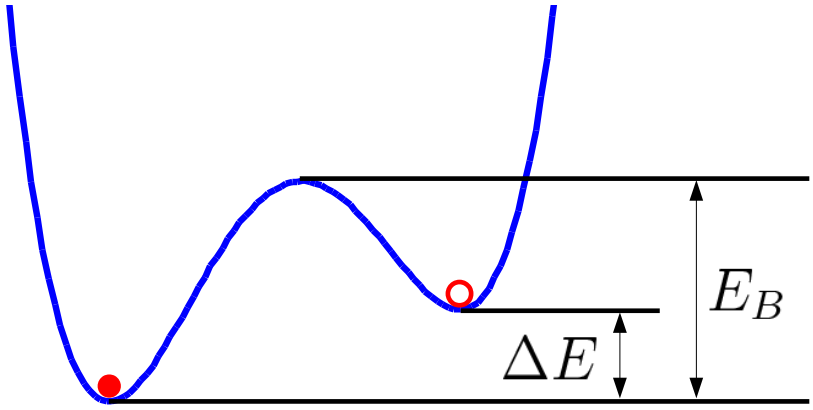

Figure 2.1: TLS potential. There are two states separated by an energy barrier of height E_B. In general there is also some energy difference ΔE between the states. The TLS can either be excited over the barrier by thermal fluctuations or it can tunnel through the barrier to change states.

It is possible now to create *any* spectrum desired by the proper choice of the characteristic time distribution $D(\tau)$. The problem is then to physically motivate a distribution that will give rise to noise with a $1/f$ spectrum.

It is reasonable to assume that the distribution of barrier heights is uniform: $D(E) = const$. This can be expected, generally, because there is no obvious reason to prefer any particular barrier height over another. Just by this symmetry, the distribution should tend to be uniform.

It is also reasonable to assume that the characteristic time for a given TLS is exponentially dependent on an energy barrier height separating the two states. This can occur for thermal activation where:

$$\tau = \tau_0 \exp\left(E/k_B T\right), \tag{2.3}$$

or for quantum tunneling, where the tunneling probability also depends exponentially on the barrier height. The distribution of barrier heights is assumed above to be uniform; thus, the distribution of relaxation times is log-uniform.

By inserting the assumption of a log-uniform distribution of relaxation times into 2.2, taking the case of thermal activation, and changing variables to energy, the following expression is obtained:

$$S(\omega) \propto \int \frac{\tau_0 \exp\left(E/k_B T\right)}{1+\omega^2\tau_0^2 \exp\left(2E/k_B T\right)} D(E)\mathrm{d}E. \tag{2.4}$$

Performing the integration yields

$$S(\omega) \propto \frac{k_B T}{\omega} D(E) \quad \text{for } \tau_2^{-1} \ll \omega \ll \tau_1^{-1}. \tag{2.5}$$

Thus, the spectrum will have a $1/f$ form within the range of frequencies encompassed by the TLS characteristic times. Because this model is based on thermal activation, and assuming the energy barriers are not temperature-dependent, the noise magnitude is temperature-dependent.

2.1 $1/f$ flux noise in SQUIDs

One important example of a system that exhibits $1/f$ noise is the flux threading a dc SQUID. The earliest characterization of low frequency flux noise in SQUIDs at millikelvin temperatures was done by Wellstood *et al.* in the late 1980s [4]. SQUID noise was measured using a second SQUID in a flux locked loop as a sensitive current amplifier (see 3.6). As the devices were cooled, the white noise went down, but the excess low frequency noise did not. They measured a series of SQUIDs made with different materials and geometries in an attempt to locate the source of the noise. Although they were unable to positively identify the source, they were able to rule out many possibilities and make several important observations that guided theoretical and experimental development.

2.1.1 Observations about $1/f$ flux noise

The results of those experiments can be summarized as follows:

1. The noise was flux like, as demonstrated by observing noise power which is proportional to SQUID flux sensitivity.

2. There was no systematic dependence of the noise on the materials considered including Pb, PbIn, and Nb superconductors.

3. There was no systematic dependence of the noise on SQUID geometry considering very large differences in area, linewidth, and inductance.

4. The noise was very weakly dependent on temperature below $\sim$ 1K.

5. $1/f$ noise power had a nearly universal magnitude and spectral shape

$$S_\Phi = \frac{A}{f^\alpha} \tag{2.6}$$

with the magnitude of A $\sim 5 - 10\ \mu\Phi_0/\sqrt{\text{Hz}}$ at 1 Hz, and $0.58 < \alpha < 0.80$.

Some of these results, at first glance, seem to be contradictory. If the noise originates from far from the SQUID, one would expect the magnitude to strongly depend on the sensing area of the device. If, however, the noise originates from the SQUID materials themselves, one would expect to see some difference from the materials used in fabrication. Thus, the problem has lain dormant until the recent demand for long decoherence times in qubits has revived the subject.

Bibliography

[1] P. Dutta and P. Horn, Reviews of Modern Physics **53**, (1981).

[2] M. Weissman, Reviews of modern physics **60**, 537 (1988).

[3] S. Machlup, Journal of Applied Physics **25**, 341 (1954).

[4] F. Wellstood, C. Urbina, and J. Clarke, Appl. Phys. Lett. **50**, 772 (1987).

Chapter 3

SQUID theory and operation

The overwhelming majority of work in this thesis is performed with the Superconducting QUantum Interference Device (SQUID) as its primary component. SQUIDs act like a flux-to-voltage transducer and form the basis of the most sensitive amplifiers. The SQUID is also very flexible, which allows one to easily vary materials and temperatures of operation. As such, it is useful to take some time to describe the basic functioning of the SQUID and to elaborate on a few of the circuits used for the readout and data processing from these devices.

This description focuses on the dc SQUID, so called because it is biased with a dc current. This is the design that appears exclusively in this work. These experiments rely only on the flux-to-voltage transducer property of the SQUID, and that property is already present in the simplest models.

A SQUID is a loop of superconducting material interrupted by two Josephson junctions. We will see that the Josephson relations coupled with the concept of flux quantization gives rise to the SQUID flux-to-voltage transfer function.

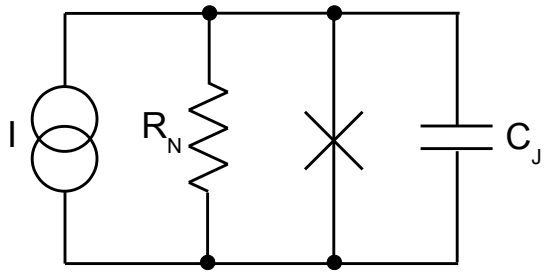

Figure 3.1: RCSJ model circuit diagram

3.1 dc SQUID theory

To describe the SQUID, we must first introduce the Josephson junction, a project that has been started in section 1.4. There, the junction was modeled as a capacitor and an ideal Josephson element in parallel. For the SQUID, we must also add a finite shunt resistance, thereby forming the so-called RCSJ (resistively and capacitively shunted junction) model. Resistance gives rise to damping of the phase particle proportional to $1/R_N$. To see this, we proceed as before by writing the current through the parallel combination:

$$I = I_c \sin\delta + V/R + CdV/dt. \tag{3.1}$$

Eliminating V in favor of δ gives a differential equation on δ:

$$(1/\omega_p)^2 d^2\delta/dt^2 + Q^{-1}(1/\omega_p)d\delta/dt + \sin\delta = I/I_c, \tag{3.2}$$

where $\omega_p^2 = \frac{2\pi I_c}{C\Phi_0}$ and $Q = \omega_p RC$. The term proportional to $d\delta/dt$ is recognized as a drag force on the phase particle.

The tilt of the potential is controlled by the bias current I. As the current is increased from 0, eventually a point will be reached, $I = I_0$, where the phase particle will transition out of the local minimum and roll continuously down the potential. This will result in a voltage

developing across the junction, according to the second Josephson equation. If the current is reduced, eventually the particle will retrap back in a minimum and return to the zero voltage state. That current is called the retrapping current, I_r. In general, $I_0 \neq I_r$ because the phase particle has inertia. This gives rise to hysteresis in the junction IV curve. Even after the bias current has been reduced to the point where local minima are again present, the particle will have enough inertia to avoid retrapping. This means that in the absence of damping, the phase particle will not retrap until the current is reduced completely to zero. Of course, if the damping is very strong, then the particle will retrap as soon as a minimum is re-formed and $I_r = I_0$. Hysteresis needs to be avoided for a SQUID intended to measure flux because generally there will be two stable voltages for a given flux level, but also because traversing the multiple branches in the IV curve requires a complicated bias sequence. These complications are avoided by ensuring that the devices are always overdamped and therefore non-hysteretic. To ensure this, the damping must remove as much energy from the phase particle every cycle as it gains by falling another cycle down the potential. This can be thought of as a competition between two times: an L/R time adding energy and an RC time removing it. When the times are equal, this is the boundary between hysteretic and a single valued IV curve. The relevant inductance scale comes from the Jospehson inductance (see 1.2). We introduce the damping parameter β_C

$$1 = R^2C/L = 2\pi I_c R^2 C/\Phi_0 = \beta_C. \tag{3.3}$$

When $\beta_C < 1$, the junction is non-hysteretic. β_C is the McCumber-Stewart damping parameter, which is a well known result for Josephson junctions [1, 2].

In the strongly overdamped regime, the differential equation for the phase simplifies. Typically, the critical current and capacitance are fixed by the junction fabrication technology, and therefore, to ensure the $I - V$ characteristics are non-hysteretic, a resistance small

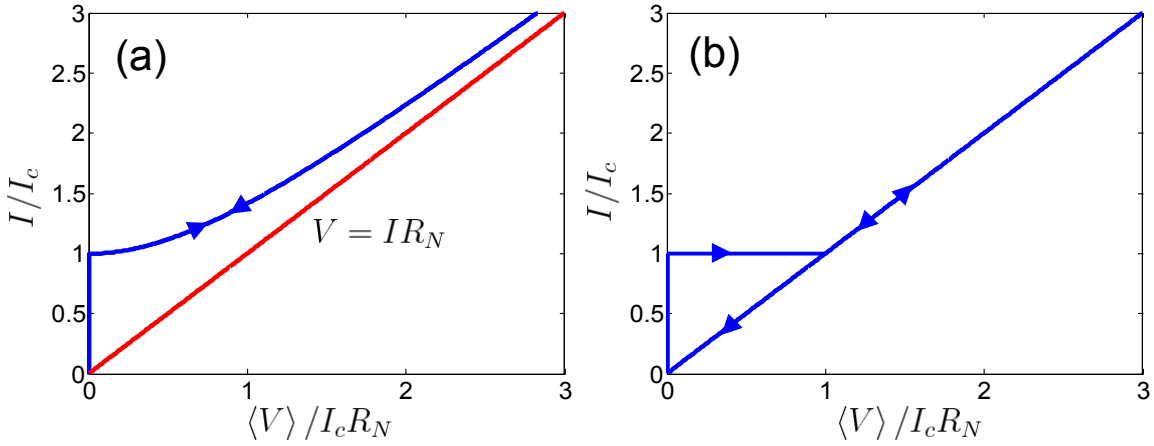

Figure 3.2: Junction IV characteristic in the RCSJ model. In the overdamped case (a), $Q \ll 1$, where the IV curve is not hysteretic and converges to the normal shunt resistance at large voltages. In the underdamped case (b), $Q \gg 1$, the IV curve is hysteretic with the junction following the normal resistance line until it finally retraps into the zero voltage state at $I = 0$.

enough to ensure $\beta_c < 1$ is chosen. If R is small, so that $Q \ll 1$, the differential equation for the phase (eq. 3.2) can be written

$$\frac{d\delta}{dt} = \frac{2\pi I_c R}{\Phi_0}\left(\frac{I}{I_c} - \sin\delta\right). \tag{3.4}$$

The second Josephson relation can be used to solve for the average voltage as a function of current yielding: [3]

$$V = \Re\{R(I^2 - I_c^2)^{1/2}\}. \tag{3.5}$$

3.1.1 Flux quantization

Flux quantization results from the requirement of a single-valued superconducting order parameter Ψ. This means that around any closed path through a superconductor the

superconducting phase ϕ must advance by an integer multiple of 2π [3]:

$$\oint \nabla\phi \cdot ds = 2\pi n, \tag{3.6}$$

for some integer n. According to the BCS theory of superconductivity, a magnetic field results in a phase gradient

$$\nabla\phi = \frac{2eA}{\hbar}. \tag{3.7}$$

Substituting equation 3.7 into 3.6 gives:

$$\oint \frac{2e}{\hbar} A \cdot ds = 2\pi n. \tag{3.8}$$

Note that

$$\oint A \cdot ds = \Phi, \tag{3.9}$$

where Φ is the enclosed flux, implies that the flux is quantized

$$\Phi = \frac{h}{2e} n = n\Phi_0, \tag{3.10}$$

where Φ_0 is the magnetic flux quantum.

In the case of a ring of superconducting material, this means that if an external flux is applied, a current will begin to flow, creating an equal and opposite flux in order to maintain the quantization condition on the total flux.

In the context of a SQUID, the loop is interrupted by Josephson junctions, each supporting a phase difference across them, which gives the SQUID extra degrees of freedom to fulfill the quantization condition (3.6).

3.1.2 dc SQUID characteristics

The total current through the SQUID is the sum of the current through the branches. Therefore, the maximum zero voltage current for identical junctions is $2I_c$, where I_c is the critical current of a single junction. Because the junctions are embedded in a loop, an external applied flux gives rise to a phase advancement around the loop. The additional free parameters of the phase across the junctions imply that the flux need not be completely screened by a circulating current in order to keep the superconducting condensate single valued. For simplicity, we begin by neglecting the contribution of the screening current and calculating the transport current through the SQUID. The condition of a single valued phase still applies, thus:

$$\delta_1 + \delta_\Phi/2 = \delta_2 - \delta_\Phi/2 \tag{3.11}$$

$$\delta_2 = \delta_1 + \delta_\Phi = \delta_1 + 2\pi\frac{\Phi}{\Phi_0}, \tag{3.12}$$

where δ_Φ is the phase advancement due to the external flux. Therefore, the transport supercurrent across the device can be written in terms of the flux and the phase across one junction, as follows:

$$I = I_c \sin\delta_1 + I_c \sin\delta_2 \tag{3.13}$$

$$= I_c[\sin\delta_1 + \sin(\delta_1 + 2\pi\Phi/\Phi_0)]. \tag{3.14}$$

The critical current of the SQUID (I_0) is defined as the maximum supercurrent the device can support. Equation 3.14 should be maximized with respect to δ_1 to calculate the critical current of the SQUID. This can be achieved with a trigonometric identity yielding:

$$I_0 = 2I_c|\cos(\pi\Phi/\Phi_0)|. \tag{3.15}$$

Thus the SQUID has a critical current that is dependent on the flux threading the loop, and if it is current biased slightly above the critical current, then the voltage across the SQUID will depend on the flux, implementing a flux-to-voltage transducer. This is the basis of using a SQUID to detect flux.

Taking into account the effect of the circulating screening current changes the details of the flux to voltage transfer function, but it does not change the fundamental periodicity in Φ_0, and therefore it does not change the fundamental operating principle of the device. Thus, for the remainder of the discussion, screening will continue to be ignored; this is equivalent to considering a very small inductance SQUID.

Since the SQUID in the limit $L \to 0$ behaves like a compound Josephson junction with a flux dependent critical current, it is possible to write an explicit form for the IV curve by substituting equation 3.15 into 3.5, giving:

$$V = \Re\{R[I^2 - (I_c \cos(\pi\Phi/\Phi_0))^2]^{1/2}\}, \tag{3.16}$$

where R is the resistance shunting the SQUID, and I_c is the critical current for the SQUID.

3.1.3 dc SQUID noise

The sensitivity of the SQUID to flux is limited by white noise. The main source of white noise is Johnson noise in the shunt resistors.

Johnson noise appears as a fluctuating voltage across any resistor as a consequence of the fluctuation-dissipation theorem. The spectral voltage noise spectral density of a resistor with resistance R at temperature T is

$$S_V = 4k_B T R. \tag{3.17}$$

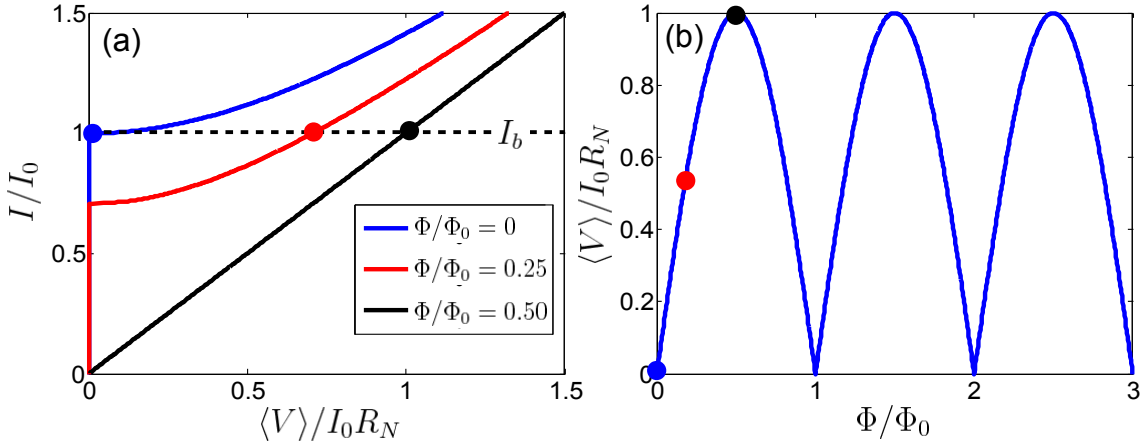

Figure 3.3: SQUID IV curve for three flux biases. The critical current modulates with the applied flux and has a minimum at $\Phi = \Phi_0/2$. The device is often operated by biasing at a constant current and observing the voltage. The right panel shows the $V - \Phi$ curve, which results from biasing at $I_b = I_0$. The colored circles correspond to the the flux states in (a).

The Johnson noise from the shunt resistors gives rise to a voltage noise across the SQUID. This voltage noise will appear as a flux noise depending on the flux-to-voltage transfer coefficient $V_\Phi = dV/d\Phi$, which is the slope of the $V - \Phi$ curve where the SQUID is biased and depends on all of the details of the SQUID. The largest V_Φ coefficient will give the highest sensitivity. In general, there is no analytic expression for V_Φ or the SQUID voltage noise; however, detailed numerical simulations have been done to estimate these parameters and give an idea of where they are optimized, and therefore, of the theoretical limit to SQUID sensitivity [4, 5]. These simulations find that the energy sensitivity of the SQUID is greatest for $\beta_L = 2LI_0/\Phi_0 \approx 1$ and $\beta_C \approx 1$. For these parameters, the maximum of V_Φ has the simple form

$$V_\Phi \approx \frac{R}{L}. \tag{3.18}$$

The SQUID voltage noise is approximately four times the Johnson noise of an equivalent resistor

$$S_v(f) \approx 16 k_B T R; \tag{3.19}$$

therefore, the flux white noise level is

$$S_\Phi = \frac{S_V}{V_\Phi^2} \approx \frac{16 k_B T L^2}{R}. \tag{3.20}$$

For a 100 pH SQUID at 200 mK with 10 Ω shunt resistors, this result is $\approx 0.1\ \mu\Phi_0/\sqrt{\text{Hz}}$.

3.2 dc SQUID readout operation

A SQUID can be read out several ways. The most straight forward is to simply current bias above the critical current, and flux bias with an external applied flux at the steepest point on the SQUID V-Φ curve. Here the output voltage change, ΔV, for a small flux change, $\Delta\Phi$, will be

$$\Delta V = \left(\frac{dV}{d\Phi}\right)\Delta\Phi. \tag{3.21}$$

The downside to this arrangement is the severely limited linear dynamic range. In order to linearize the response of the SQUID over a very wide flux range and make operation convenient, the SQUID is typically operated in a flux locked loop.

3.2.1 Flux locked loop

In a flux locked loop arrangement, the SQUID is used as a null detector for magnetic flux. Whenever the applied flux drifts away from the locked value, the flux locked loop applies a counterbalancing flux through a feedback coil with mutual inductance M_f to the SQUID, to return the total external flux to the locked value. The current through the feedback coil, therefore, is proportional to the external flux applied to the device. That current passes through a feedback resistor, R_f, and the voltage across that resistor is the output of the flux

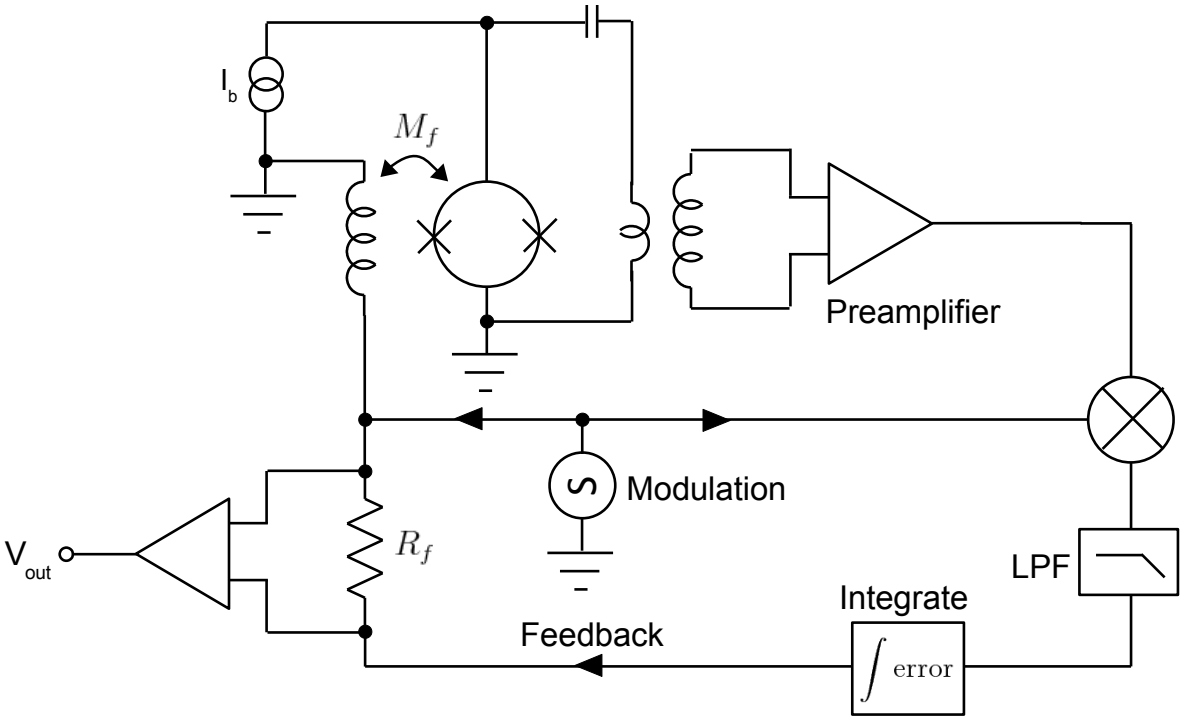

Figure 3.4: Flux locked loop block diagram

locked loop. The output voltage is related to the external flux by:

$$\Delta V = \frac{R_f}{M_f}\Delta\Phi. \tag{3.22}$$

Typically, the null detection is done by means of a lock-in measurement of a small amplitude modulation flux. The main advantage of the lock-in detection is avoiding the $1/f$ noise of the readout preamplifier by pushing the signal to a higher frequency. If the modulation signal at frequency f_0 (typically of order 100 kHz) is centered on a minimum of the $V-\Phi$ curve, then the voltage signal contains only components at $2f_0$ and higher. This $2f_0$ signal is mixed down and filtered and produces no output after the demodulation. This is the null signal. If flux enters the loop, then the modulation signal moves off of the minimum of the $V-\Phi$ curve and the demodulated signal contains a DC component proportional to the error.

This error signal is integrated and fed back to push the SQUID back to the null point.

In general, it is not easy to engineer the value of M_f with very much precision, but there is a relatively simple technique to calibrate this number for quantitative measurement. This procedure relies on the null detection mechanism and the periodicity of the SQUID $V - \Phi$ curve. When the SQUID is locked, the feedback mechanism will seek a null point; however, there are many identical points due to the fact that the $V - \Phi$ curve is periodic in Φ_0. Exactly which point is chosen is somewhat a matter of chance, but it can also be influenced by applying a flux before trying to lock. By locking, unlocking, and relocking several times, the flux locked loop will likely lock at several different null points and the output voltage will take on several different DC offsets. The difference in voltage between two adjacent locking points corresponds to exactly one flux quantum more being applied by the mutual inductance. This voltage is also the conversion factor R_f/M_f that is sought.

As a practical matter, there is also always a contribution to the noise from the preamplifier. The preamplifier for our experiments is a room temperature JFET, which is optimally noise matched with a transformer to the output impedance of the SQUID. Noise measurements indicate that the input voltage noise is ~ 0.1 nV/$\sqrt{\text{Hz}}$ at the ~ 100 kHz modulation frequency. This corresponds to a flux noise level of ~ 0.5 μV/$\sqrt{\text{Hz}}$. This is also well below the $1/f$ levels at 1 Hz. For more sensitivity, we often employ a second SQUID as a current preamplifier. For a typical flux gain of ~ 20, the room temperature noise is completely negligible. Additionally, the correlation amplifier setup described below is theoretically capable of completely eliminating all noise contribution from twin uncorrelated preamplifiers. Put together, preamplifier noise is not expected to contribute significantly to measurements of $1/f$ noise.

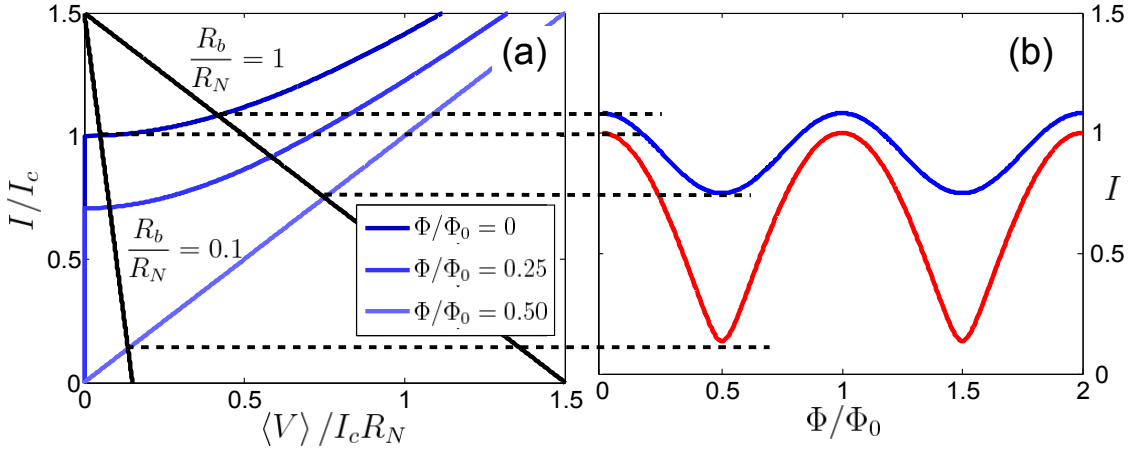

Figure 3.5: The operating point can be visualized as a load line from the bias resistor intersecting the SQUID IV as in panel (a). Generally, smaller bias resistors give larger signal for the same bias current. Note that the $I - \Phi$ curve is periodic in flux with a period of $1\Phi_0$. The right panel (b) is showing the $I - \Phi$ curves for a SQUID with two different sized bias resistors.

3.2.2 Two stage SQUID amplifier

In the flux locked loop, the SQUID voltage is read out most conveniently by a room temperature amplifier. The input noise of that amplifier fundamentally limits the sensitivity of the system. In order to provide higher signal to noise levels for very small flux noise signals, a second SQUID can be employed as a preamplifier.

In this arrangement, the first stage SQUID (the device under test) is voltage biased by a small (fraction of an ohm) bias resistor. In the IV plane, the bias resistor appears as a nearly vertical load line. The intersection of that load line with the SQUID IV curve establishes the operating point. Completely analogous to the current bias case, the device has an $I - \Phi$ curve which is periodic in flux with a period of $1\Phi_0$. In normal operation, a flux bias will be applied to the first stage to operate at the steepest part of the I-Φ curve to maximize the gain. In this way, the voltage bias converts a fluctuating flux into a fluctuating current. This current is then coupled to a second SQUID via an integrated on-chip input coil which

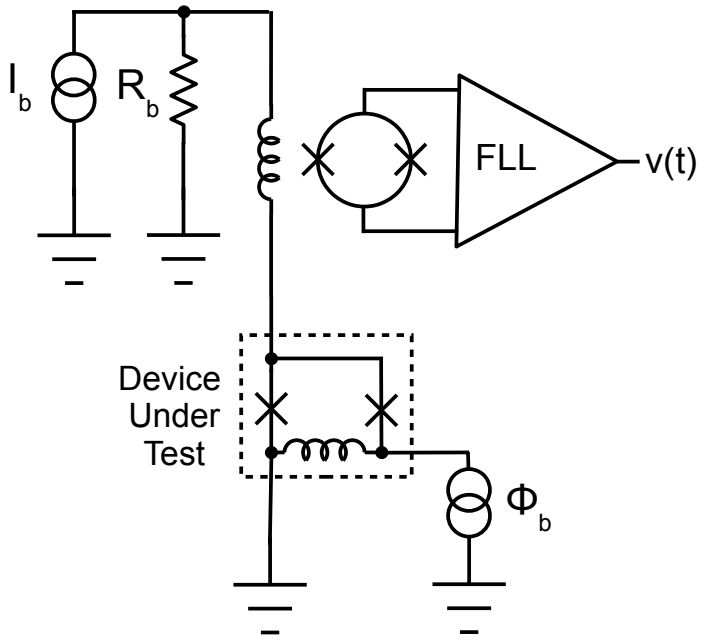

Figure 3.6: Two SQUID amplifier circuit diagram. The device under test is voltage biased and flux biased to the point of maximum $dI/d\Phi$ and the current is read out by a second SQUID in a flux locked loop. The flux bias can also be supplied by an external coil for devices where direct injection is impossible.

is in turn read out by a standard flux locked loop.

The gain from the first stage depends on $dI/d\Phi$ of the first stage SQUID and the mutual inductance M of the second stage input coil:

$$G_\Phi = \frac{dI}{d\Phi_1} M = \frac{d\Phi_2}{d\Phi_1}. \tag{3.23}$$

This number is calibrated by sweeping out the $I - \Phi$ curve and measuring its slope. The current axis represents a flux in the second stage (thanks to the mutual inductance M), and the Φ axis represents a flux in the first stage; thus, the slope of the $I - \Phi$ curve gives the flux gain at each flux bias point. One need not know the mutual inductance between the first

stage flux bias line and the first stage SQUID if the amplitude of the flux sweep is larger than 1 Φ_0 because the $I - \Phi$ will repeat; the period of the $I - \Phi$ is a calibration for the first stage flux. Typical flux gains are in the range of 10-100 and provide a noise floor of $< 1\ \mu\Phi_0/\sqrt{\text{Hz}}$ referred to the input of the first stage SQUID.

A final interesting feature of this experiment is that the first stage SQUID need not be biased at the steepest point on its $I - \Phi$ curve where the flux gain is the largest. If the first stage is biased at a minimum of its $I - \Phi$ curve then a small change in flux will not cause a change in current. This is useful for distinguishing flux-like noise from critical current-like noise because the amplitude of the latter will not be affected by the flux bias point.

3.2.3 SQUID correlation amplifier

Even the two stage SQUID amplifier is ultimately limited by the noise of the second stage SQUID. In order to accurately and efficiently measure even lower noise levels, we have implemented a SQUID correlation amplifier. This is similar to the two-stage SQUID amplifier setup except there are twin second stage SQUIDs, each receiving a copy of the current from the first stage by being installed in series with that device.

The advantage of this arrangement is that the noise from the first stage SQUID is correlated in the two second stage SQUIDs, whereas the noise from the second stage SQUIDs themselves will, in general, not be correlated. This means that, in principle, the noise from the amplifier chain can be completely eliminated and the noise level that can be measured is limited only by the patience of the investigator. In practice, the measurement will be limited by some spurious correlation caused by cross talk between the second stage SQUIDs.

The calibration of the measurement is identical to the procedure for the two-stage SQUID amplifier except that it must be done twice, once for each second stage. There is also some additional post processing in order to extract the correlated signal from the two outputs.

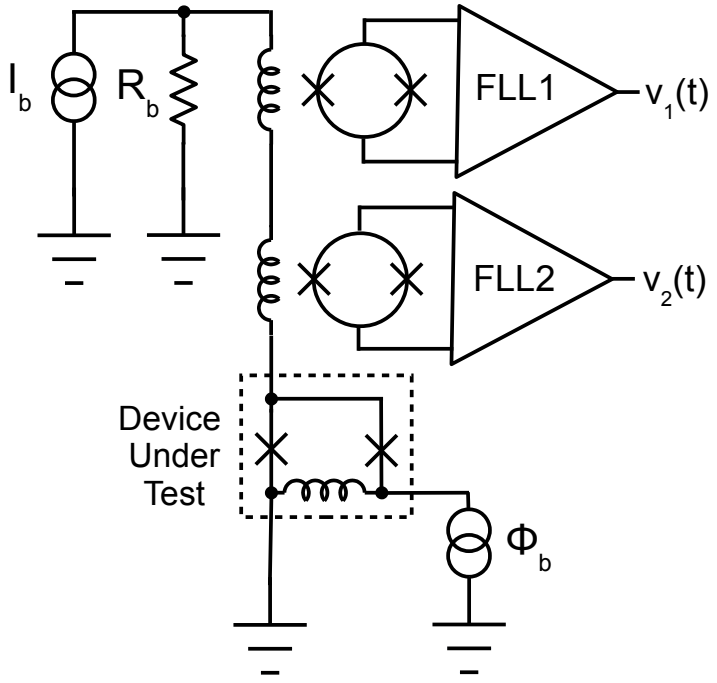

Figure 3.7: Correlation amplifier circuit diagram. This works just like the two-SQUID amplifier (Fig. 3.6) except two SQUIDs are reading out the current simultaneously.

Take v_1 and v_2 as the outputs from the twin second stage flux locked loops. First, each voltage signal is Fourier transformed:

$$\mathcal{F}_{1,2} = \int_{-\infty}^{\infty} v_{1,2}(t) e^{-2\pi i f t}. \tag{3.24}$$

Next, the correlation function is computed.

$$S_{12} = \langle \mathcal{F}_1^* \mathcal{F}_2 \rangle \,, \tag{3.25}$$

where the averaging is over the ensemble of time series. Finally, S_{12} is referenced to the input of the device under test as a flux by dividing by the appropriate factors G_1 and G_2

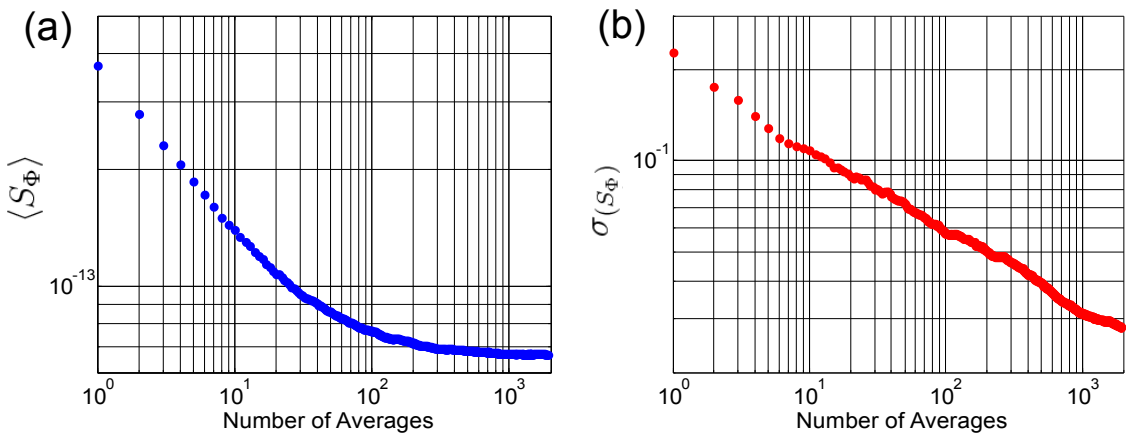

Figure 3.8: Measured correlation amplifier progression. The left panel shows that the average value of the cross spectrum drops and then saturates as the noise contribution from the readout stage is averaged away. The right panel shows that the accuracy of the estimate gets better as averages are taken, even past the point that the readout noise is removed.

for the two readout SQUIDs, as determined by the individual $I - \Phi$ gain calibrations and R_f/M_f:

$$S_\Phi = \frac{S_{12}}{G_1 G_2}. \tag{3.26}$$

As more and more traces are included in the average, the average value of the correlation spectrum falls until it ultimately saturates. The saturation is an indication that the noise contribution of the second stage has been suppressed to the full extent possible. The variance in the spectrum will continue to decrease with averages in the usual way. With this setup, it has been possible to measure very accurate $1/f$ noise spectra to noise levels $< 0.1\ \mu\Phi_0/\sqrt{\text{Hz}}$ over several decades of frequency.

3.3 Mounting and refrigeration

The SQUIDs are mounted in an adiabatic demagnetization refrigerator (ADR) for cooling to millikelvin temperatures. The ADR is a single shot cooling platform that relies on a pulse

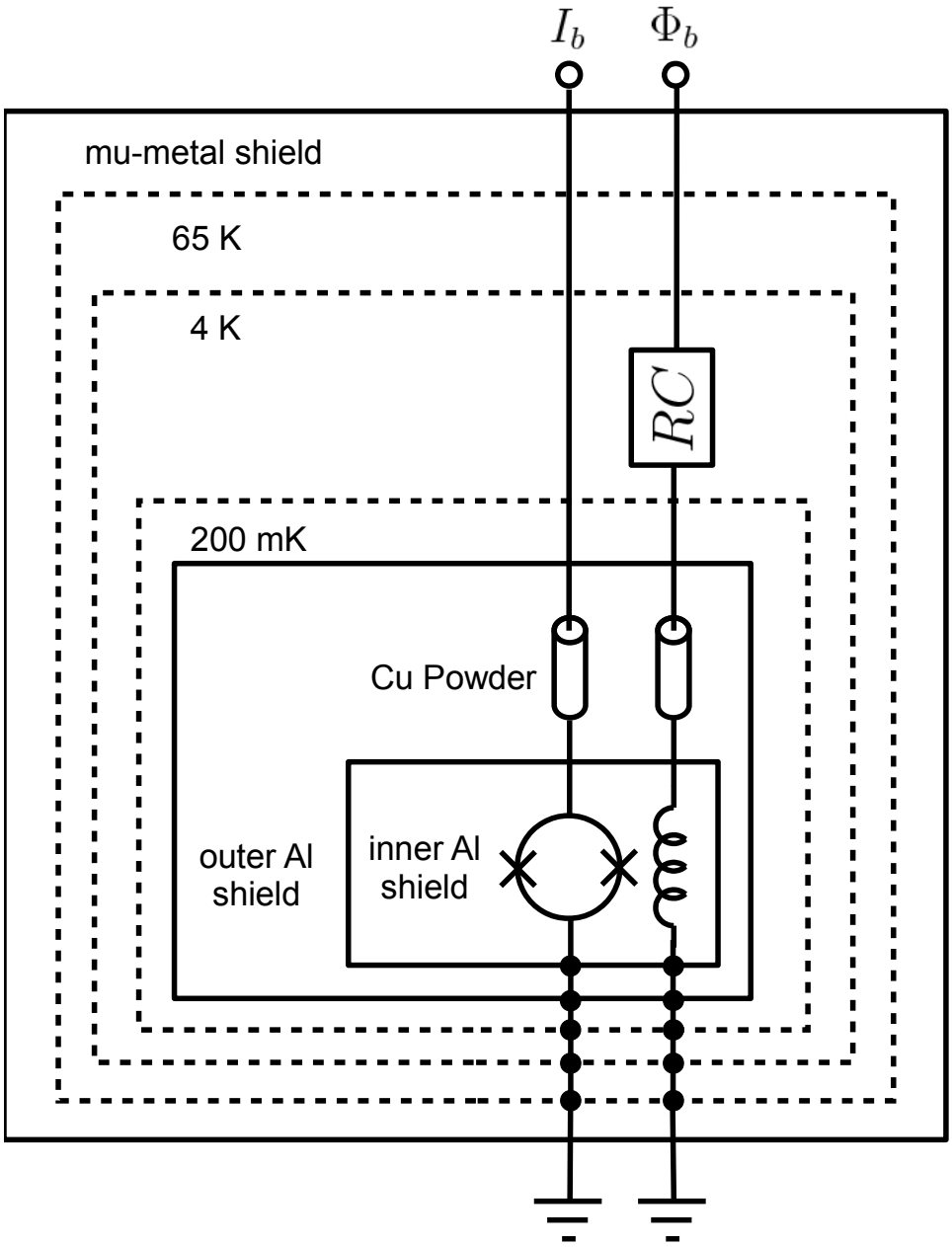

Figure 3.9: Fridge mount diagram. The SQUID is enclosed by two superconducting shield layers and one mu-metal layer. The bias lines are filtered with copper powder filters at the cold stage and, in the case of the flux line, an RC filter at 4 K.

tube cooler to reach a temperature of 4 K and the adiabatic demagnetization of a salt pill to cool down into the millikelvin range. Typical base temperatures of 50 mK are possible under full experimental heat load. The refrigerator can stay below 200 mK for a matter of a

few hours before it needs to be cycled to 4 K again and the salt pill remagnetized. A major advantage of the ADR is the easy temperature selection and ramping. By simply changing the current through the magnet, it is possible to reach and stabilize at any temperature between base and 4 K within a few minutes.

Due to the SQUIDs' very high sensitivity to magnetic fields, the devices need to be very well shielded, both from stray magnetic fields and from RF interference in the lines. The field screening is realized by multiple layers of shielding. There are two layers of superconducting aluminum, which provide excellent magnetic field attenuation below the transition temperature of aluminum ($\sim$1.2 K). There is also a single layer of high permeability mu-metal material surrounding the cryostat.

The control lines are heavily filtered to limit stray RF interference from getting down to the SQUID. There are two kinds of lines that attach to the SQUID: the current bias and the flux bias. Because of the need to minimize Johnson noise getting to the SQUID, very little resistance can be tolerated in the bias line. Thus, the bias lines pass through a copper powder filter stage, which attenuates high frequency fields using eddy current losses in an inductively coupled powder and does not require a large series resistance. The flux bias line is more flexible. This line is filtered with a copper powder filter as well, but also with a normal *RC* filter at 4 K.

Bibliography

[1] D. McCumber, Journal of Applied Physics **39**, 3113 (1968).

[2] W. Stewart, Appl. Phys. Lett. **12**, 277 (1968).

[3] M. Tinkham, *Introduction to superconductivity* (Dover Publications, 31 East 2nd Street, Mineola, NY 11501-3852, 2004).

[4] C. Tesche and J. Clarke, Journal of Low Temperature Physics **29**, 301 (1977).

[5] J. Clarke, Proceedings of the IEEE **77**, 1208 (1989).

Chapter 4

Surface magnetism in the dc SQUID

This chapter details experiments that, for the first time, showed direct experimental evidence for a high density of unpaired spins on the surface of SQUIDs of order $\sigma_s \approx 5 \times 10^{17}$ /m^2 [1].

4.1 Temperature dependent flux in the SQUID

At temperatures below ~ 500 mK on Nb SQUIDs, we observed a surprising dependence of the quasistatic magnetization threading the SQUID on temperature. In this temperature range, the flux threading the SQUID scales as $1/T$, strongly reminiscent of Curie law behavior of paramagnetic spins. We interpret this as evidence of unpaired spins on the surface of the SQUID and have estimated the spin density from the magnitude of the response. Furthermore, the magnitude of the change depends linearly on the number of trapped vorticies in the films allowing a quantitative measurement of spin density.

4.1.1 Experimental setup

The setup for this experiment was the two SQUID amplifier described in Section 3.6. The basic picture of the experiment is a simple one: lock the SQUID at a high temperature and slowly lower the temperature, recording the flux changes as the temperature is decreased. Because there are two SQUID fluxes changing simultaneously, there is not enough information in this simple picture to separate the contributions from each device. It is possible, however, to separate the two contributions by tracing out a few periods of the $I - \Phi$ curve of the first stage SQUID and following the shifts in the extrema of that curve.

A flux drift in the first stage SQUID will cause the $I - \Phi$ curve to shift along the Φ axis because the flux through the first stage is the sum of the external flux sweeping out the curve and the flux from the unpaired spins of that device. A flux drift in the second stage SQUID will cause a shift in the I axis of the $I - \Phi$ curve because the flux threading that device is the sum of the first-stage current coupled through the coupling coil and that device's unpaired spins.

The flux was swept out with a function generator and the resulting FLL output (proportional to I) was digitized and recorded for later processing. One full $I - \Phi$ curve was recorded for each temperature in increments of 1 mK from 500 mK to the base temperature of the ADR, which was ~ 90 mK.

To determine the most accurate minimum of the $I - \Phi$ curve, several points near the absolute minimum were fit with a parabola and the minimum of that parabola was derived from the coefficients of the quadratic form, which was then used in plotting the data.

4.1.2 Field cool experiments

Typically, in a system that obeys a Curie law, there is some orienting field that supplies the $1/T$ signature. These experiments on flux drift in SQUIDs, however, are done in a very

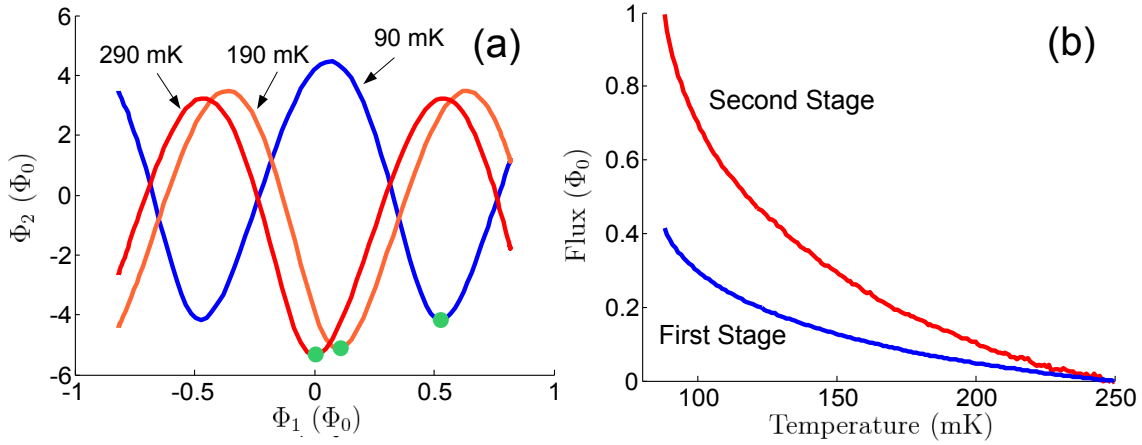

Figure 4.1: 3 $I - \Phi$ curves taken at different temperatures. The minima are highlighted in green. The flux changes derived from the movement of the minima are plotted in (b) for both devices.

low field. The field is likely to be not precisely zero due to influence of the large magnet that controls the ADR, even though the device is heavily shielded with superconductors. It is also possible that there is some magnetic material in the connections - particularly the brass SMA connectors themselves - which could provide an offset field. To study the field dependence, we affected the orienting field by trapping vorticies in the film before cooling.

A vortex will only appear in a type II superconductor where the coherence length ξ is relatively short compared to the penetration depth λ. In this situation, the formation energy for a boundary surface between a normal metal region and a superconducting region is negative. This implies that a magnetized superconductor will tend to break into superconducting and normal domains above some critical field H_{c1} significantly lower than the pair breaking critical field H_{c2} [2, 3]. The normal domain in a type II superconducting plane with applied magnetic field perpendicular to the surface will take the shape of a cylinder to maximize the size of the surface, and therefore, the energy gain. The radius of the normal core will be of order ξ, the coherence length, and contain the minimum possible flux, 1 Φ_0. A supercurrent will circulate around the normal core such that it creates a magnetic field in the same direction as the applied field. This vortex current circulates out to a radius of $\sim \lambda$,

the penetration depth. When a thin film type II superconductor is cooled from above T_c to below with a field B_{fc} applied ($B_{fc} > H_{c1}$), the field will be carried below T_c by vorticies, each vortex carrying one flux quantum. Thus, vortex density can be calculated from the cooling field [4, 5]:

$$\sigma_v = B_{fc}/\Phi_0. \tag{4.1}$$

Vorticies experience a Lorentz force from currents flowing in the superconductor, which can cause them to move. Vortex motion causes dissipation, and it can also cause flux noise in SQUIDs. Typically, however, vorticies become pinned to defects in the superconductor and contribute negligible noise at temperatures below the characteristic pinning energies. Typical pinning energies in Nb thin films are on the order of 10 meV [6], well above the thermal energy of our experiments. Thus, once below T_c, the field can be removed, and the vorticies will remain trapped. Spins near the surface inside a vortex core will experience the additional field of the vortex and tend to align with it.

The field is applied to either SQUID by means of the flux bias coil. To change the vortex density, the device must be warmed back above T_c, which, for our Nb devices, is $\sim$ 9 K. An experimental cycle for one field is as follows: first, warm the device to $\sim$ 15 K to make sure it is completely normal conducting by turning off the pulse tube cooler to the ADR and allowing the temperature to drift up. Then, apply the desired field and turn the cooling back on. Leave the field applied until the pulse tube returns to base temperature $\sim$ 4 K. Here, the device is well below T_c, so remove the field. Next, bias the SQUIDs and lock the flux locked loop. Finally, slowly cool the device to base temperature using the adiabatic cooling, recording the $I - \Phi$ curve the entire way. The entire process takes about 2 hours.

It was found that the cooling field, and therefore the vortex density, strongly affects the size of the magnetization signal at low temperature. Both positive and negative fields can be applied and the signal can grow and even reverse. Here, we plot the change in flux from

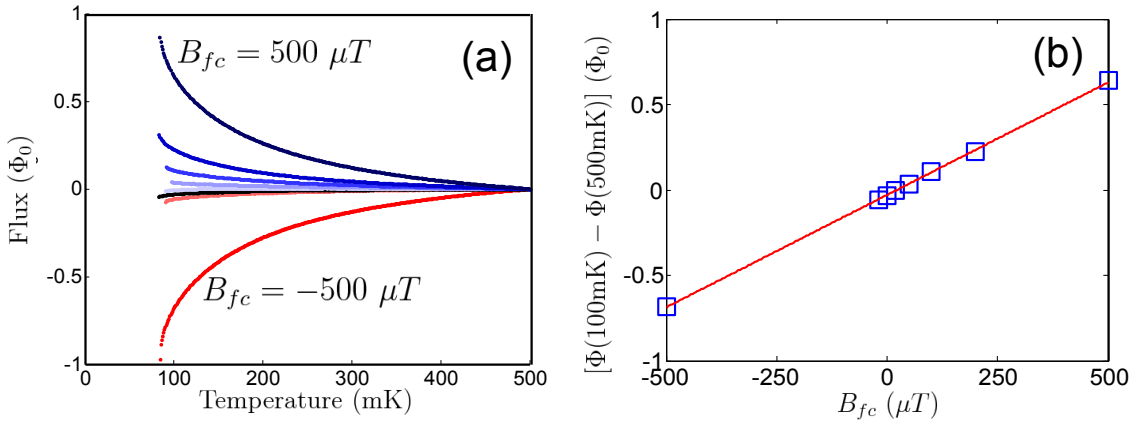

Figure 4.2: Individual flux *vs.* temperature curves for several cooling fields are plotted in (a). The change in flux *vs.* cooling field is shown in (b), and they all lie on a straight line.

500 mK to 100 mK as a function of cooling field, and the data fall on a line. A linear fit gives a slope of 1.3 Φ_0/mT. This can be used to estimate the density of spins as described below.

4.2 Calculation of surface spin density

We interpret the data to represent the paramagnetic response of unpaired spins near the surface of the superconductor, which is enhanced in the local strong fields of trapped vorticies. The crucial facts that lead to the measured effect are two fold. First, the spins clearly couple flux to the vorticies; however, the vorticies must maintain a constant 1 Φ_0 to satisfy the quantization condition. The extra flux from the spins forces the vortex currents to redistribute. Second, this current redistribution takes place within the boundary conditions of the SQUID. The vortex current drops off relatively slowly from the center and, inevitably, some of that current circles around the SQUID loop and couples flux to the SQUID. Thus, a spin couples to the SQUID through the vortex currents. The calculation, therefore, begins by calculating the coupling of a spin to a vortex and then calculating the coupling of a vortex

to the SQUID. Before treating that calculation in detail, we introduce a calculation tool, which is useful in the later sections.

4.2.1 Current distribution in a superconducting washer

The most general method to calculate a current distribution in a superconductor system solves a system of two equations, Ampere's law and London's equation:

$$\nabla \times \vec{B} = \mu_0 \vec{J} \tag{4.2}$$

and

$$\nabla \times \vec{J} = -\frac{1}{\mu_0 \lambda^2} \vec{B}, \tag{4.3}$$

where $\lambda = (m/\mu_0 n_s e^2)^{1/2}$ is the penetration depth of the superconductor. These equations together define a unique $\vec{B}$ and $\vec{J}$ for every point if some boundary conditions are specified.

For the case of the SQUID washer and the vortex, which are to be considered specifically for this problem, we construct a simplified geometry. We consider a thin circular washer with outer radius r_o, and inner radius r_i. The washer is discretized according to its symmetry by breaking it into concentric rings with width and spacing w. From this, the Maxwell equation (Equation 4.2) can be simplified [7].

The problem is radially symmetric, so the vector potential $\vec{A}(x)$ at radius x due to a current I flowing through a loop at radius r is given by:

$$\vec{A}(x) = \frac{\mu_0}{4\pi} I \oint \frac{r d\vec{\theta}}{\sqrt{(x - r\cos\theta)^2 + (r\sin\theta)^2}}. \tag{4.4}$$

The direction parallel to the radius vector integrates to zero, leaving only the tangential direction. The flux enclosed by a loop at radius x can be calculated by integrating the

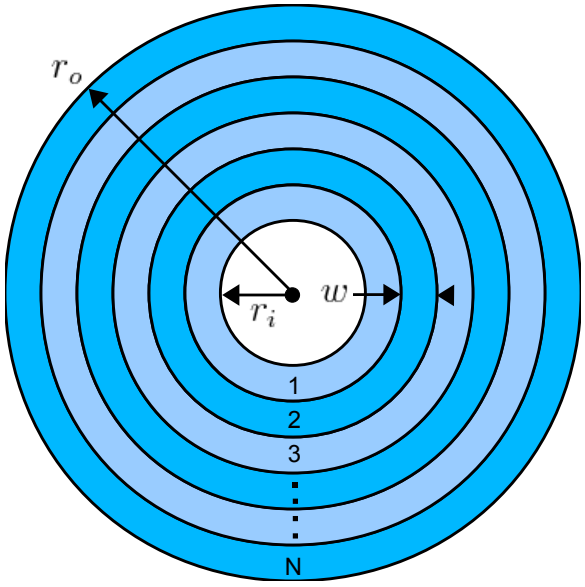

Figure 4.3: SQUID washer model. The washer is modeled as a circular washer of radius r_o with a hole of radius r_i. The washer is then separated into N strips of width w such that there are no gaps, $Nw = r_o - r_i$.

magnetic vector potential around the loop, giving:

$$\phi(x) = 2\pi x|\vec{A}(x)| \tag{4.5}$$

$$= \pi x \mu_0 I A_c(x/r) \tag{4.6}$$

$$A_c(x/r) = \oint \frac{\cos\theta d\theta/2\pi}{\sqrt{(x/r - \cos\theta)^2 + \sin^2\theta}}. \tag{4.7}$$

This integral can be performed in terms of elliptic integrals of the first kind (K) and second kind (E).

$$A_c(x/r) = \frac{1}{\pi\sqrt{x/r}}\left[\left(\frac{2}{k} - k\right)K(k) - \frac{2}{k}E(k)\right], \tag{4.8}$$

where

$$k \equiv \sqrt{\frac{4x/r}{(1+x/r)^2}}. \tag{4.9}$$

With this identification of a flux due to a current, a mutual inductance can be defined

between two loops. If loop i is at radius x, and loop j is at radius r, then

$$M_{ij} = \pi\mu_0 x \frac{A_c([x + w/2]/r) + A_c([x - w/2]/r])}{2}, \tag{4.10}$$

where the finite width of the loops has been taken into account by averaging over the width of the loop and evaluating the vector potential in the center of the loop. If the current in each loop is represented in a vector $\vec{i}$, the induced flux, $\vec{\phi}$, is given by:

$$\vec{\phi} = M_{max}\vec{i}. \tag{4.11}$$

So far, this represents the contribution from the Maxwell equation (Equation 4.2). The contribution of the London equation (Equation 4.3) is as follows. From the definition of the magnetic vector potential we have:

$$\vec{B} = \nabla \times \vec{A}. \tag{4.12}$$

Inserting this into the London equation, we find, by equating the argument of the curl operators that:

$$\vec{J}(x) = -\frac{1}{\mu_0\lambda^2}\vec{A}(x), \tag{4.13}$$

where x is the radius of the current loop. Again, by integrating the magnetic vector potential around the loop, we obtain the flux through it:

$$\phi(x) = 2\pi x|\vec{A}(x)| \tag{4.14}$$

$$= -2\pi x\mu_0\lambda^2|\vec{J}(x)| \tag{4.15}$$

$$= -\mu_0 2\pi x \left(\frac{\lambda^2}{dw}\right) I(x), \tag{4.16}$$

where d is the thickness of the film, and w is the width. This can be placed in the matrix

form of 4.11 with

$$(M_{lon})_{ij} = -\delta_{ij} 2\pi\mu_0 x \left(\frac{\lambda^2}{dw}\right), \tag{4.17}$$

where δ_{ij} is the Kronecker δ-function.

To solve for the current in each ring, one must evaluate:

$$\vec{I} = (M_{max} - M_{lon})^{-1}\vec{\phi}, \tag{4.18}$$

where the $\vec{\phi}$ represents the flux through each ring and acts like the boundary conditions which gives rise to a unique solution. The flux profile must be reasoned using some other method.

4.2.2 Coupling of surface spins to a vortex

To calculate the spin to vortex coupling, we rely again on the reciprocity theorem (Section 5.1). To apply this theory, we need to calculate the magnetic field at the position of the spin due to the vortex current.

We model the vortex as a superconducting washer with inner radius $r_i = \xi$ and outer radius $r_o \gg \xi$, where ξ is the coherence length. For the 80 nm thick Nb thin films in use here, we estimate that $\Lambda = 100$ nm and $\xi = 30$ nm.

The final defining feature of a vortex is that it contains a quantized flux equal to 1 Φ_0. This allows us to postulate that the flux vector from 4.18 is $\vec{\phi} = \vec{1}$ with one flux quantum threading each loop.

Performing the matrix inversion specified by Equation 4.18 yields the current distribution in the vortex, and from there, it is straightforward to calculate the field at any point in space with the Biot-Savart law. The in-plane $B_r(r, z)$ and out-of-plane $B_z(r, z)$ fields due to a single

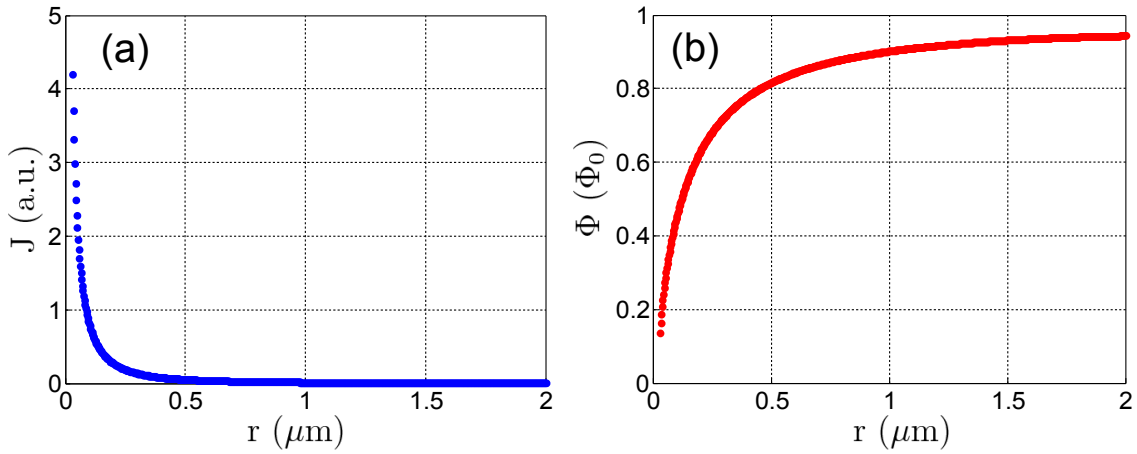

Figure 4.4: (a) shows the numerical solution of the vortex current as a function of radius from the core. (b) shows the total flux enclosed by a loop of a given radius. This shows the expected decay of the vortex current and the increase of the flux toward one flux quantum. Note that the flux does not reach 1, signifying a complete vortex, until a radius $r \gg 1$ μm. This shows the slow decay of the vortex current

loop with radius a centered at $r = 0$ in the $z = 0$ plane are as follows:

$$B_r(r,z) = -\frac{\mu_0 j z}{4\pi\sqrt{ar^3}}\left(K(j) - \frac{2-j^2}{2(1-j^2)}E(j)\right) \tag{4.19}$$

$$B_z(r,z) = \frac{\mu_0 j r}{4\pi\sqrt{ar^3}}\left(K(j) + \frac{j^2(r+a)-2r}{2r(1-j^2)}E(j)\right), \tag{4.20}$$

where, in this case,

$$j \equiv \sqrt{\frac{4r/a}{(1+r/a)^2+(z/a)^2}}. \tag{4.21}$$

The total field is the sum of the contributions for each current loop.

Now, by applying the reciprocity theorem, we calculate the flux coupled to the vortex by a spin at (r, z):

$$\phi_{s\to v} = \frac{B(r,z)}{I_v}\mu, \tag{4.22}$$

where $B(r,z) = [B_z(r,z)^2 + B_r(r,z)^2]^{1/2}$ is the magnitude of the field at (r,z), $I_v = \sum i$ is the total current in the washer, and μ is the effective moment of the spin. The expectation

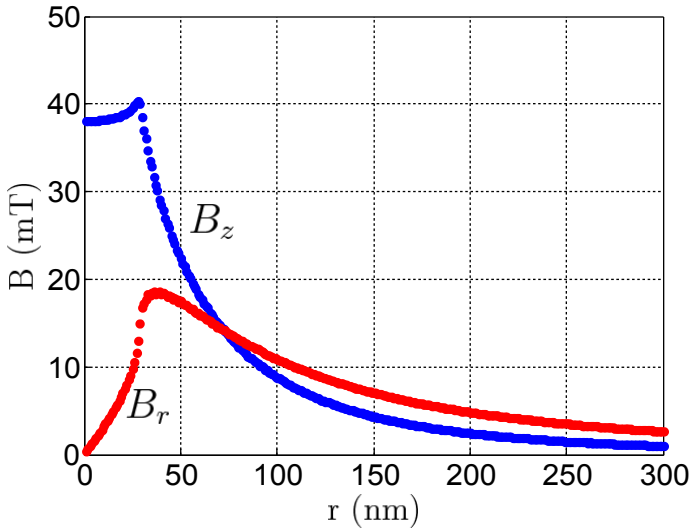

Figure 4.5: Vortex field distribution, in-plane and out-of-plane contribution

value of the magnetization of a spin 1/2 particle with magnetic moment μ_B in a magnetic field is well known to be temperature dependent and given by:

$$\langle \mu \rangle = \mu_B \tanh\left(\frac{\mu_B B(r,z)}{2k_B T}\right) \tag{4.23}$$

and therefore,

$$\Phi_{s\to v} = \mu_B L_v \frac{1}{\Phi_0} B(r,z) \tanh\left(\frac{\mu_B B(r,z)}{2k_B T}\right), \tag{4.24}$$

where I_v has been replaced by Φ_0/L_v introducing the vortex self inductance, which has the value $L_v = 0.24$ pH for these material parameters.

The total flux coupled to the vortex from spins with density σ_s is then:

$$\Phi_v(T) = \mu_B \sigma_s L_v \frac{1}{\Phi_0} \int 2\pi r B(r,z) \tanh\left(\frac{\mu_B B(r,z)}{2k_B T}\right) dr dz \tag{4.25}$$

$$= \mu_B \sigma_s L_v P_{eff}(T), \tag{4.26}$$

where

$$P_{eff}(T) = \frac{1}{\Phi_0} \int 2\pi r B(r,z) \tanh\left((\frac{\mu_B B(r,z)}{2k_B T} \right). \tag{4.27}$$

4.2.3 Coupling of a vortex to the SQUID

A vortex trapped in a SQUID washer couples some flux to the SQUID. The physical reason for this offset flux is the vortex current circulating around the hole in the SQUID washer. The vortex current is mostly confined to the region around the vortex core, but the decay is slow enough that a small part of the current will still find its way around the washer (see Figure 4.4).

We have developed the tools to calculate current distribution from a flux distribution above. To calculate the flux offset from a vortex, we employ an iterative technique to determine the applied flux needed to cancel the effect of a vortex. Because of the angular symmetry, a single vortex at radius r can be replaced by n vorticies of magnitude Φ_0/n positioned around the washer at radius r. As $n \to \infty$, this converges to a cut in the washer with a net flux through the cut of 1 Φ_0. With this, the presumed flux profile becomes:

$$\Phi(r') = \begin{cases} -f & r' < r \\ \Phi_0 - f & r' > r \end{cases} \tag{4.28}$$

where f is the compensating offset flux. The value of f which represents full cancellation is the one that results in zero total circulating current:

$$\sum i = 0. \tag{4.29}$$

For each value of r, the current distribution is calculated using Equation 4.18 with the flux vector defined by Equation 4.7. In this case, the penetration depth, λ, is much smaller than

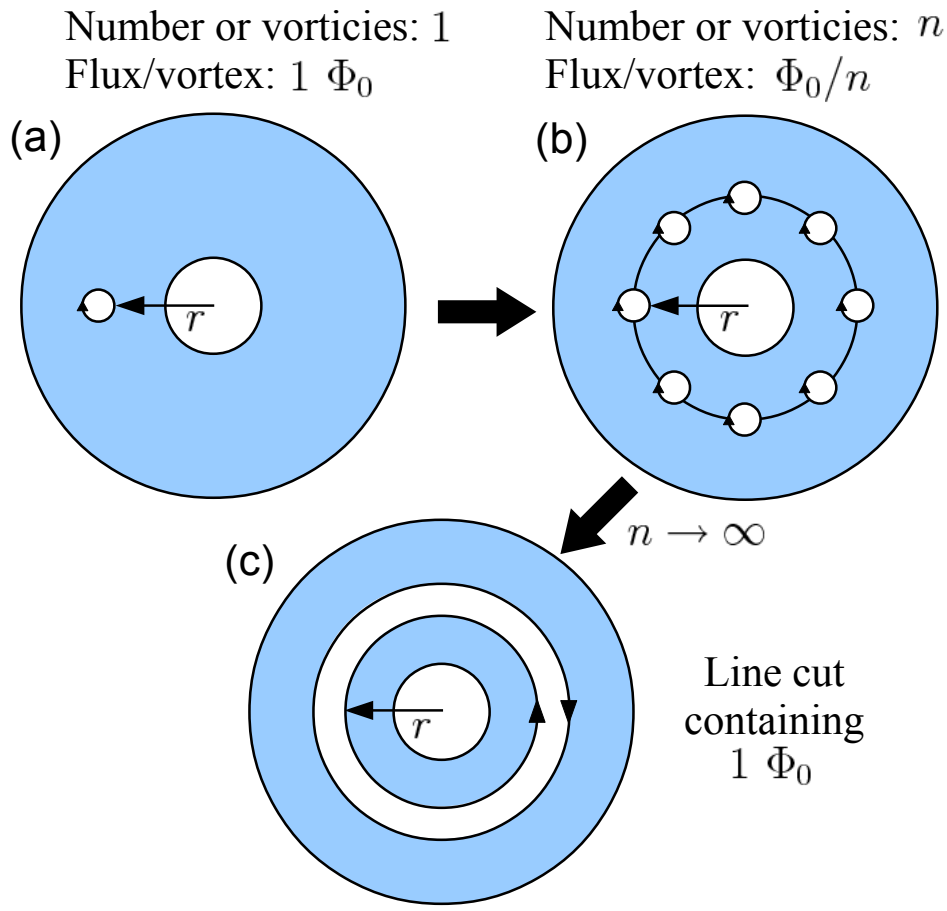

Figure 4.6: In (a) there is one vortex containing 1 Φ_0 at radius r. This is equivalent to (b) where there are n vorticies at radius r, each containging Φ_0/n flux. As $n \to \infty$ in (c), the vorticies converge to a line cut containing 1 Φ_0.

the dimensions of the washer, therefore the London contribution is neglected. This procedure results in an offset flux as a function of radius $f(r)$.

For a given washer geometry, then, it is possible to compute an average flux offset for uniformly distributed vorticies, $\langle f(r_i, r_o)\rangle$:

$$\langle f(r_i, r_o)\rangle \equiv \frac{\int_{r_i}^{r_o} 2\pi r f(r)}{\pi(r_0^2 - r_i^2)}. \tag{4.30}$$

It is clear that a vortex near the inner radius couples $\sim 1\ \Phi_0$ to the SQUID, and a vortex

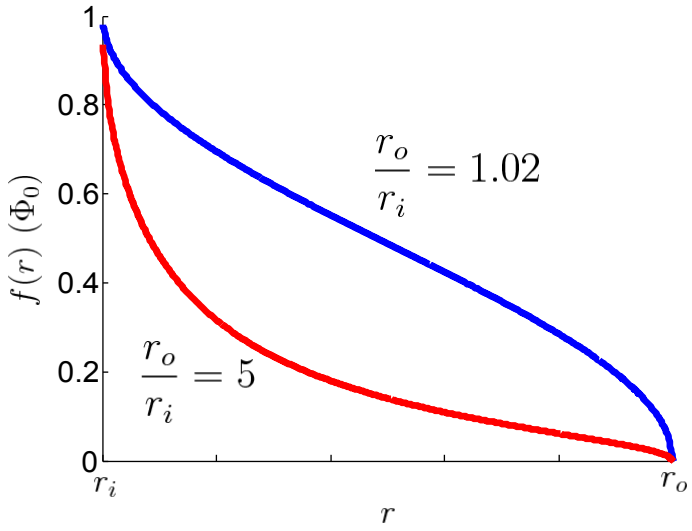

Figure 4.7: Flux offset as a function of radius for a vortex in a washer. The blue curve is the result for a narrow linewidth device, and red is for the washer with the aspect ratio of the experiment.

at the far edge couples $\sim 0\ \Phi_0$ to the SQUID. Thus, for a thin linewidth washer, one expects an average offset $\langle f \rangle = 0.5\ \Phi_0$, and indeed, this is the result of the numerical calculations. For the geometry used for the experiment, we find an average flux offset of

$$\langle f \rangle = 0.14\ \Phi_0. \tag{4.31}$$

4.2.4 Calculation of surface spin density

Upon cooling the spins, they begin to polarize in the vortex field, coupling a flux to the vortex according to Equation 4.25. This couples an average flux to the SQUID according to Equation 4.31. The total flux change coupled to the SQUID is therefore:

$$\Delta\Phi = 0.14 A_{SQ} \sigma_v \mu_B \sigma_s L_v \Delta P_{eff}, \tag{4.32}$$

where A_{SQ} is the area of the SQUID. For these experiments, the vortex density σ_v is related to the cooling field B_{fc} as $\sigma_v = B_{fc}/\Phi_0$. Now we can relate the measured flux change to the spin density as:

$$\frac{\Delta\Phi}{B_{fc}} = 0.14\frac{A_{SQ}}{\Phi_0}\mu_B\sigma_s L_v \Delta P_{eff}. \tag{4.33}$$

For our material parameters, $\Delta P_{eff} \equiv P_{eff}(100\text{ mK}) - P_{eff}(500\text{ mK}) = 0.037$. Using $A_{SQ} = 0.96\text{ mm}^2$ and the slope $\Delta\Phi/B_{fc} = 1.3\ \Phi_0/\text{mT}$, the spin density is observed to be $\sigma_s = 5.0 \times 10^{17}\ \text{m}^{-2}$.

Other experimenters have shown similar spin densities on many other materials. Bluhm *et al.* used a scanning SQUID microscope to measure spin susceptibility at temperatures below 1 K [8]. They found a paramagnetic $1/T$ like dependence indicative of unpaired spins. Also, experiments on spin-flip scattering in superconducting nanowires have measured a magnetic defect density with a similar density of defects [9]. These experiments involve using a magnetic field to quench the magnetic defects and thereby enhance superconductivity. It is now widely believed that these surface spins are the origin of $1/f$ noise is SQUIDs and qubits.

4.3 Temperature dependent flux narrow line width devices

Spin interactions are impossible to estimate in the presence of a large number of vortices due to the much higher energy interaction of the spin with the vortex. For this reason, it is necessary to perform the field cool experiment on a film with no vortices trapped. This condition is relatively simple to achieve by making the linewidths of the SQUID washer very narrow. It has been shown that if a superconductor is cooled in a field lower than some threshold field $B_{th} \approx \Phi_0/w^2$ where w is the width of the line, then it is energetically

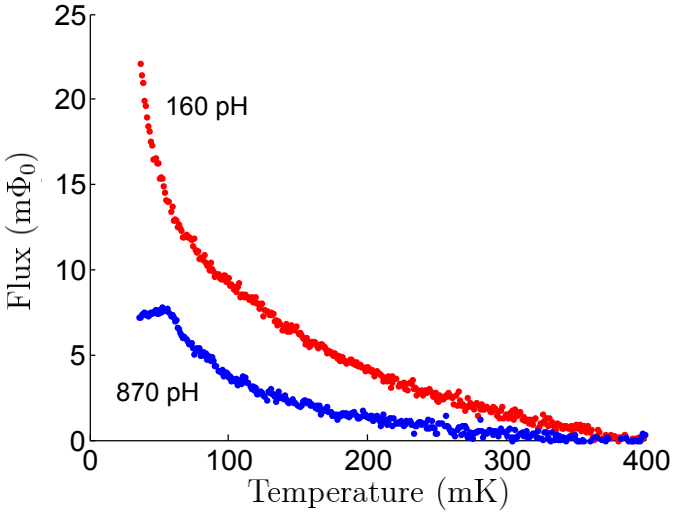

Figure 4.8: Flux change for narrow linewidth devices. Note the cusp at low temperature.

unfavorable to nucleate vortices [4].

To achieve this, we have fabricated SQUIDs with narrow (2 μm) lines. For these devices, the threshold field $B_{th} \approx 500$ μT, which is well above any background field. Data on these devices show typical flux vs. temperature curves with $1/T$ dependence at low temperature, but there is some cool down to cool down variability.

From this data, we can estimate the spin interaction energy by comparing the observed polarization to the maximum polarization. The maximum polarization can be estimated assuming the spins are all fully polarized and optimally oriented radially on the SQUID washer. Then:

$$\Phi_{max} = 2\mu_0\mu_b\sigma_s d, \tag{4.34}$$

were d is the diameter of the loop [10]. For this SQUID, $d = 50$ μm and the relation yields $\Phi_{max} = 280$ mΦ_0, whereas the measured flux change is $\sim$20 mΦ_0. This suggests a high degree of spin polarization at already 30 mK, which suggests an interaction energy of the same order.

Additionally, in a small number of devices we have seen a feature at the lowest temperatures very reminiscent of the cusp in the susceptibility of a spin glass at the spin glass freezing temperature (see Section 5.5.1). This highlights the importance of interactions and suggests the possibility of spin glass physics playing a role in $1/f$ noise. Notably, the Faoro and Ioffe model [11], which relies on RKKY interactions, predicts an interaction strength of 20 mK for the spin density derived here. RKKY interactions between spins are also capable of forming a spin glass.

Bibliography

[1] S. Sendelbach, D. Hover, A. Kittel, M. Mück, J. Martinis, and R. McDermott, Phys. Rev. Lett. **100**, 227006 (2008).

[2] J. Williams, *Superconductivity and its applications*, *Applied physics series* (Pion, 1970).

[3] M. Lang and J. Müller, *The Physics of Superconductors* (Springer-Verlag, 2003).

[4] G. Stan, S. B. Field, and J. Martinis, Phys. Rev. Lett. **92**, 097003 (2004).

[5] M. Tinkham, *Introduction to superconductivity* (Dover Publications, 2004).

[6] J. Gail, M. Mück, and C. Heiden, Appl. Phys. Lett. **73**, 2663 (1998).

[7] S. Sendelbach, D. Hover, A. Kittel, M. Mück, J. Martinis, and R. McDermott, arXiv preprint arXiv:0802.1511 (2008).

[8] H. Bluhm, J. Bert, N. Koshnick, M. Huber, and K. Moler, Phys. Rev. Lett. **103**, 26805 (2009).

[9] T. Wei, D. Pekker, A. Rogachev, A. Bezryadin, and P. Goldbart, EPL (Europhysics Letters) **75**, 943 (2007).

[10] R. Bialczak, R. McDermott, M. Ansmann, M. Hofheinz, N. Katz, E. Lucero, M. Neeley, A. O'Connell, H. Wang, A. Cleland, and J. Martinis, Phys. Rev. Lett. **99**, 187006 (2007).

[11] L. Faoro and L. B. Ioffe, Phys. Rev. Lett. **100**, 227005 (2008).

Chapter 5

Theoretical models for $1/f$ flux noise from surface spins

With the identification of a high density of unpaired spins on the surface of the SQUID, the origin of flux noise begins to take shape in terms of fluctuating surface spins. Models of $1/f$ noise from unpaired spins on the surface of superconductors are very attractive for several reasons: the spin origin is not specifically material dependent; surface spins are local, which yields the correct scaling of noise with area; the R/r scaling with aspect ratio is very naturally obtained (see Section 5.1); the $1/f$ shape has a reasonable explanation for non-interacting spins (see Equation 2.2); and the magnitude of the noise calculated from surface spins with the measured density gives approximately the right value for even simple models (see Equation 5.5).

5.1 Reciprocity and area scaling

A feature of the independent spin model for surface spins is that it very naturally reproduces an independence of the flux noise magnitude on the overall scale of the device. The

noise magnitude only ends up depending on the aspect ratio of the SQUID loop and not the overall sensing area. A fluctuating spin on the surface of a SQUID will couple a fluctuating flux to the device. The magnitude of that flux can be conveniently calculated with the help of the reciprocity theorem and a simplified model for the geometry of the SQUID. The reciprocity theorem states that the mutual inductance from one current loop to another is identically equal to the mutual inductance from the other loop back to the first ($M_{12} = M_{21}$). In this situation, we are interested in how much flux is coupled to a SQUID loop from a spin. The magnetic moment of a spin is modeled as some small equivalent current loop I_{eff} with effective area A_{eff}, such that $\mu = I_{eff}A_{eff}$. Now, applying the reciprocity theorem:

$$\Phi_{spin \to SQUID} = \frac{B}{I}\mu, \tag{5.1}$$

where B is the magnetic field at the location of the spin due to a test current I in the SQUID.

Thus, the flux coupled to the SQUID from a spin can be calculated if it is possible to calculate the magnetic field at the location of the spin due to a test current in the SQUID. The most convenient geometry for this that still retains some contact with the physical situation is a torus. Consider a torus with outer diameter R and wire radius r. Then the field at the surface will be constant and can be calculated with Amperes law

$$\frac{B}{I} = \frac{\mu_0}{2\pi r} \tag{5.2}$$

implying

$$\Phi_{spin \to SQUID} = \frac{\mu_0 \mu}{2\pi r}. \tag{5.3}$$

A further assumption is that the spins are able to rotate freely. In this situation, they will tend to align themselves to the field that is ever present due to small bias currents running through the SQUID when it is operating. This optimally couples the spins to the SQUID.

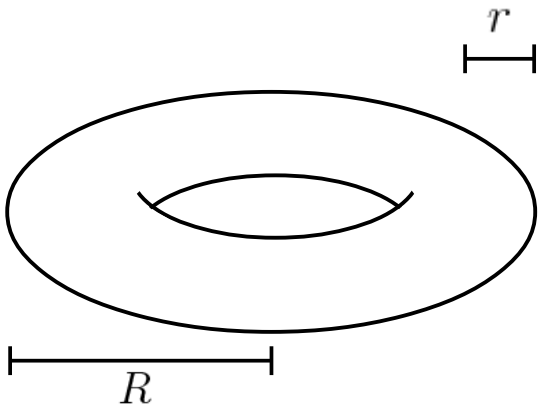

Figure 5.1: SQUID geometry simplified to a torus with outer diameter R and wire radius r.

5.2 Flux noise power estimation

With just these assumptions, it is possible to estimate the flux noise power. If the spins are then assumed to be uniformly distributed across the surface with a density σ, and if the magnetic moment of a spin is taken to be one Bohr magneton, then the total flux noise magnitude is:

$$\langle \phi^2 \rangle = \left(\frac{\mu_0 \mu_B}{2\pi r} \right)^2 \sigma (2\pi R)(2\pi r) = \mu_0^2 \mu_B^2 \sigma \frac{R}{r}. \tag{5.4}$$

In particular, the noise is expected to scale as R/r, which is independent of the overall scale of the device. In a more realistic geometry, this model only experiences small logarithmic corrections [1]. This scaling has been observed in some qubits [2]. Combining Equation 5.4 with the result for the frequency dependence (Section 2), we can generate an estimate for the flux noise power spectrum. By keeping all the appropriate scaling factors in $S(\omega)$ and converting to normal frequency single sided spectrum, we obtain:

$$S_\Phi(f) = \langle \phi^2 \rangle \cdot 2 \cdot 2\pi \cdot S(2\pi f) = k_B T D(E) \mu_0^2 \mu_B^2 \frac{R}{r} \sigma \frac{1}{f}. \tag{5.5}$$

With input from experimental observations, we can estimate the density of states through the range of relaxation times. By substituting the presumed relationship between τ and E (Equation 2.3) into 5.5:

$$D(E) = \frac{1}{E_2 - E_1} \tag{5.6}$$

$$= \frac{1}{k_B T \ln(\tau_2/\tau_1)}. \tag{5.7}$$

Then 5.5 becomes:

$$S_\Phi(f) = \frac{\mu_0^2 \mu_B^2}{\ln(\tau_2/\tau_1)} \frac{R}{r} \sigma \frac{1}{f}. \tag{5.8}$$

For example, if $\tau_2/\tau_1 = 10^{10}$, $R/r = 10$, and $\sigma = 5 \times 10^{17}/\mathrm{m}^2$, then $S_\Phi(1\mathrm{Hz})^{1/2} = 2.7\ \mu\Phi_0/\sqrt{\mathrm{Hz}}$, which is very compatible with the measured value for flux noise in SQUIDs. Note that temperature dependence remains because τ_2, τ_1 are temperature dependent. The independent spin model explains most of the features of the noise identified by Wellstood; however, it says nothing about the origin of the spins. Recent experiments have also cast significant doubt on the tenability of the non-interacting picture of the spins [3].

5.3 MIGS

The origin of the surface spins is still unresolved. One explanation proposed by Choi, *et al.* [4] attempts to explain the origin of the spins in terms of Metal Induced Gap States (MIGS). MIGS form at interfaces between metals and insulators where the wave function of the electron is able to leak into the insulator because the energy barrier is not infinite. The wave function decays exponentially in this region, much like an evanescent wave in electrodynamics. However, under certain conditions of disorder at the interface, the tail of the wave function can localize and form a paramagnetic spin. This is a very attractive theory

because of its universal nature; any metal and insulator with appropriate disorder should theoretically produce these gap states.

It should be possible to test this theory by significantly reducing the disorder at the interface by fabricating an all-epitaxial device, but such fabrication is a technical challenge, and no results showing reduced noise have been produced. Additionally, the SQUIDs from this chapter have shown a reduction in noise by using a silicon nitride dielectric encapsulation. Such a material dependence is not predicted in the MIGS model. However, it may still be that there are MIGS at a lower level and perhaps they will ultimately limit flux noise performance.

5.4 Faoro/Ioffe model

Along with the Dutta and Horn model (Section 2) for independent spins, there have been a few more models proposed to explain low frequency flux noise in superconducting circuits. One considers electrons with fixed moments hopping between traps with a wide distribution of escape times [5]. Another considers spin flips of paramagnetic dangling bonds interacting with tunneling two level systems in an amorphous dielectric [6].

A more recent model by Laura Faoro and Lev Ioffe [7] proposes a theory based on spin diffusion on the superconductor surface facilitated by the RKKY interaction in the non-uniform surface field of a SQUID loop. This model will be elaborated on here.

The model considers unpaired spins on the surface of a superconductor that are coupled to one another by the RKKY interaction. The spins occupy fixed locations and experience random flips, which give rise to the fluctuating magnetic signal. The spin flips are not thermally driven; they are due to tunneling of pairs and, therefore, the characteristic time is set by the energy barrier, which in turn is set by the interaction energy between the spins. With this assumption, the spins always flip in pairs, the total magnetization of the system

is a conserved quantity, and the local magnetization obeys the diffusion equation

$$\left[\frac{d}{dt} - D\nabla^2\right] M(t,r) = 0, \tag{5.9}$$

where the diffusion constant D is related to the distance between spins r and the potential $V(r)$ as

$$D = r^2 < V^2(r) >^{1/2} . \tag{5.10}$$

Because magnetization is conserved, this mechanism would produce no noise if all spins were coupled equally to the SQUID. The noise in this model relies on the non-uniform distribution of current in a thin film superconductor to produce the necessary position-dependent couplings. The current peaks at the edges due to the penetration depth of the superconductor; therefore, spins at the edges are most strongly coupled to the SQUID. Faoro and Ioffe take this into account and derive a model of noise that is temperature independent and has approximately the correct magnitude:

$$S_\Phi = \frac{4}{\pi}(\mu_0\mu_B)^2\sigma_S\frac{R}{r}\frac{1}{f}. \tag{5.11}$$

Because it takes into account interactions between spins on a surface, this model currently explains many of the features of the noise that have been experimentally demonstrated. This model, however, does not explain the correlation between flux and inductance that has been observed in SQUIDs (Section 6.6.1).

5.5 Spin interactions and spin glasses

The experiments on inductance noise in SQUIDs (Section 6) indicates a high degree of coordination between spins. Other results on magnetization *vs.* temperature have shown

the existence of a cusp, which is very reminiscent of a spin glass at the freezing temperature 4.8. This section takes a look at the physics of interacting spins as it pertains to $1/f$ flux noise.

In the previous sections on the theory of $1/f$ noise, it was assumed that the spins were non-interacting. This is almost certainly untrue. Some attempts have been made to try to extend the model with some effects of interactions. At temperatures that are high relative to the interaction strength, the spins are paramagnetic and relatively uncorrelated. At low enough temperatures, however, spins tend to align with one another, forming a ferromagnet for positive interactions or an anti-ferromagnet for negative interactions. In these configurations, spin fluctuations are suppressed because spin flips are energetically unfavored in the lattice. Experiments on SQUIDs clearly indicate that the noise does not decrease at low temperatures [8], which is inconsistent with such long range magnetic order.

There is another possibility. If the interactions between spins can take a random sign, then it will be impossible for the spins to form any long range ferromagnetic or anti-ferromagnetic order. Systems like this exhibit some temperature T_G, called the freezing temperature, below which the magnetic moments are aligned in some correlated, but random, way [9]. This system is called a spin glass in analogy with the frozen disorder of an ordinary structural glass.

A natural and common interaction between spins near the surface of a superconductor that has the ability to form a spin glass is the RKKY interaction (for Ruderman-Kittel-Kasuya-Yosida, its discoverers). The RKKY interaction is an indirect exchange interaction between spins that is mediated by the conduction electrons. Each spin polarizes the electrons around it in the superconductor as the electrons attempt to screen the spin. These clouds of polarization exhibit oscillatory behavior, which decays relatively slowly. When the clouds overlap, their direct exchange interaction leads to an indirect interaction between the spins.

The RKKY interaction in a superconductor takes the following form [10]:

$$J(r) = \left[J_0 \frac{\cos 2k_F r}{r^3} \right] e^{-2r/\xi}, \tag{5.12}$$

where r is the distance between two spins, k_F is the Fermi wave vector in the metal, and $\xi = v_F/\Delta$. In metals, $k_F \sim a_0$ where a_0 is the lattice spacing. Equation 5.12 indicates that the *sign* of the interaction can change for spins whose separation is different by only one lattice constant. For a spin density of $5 \times 10^{17}/\mathrm{m}^2$, the average spin separation is ≈1 nm or $\sim 10\ a_0$, which indicates that randomly placed spins will have random signs of interaction and fulfill the basic condition for a spin glass. Noise from spin glasses exhibit many properties that are found in SQUIDs, including $1/f$ noise.

5.5.1 Spin glass susceptibility

Above T_G, the spins are in the paramagnetic state and are independently fluctuating. In this regime, the complex susceptibility $\chi(\omega) = \chi^{'}(\omega) + i\chi^{''}(\omega)$ for a single spin takes the form:

$$\chi(\omega)_\tau = \left(\frac{\mu_0 \mu_B^2}{k_B T} \right) \frac{1}{1 + i\omega\tau}. \tag{5.13}$$

where τ is the spin relaxation time. It is clear that both the static magnetization $\chi(0)$ and the real part of the frequency dependent susceptibility $\chi^{'}(\omega)$ increase as temperature is lowered. However, as the temperature approaches and goes below T_G, the system becomes frozen. The magnetic moments may be randomly oriented, but their relative orientation becomes fixed, which means that they are less able to align to applied fields and that the susceptibility starts to drop with decreasing temperature. This behavior forms a cusp in the magnetization. Such a cusp is a characteristic feature of the spin glass and has been observed in some SQUIDs [3].

The imaginary part of the frequency dependent susceptibility is notable in a spin glass for remaining finite, even at very small frequencies, which correspond to long times [9]. The imaginary part of the susceptibility is related to a phase shift during sinusoidal drive, which gives rise to dissipation.

It is also possible to define the imaginary susceptibility as a response to a step drive; this is called the relaxation function (see Equation 5.15). If a spin glass is cooled from above T_G to below with an applied field, and then that field is removed, the system will not relax immediately. The magnetization that is left is called remnant magnetization. The random nature of the coupling sign between the spins creates a very complicated potential energy landscape with many local minima of various depths. The system is always trying to relax to the global ground state, but it can get stuck for very long periods of time exploring local minima. It is found experimentally that the decay of the remnant magnetization on many spin glasses follows a logarithmic law [11]:

$$M(t) = M_1 - m \ln(t/t_1), \tag{5.14}$$

where t_1 and M_1 are the initial time and magnetization, respectively, and m is a constant that depends on temperature. The law will hold until some maximum time t_{max}.

5.5.2 $1/f$ noise in spin glasses

If a logarithmic relaxation is assumed for magnetization in a spin glass, it can be shown [12] that the magnetization noise (and therefore the flux noise in a SQUID) have a $1/f$ spectrum. This is done by formulating the fluctuation-dissipation theorem in terms of the relaxation function:

$$S_M(f) = \frac{2k_BT}{\pi f} \int_0^\infty \sin(2\pi f) \left[-\frac{d}{dt} \frac{M(t)}{H_0} \right] \mathrm{d}t, \tag{5.15}$$

where H_0 is the initial magnetizing field. Inserting 5.14 into 5.15, the result for the spectrum follows as:

$$S_M(f) = \frac{k_B T m}{H_0} \frac{1}{f}, \tag{5.16}$$

where the result is valid for $t_{max}^{-1} \ll 2\pi f \ll t_1^{-1}$. Magnetic spectra with a $1/f$ spectrum have indeed been measured in spin glass systems [13].

5.5.3 Spin susceptibility above T_G

Most of the effects of a spin glass are observed, naturally, below the spin freezing temperature T_G. There are, however, some effects that have been observed in canonical spin glasses, such as CuMn, at temperatures well above T_G. In particular, the susceptibility shows some regular deviations from pure paramagnetic Curie law behavior. Similar effects have been observed in SQUIDs [3] in the form of jumps in the susceptibility in the direction of increasing susceptibility as the temperature is lowered.

A purely paramagnetic system will have a susceptibility that is proportional to the square of the size of the spin magnetic moment μ_B^2, and inversely proportional to temperature (see Equation 5.13). However, when the susceptibility was measured on CuMn [14], it was found that the susceptibility of the spin glass departed from the Curie law in the direction of increasing susceptibility as temperature was lowered. This is interpreted as an increase in the effective magnetic moment of the spins due to ferromagnetic clustering. This clustering is a precursor to the freezing that will happen at T_G. The effective moment can be calculated from the susceptibility from the following equation:

$$p(T) = \frac{N\mu_B^2}{3k_B} \left[\frac{\mathrm{d}(\chi^{-1})}{\mathrm{d}T} \right]^{-1/2}. \tag{5.17}$$

The data clearly show that as the temperature is lowered, the effective moment increases

rapidly as T_G is approached [14]. A spin glass in which ferromagnetic couplings are predominant and the effective moments are very large is often referred to as a mictomagnet, or a cluster glass [15]. These arise at relatively high concentrations of magnet moments, roughly 10 atomic percent, and are often considered separately from spin glasses.

Bibliography

[1] R. Bialczak, R. McDermott, M. Ansmann, M. Hofheinz, N. Katz, E. Lucero, M. Neeley, A. O'Connell, H. Wang, A. Cleland, and J. Martinis, Phys. Rev. Lett. **99**, 187006 (2007).

[2] T. Lanting, A. Berkley, B. Bumble, P. Bunyk, A. Fung, J. Johansson, A. Kaul, A. Kleinsasser, E. Ladizinsky, F. Maibaum, R. Harris, M. Johnson, E. Tolkacheva, and M. Amin, Phys. Rev. B **79**, 060509 (2009).

[3] S. Sendelbach, D. Hover, M. Mück, and R. McDermott, Phys. Rev. Lett. **103**, 117001 (2009).

[4] S. Choi, D. Lee, S. Louie, and J. Clarke, Phys. Rev. Lett. **103**, 197001 (2009).

[5] R. H. Koch, D. P. DiVincenzo, and J. Clarke, Phys. Rev. Lett. **98**, 267003 (2007).

[6] R. de Sousa, Phys. Rev. B **76**, 245306 (2007).

[7] L. Faoro and L. B. Ioffe, Phys. Rev. Lett. **100**, 227005 (2008).

[8] F. Wellstood, C. Urbina, and J. Clarke, Appl. Phys. Lett. **50**, 772 (1987).

[9] S. Kogan, *Electronic Noise and Fluctuations in Solids* (Cambridge University Press, 1996).

[10] V. M. Galitski and A. I. Larkin, Phys. Rev. B **66**, 064526 (2002).

[11] P. Nordblad, P. Svedlindh, L. Lundgren, and L. Sandlund, Phys. Rev. B **33**, 645 (1986).

[12] S. Kogan, Solid State Communications **38**, 1015 (1981).

[13] M. Ocio, H. Bouchiat, and P. Monod, Journal of Magnetism and Magnetic Materials **54**, 11 (1986).

[14] A. Morgownik and J. Mydosh, Phys. Rev. B **24**, 5277 (1981).

[15] J. Mydosh, *Spin Glasses: An Experimental Introduction* (Taylor & Francis, 1993).

Chapter 6

Inductance Noise

Once it has been determined that the likely source of $1/f$ noise in superconducting thin film is the fluctuation of paramagnetic spins on the metal surface, it is reasonable to attempt to gain more information about the spin system by measuring the AC susceptibility of the spin system. In this chapter, we explore the complex frequency and temperature dependent susceptibility of surface spins using SQUIDs.

6.1 AC Susceptibility

Sample magnetic moments can rotate to align with applied magnetic fields. It takes a finite amount of time for a rotation to occur, and this characteristic time carries information about the spin environment. A purely DC measurement will not give any information about this characteristic response time, so an AC measurement is required.

The basic idea of the AC susceptibility measurement is to apply a sinusoidally varying magnetic field, $H(t) = H_{ac}\sin(\omega t)$, to the sample and measure the magnetization, $M(t)$. For small magnetic fields, the relation between M and H is linear and can be most generally

represented by an integral

$$M(t) = \int_{-\infty}^{t} \chi(t - t')H(t')dt', \tag{6.1}$$

where χ is the sample susceptibility. If $H(t)$ takes the sinusoidal form above, this integral can be simplified by taking the Fourier transform of both sides, thereby transforming it into a frequency representation. Then:

$$M(\omega) = \chi(\omega)H_{ac}, \tag{6.2}$$

where $\chi(\omega) = \chi'(\omega) + i\chi''(\omega)$ is a complex number. The real part, $\chi'(\omega)$, is related to dispersion. The imaginary part, $\chi''(\omega)$, is directly related to the phase shift of the response with respect to the drive. When there is a phase shift, meaning $|\chi''(\omega)| > 0$, there is hysteresis in the $M - H$ plot, and the drive spends some time each cycle opposing the field of the system. This requires energy, and thus $\chi''(\omega)$ is also related to dissipation of energy into the system.

The form of the susceptibility can be derived for a simple spin model. We assume a spin obeys the following differential equation:

$$\frac{dm}{dt} = -\frac{m - m_0(B)}{\tau}, \tag{6.3}$$

where m is the spin magnetization, $m_0 = \chi_0 B$ is the zero frequency magnetization, and τ is the characteristic spin relaxation time. Changing to the frequency representation, dm/dt is replaced with $i\omega m$, which yields:

$$\frac{m}{B} = \chi(\omega) = \frac{\chi_0}{1 + i\omega\tau}. \tag{6.4}$$

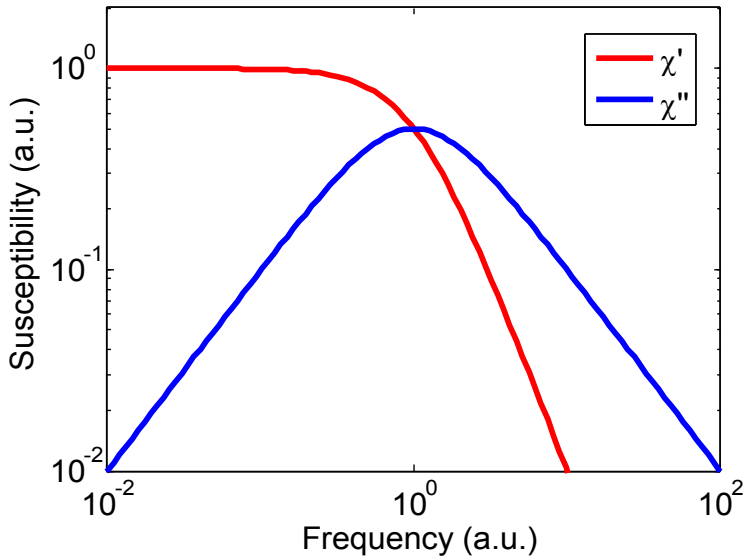

Figure 6.1: Real part (red) and imaginary part (blue) of the spin susceptibility

From this, the real and imaginary parts of the susceptibility are:

$$\chi'(\omega) = \frac{\chi_0}{1+\omega^2\tau^2} \tag{6.5a}$$

$$\chi''(\omega) = \frac{\chi_0\omega\tau}{1+\omega^2\tau^2}. \tag{6.5b}$$

At low frequency, $\omega \ll \tau$, the spin simply follows the field exactly, thus $\chi' = \chi_0$ and $\chi'' = 0$. At high frequencies, the field is moving too rapidly for the spin to respond at all, giving $\chi' = 0$ and $\chi'' = 0$. At frequencies compatible with the relaxation time, the spin will lag the field, causing the amplitude to be smaller than the maximum, $\chi' < \chi_0$, and there will be some dissipation, $\chi'' > 0$.

The susceptibility of an ensemble of spins will take the form:

$$\chi(\omega) = \int g(\tau)\frac{\chi_0(\tau)}{1+i\omega\tau}, \tag{6.6}$$

where $g(\tau)$ is the distribution of spin relaxation times.

6.2 Experimental setup

Magnetization is a flux in response to an excitation field. In circuit terms, the excitation is a current and magnetization is a flux in response to the current, or an inductance. By measuring the inductance of the SQUID loop, we gain information about the susceptibility of the spins. This experiment is based around a susceptometer SQUID. This is a SQUID design where it is possible to inject a current directly into the loop of the SQUID. The advantage of injecting the current directly into the loop is that the surface fields couple strongly to any surface spins, and the radial magnetization ensures optimal coupling of the spins to the SQUID. The complex inductance, $L = L' + iL''$, of the SQUID is measured by applying an excitation current at some frequency, f_0, and measuring the output of the flux locked loop with a phase sensitive lock-in amplifier. The lock-in amplifier provides the component in phase with the drive, which corresponds to the real part of the inductance, and the component 90° out of phase with the drive, which corresponds to the imaginary part of the inductance.

The inductance so measured contains several components. The total inductance is the sum of a geometric inductance from the excitation current coupling a flux directly to the SQUID, a component of flux coupled by the magnetization of the spins, and a component from the kinetic inductance of the superconductor. The flux induced by spin magnetization is a very small fraction, $\sim 10^{-5}$ of the flux coupled to the SQUID by the geometric inductance, and it is therefore necessary to cancel this inductance contribution by applying a counteracting flux with an external coil in a bridge configuration. The nulling coil is fed the same signal 180° out of phase and is tuned to cancel the contribution of the geometric inductance, allowing the measurement of the spin inductance. The kinetic inductance is

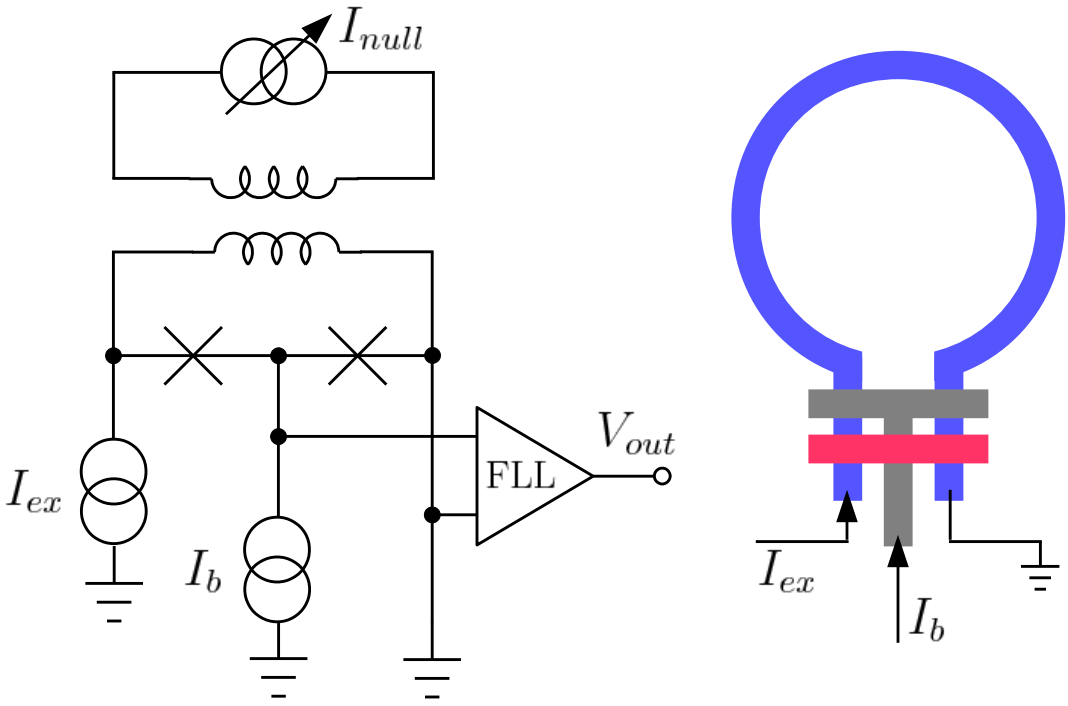

Figure 6.2: Experimental setup for measuring inductance noise. An excitation signal is injected directly into the SQUID loop while an opposite signal is coupled through an external coil, which cancels the geometric contribution to the flux. The output of the flux locked loop is fed to a lock-in amplifier.

strongly temperature dependent and drops off rapidly from its maximum at T_c [1]. For thin enough films such that the current distribution inside the film can be considered constant ($t \ll 2\lambda$) the kinetic inductance is roughly proportional to λ^2; which, in the BSC theory, takes the form:

$$\lambda^2(T) = \lambda^2(0)\left[1 - \left(\frac{T}{T_c}\right)^4\right], \tag{6.7}$$

where $\lambda(0)$ is the zero temperature penetration depth. This equation is most accurate near T_c in an idealized geometry. In the realistic case, there is no functional form that allows reliable subtraction of the kinetic inductance term; thus, it must be avoided. These SQUIDs are niobium, with $T_c \approx 9$ K, so the experiments must be done at ~ 2 K or lower, where the kinetic inductance contribution can be neglected. Note that because a SQUID is only

sensitive to changes in flux, these experiments are only sensitive to changes in inductance, ΔL.

6.3 Inductance *vs.* temperature

The temperature dependence of the SQUID inductance was measured by sweeping up and down in temperature as the change in the real and imaginary parts of the inductance was recorded. Excitation frequencies are very low, $f_0 \leq 300$ Hz, to ensure no phase shifts from the flux locked loop. A photon at this frequency has far too little energy to break apart a Cooper pair, so we expect very little quasiparticle loss. In the high temperature region, $T \geq 2K$, there is a strong decrease in L', which is interpreted as being due to the kinetic inductance. In this region, there is very little change in L'' consistent with low loss. At lower temperatures we observe rich structure in both L' and L''. Traces have jumps of order 1 fH in L', and they are accompanied by anti-correlated jumps in L'' at the same temperature. These jumps are qualitatively reproducible over several temperature cycles although they occur at significantly different temperatures. Careful inspection shows that even small fluctuations in L' and L'' are anti-correlated. This correlation would not occur due to flux noise alone; it represents a true fluctuation in the inductance of the device.

We have also probed the frequency dependence of the inductance by exciting with two simultaneous probe frequencies, $f_0 = 10$ Hz and $f_0 = 100$ Hz, and detecting the inductance with two independent lock-in amplifiers. We observe that the inductance fluctuations are highly correlated at the two frequencies. Also, $\Delta L'$ is independent of excitation frequency, whereas the dissipative part $\Delta L''$ scales linearly with frequency, $\Delta L'' \propto f_0$.

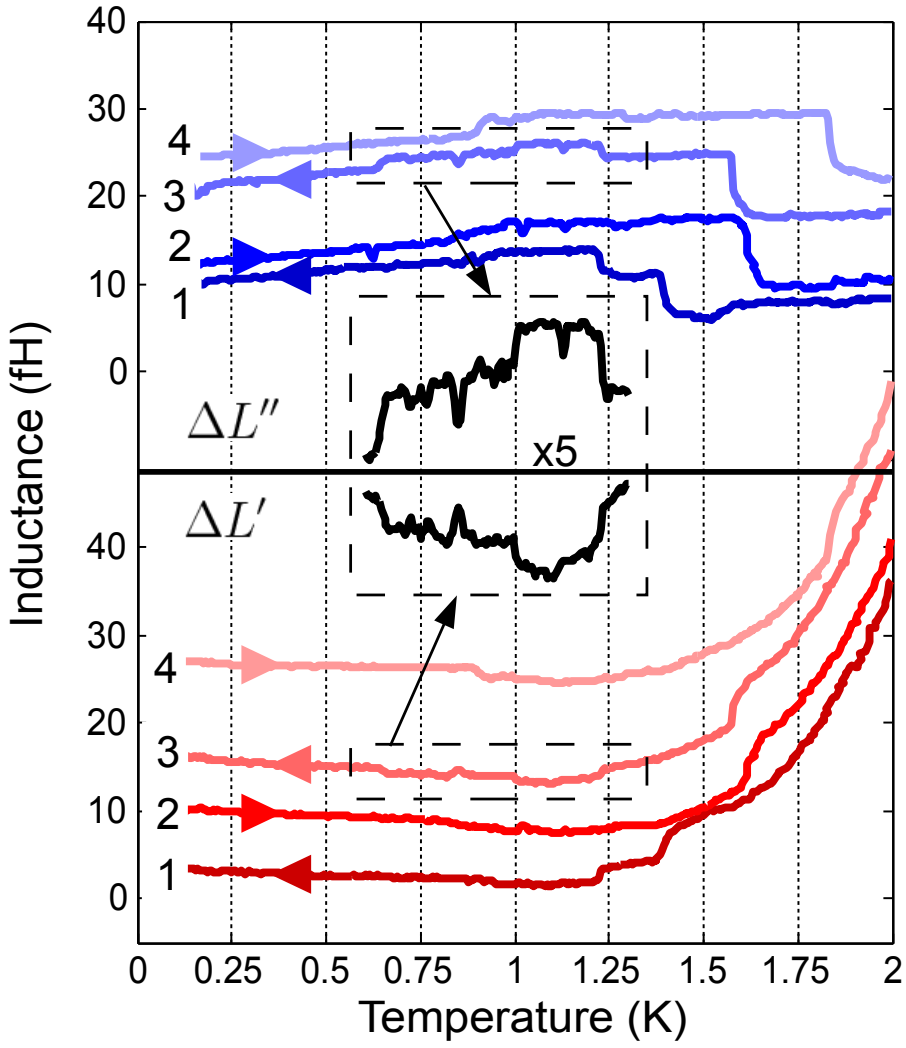

Figure 6.3: Inductance *vs.* temperature. The real and the imaginary part are recorded simultaneously as a function of temperature, and the four temperature sweeps are done back to back in the order indicated. The inset is multiplied by a factor of five to highlight the correlated fine structure.

6.4 Inductance noise

As an extension of the inductance temperature sweeps, we have also performed a set of experiments where the temperature is fixed and the inductance fluctuations are recorded as a function of time. In the absence of inductance fluctuations, measured noise is expected to be related to the flux noise at the excitation frequency and, therefore, have a white spectrum

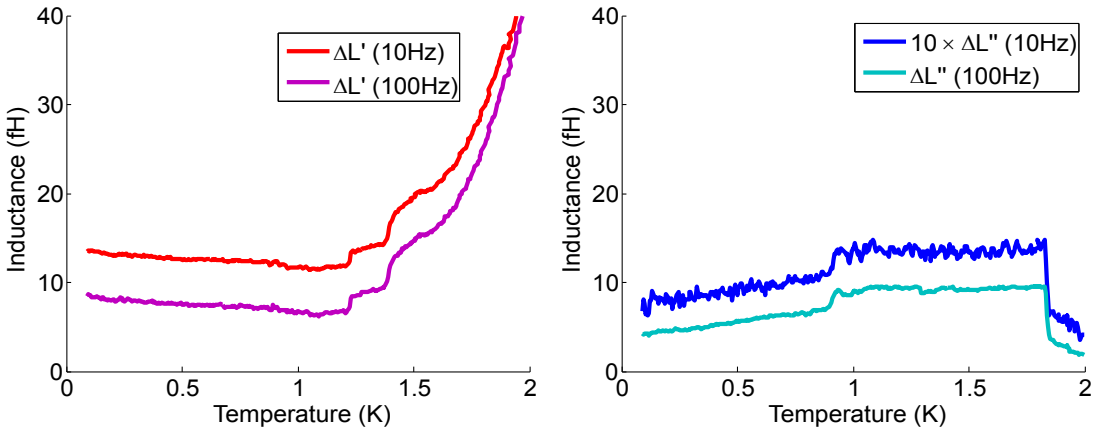

Figure 6.4: Frequency dependence of ΔL. 10 Hz and 100 Hz data are recorded simultaneously with a two-tone excitation feeding independent lock-in amplifiers. The real part (red) is independent of frequency, and the imaginary part (blue) scales linearly with frequency.

with $S_L = S_\Phi(f_0)/I_{ex}^2$. However, we observe inductance noise with a $1/f$ spectrum with a magnitude much greater than the white noise from the SQUID. The excess noise scales as I_{ex}^2 in the range from 10 Hz to 100 Hz and, therefore, is an apparent *inductance* noise.

Again, the inductance noise was measured simultaneously at two excitation frequencies in order to characterize the frequency dependence. At the frequencies $f_0 = 150$ Hz and $f_0 = 277$ Hz, we find a scaling that is similar to the inductance jumps in the temperature sweep data. $S_{L'}$ is independent of frequency in this range, and $S_{L''} \propto f_0^2$. It is also noted that in this frequency range, $S_{L''} > S_{L'}$. The fact that the noise has the same scaling as the inductance jumps suggests that discrete jumps in $L(T)$ and fluctuations in L at fixed frequency come from the same physical source.

6.4.1 Temperature dependence of inductance noise

Here (6.7) we have plotted the temperature dependence of the noise. The noise was measured over a range of temperatures from 2 K to 100 mK. The data indicates that the inductance noise increases as the temperature is reduced until it eventually saturates. The

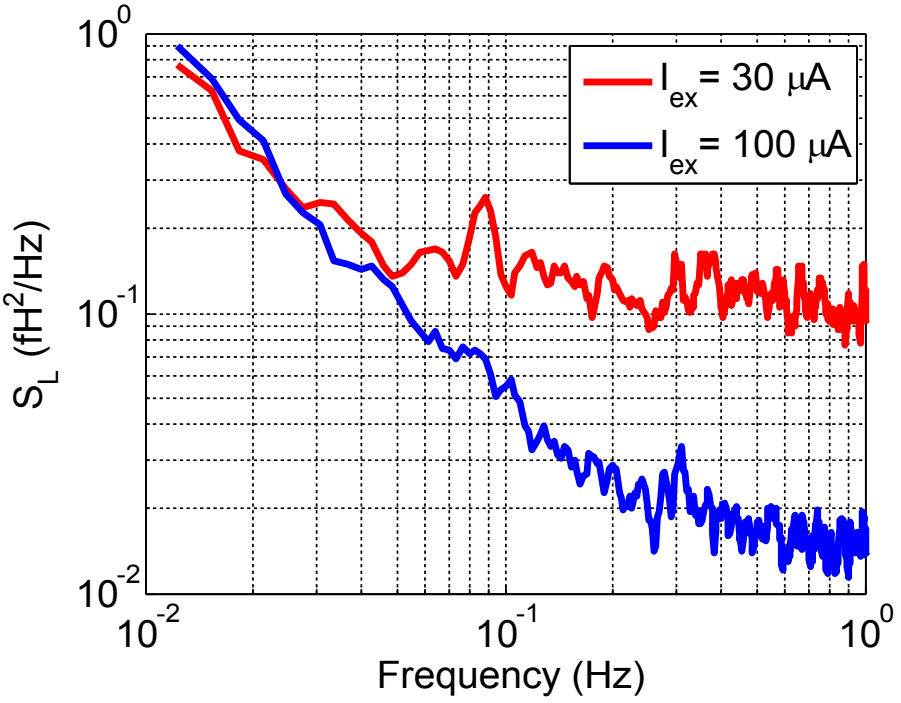

Figure 6.5: Inductance noise excitation current dependence. Excess low frequency noise scales as I_{ex}^2, which indicates that the noise is inductance like.

saturation occurs at roughly 200 mK.

6.5 Interpretation

The first possible explanation of the inductance noise comes from critical current noise. Experiments indicate that critical current noise has a $1/f$ spectrum and is proportional to the square of the junction critical current [2]. Insofar as the SQUID can be thought of as a junction with a flux dependent critical current, it might be reasonable to think that the noise could give an apparent inductance noise. Numerical simulations we have performed according to the method [3], however, indicate that critical current noise will not result in an inductance noise.

Quasiparticles should also be considered as a possible source of the inductance noise

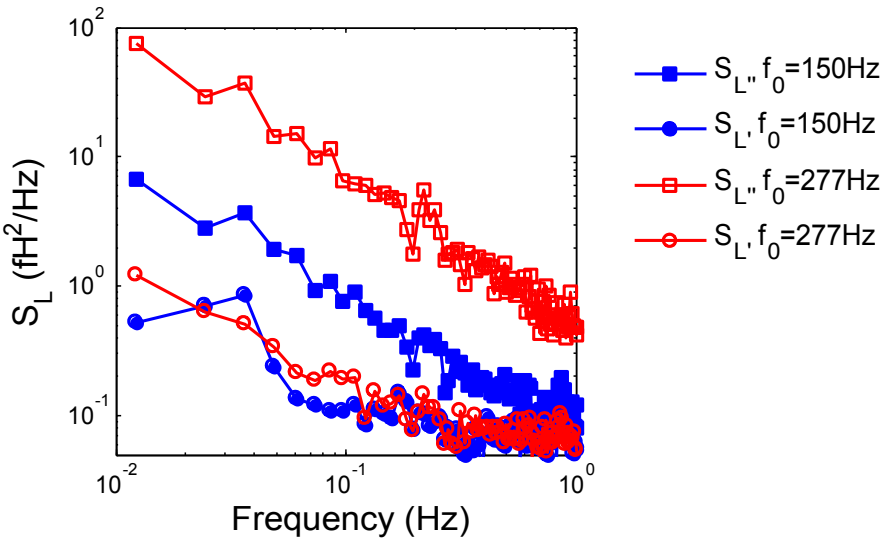

Figure 6.6: Frequency dependence of inductance noise. Fluctuations in L as fixed temperature show the same frequency dependence as the temperature sweeps. The real part of S_L (circles) is independent of frequency, and the imaginary part (squares) is linearly dependent on frequency.

because if quasiparticles are present, one would expect a similar frequency signature. Quasiparticles would generate a frequency independent kinetic inductance contribution to the real part of the inductance, and a linear in frequency imaginary part of the inductance. At these low temperatures and low excitation frequencies, however, we expect negligible contributions from quasiparticles.

6.5.1 Correlated fluctuations

The data is most compatible with fluctuations in the susceptibility of the surface spin system. Recent theoretical work using Monte Carlo simulations of Ising spin glass systems in 2D and 3D have demonstrated that the susceptibility and magnetization noise of systems of spins has the same frequency and temperature dependence as the measurements of flux and inductance noise on SQUIDs [4]. The evidence from the frequency dependence and relative

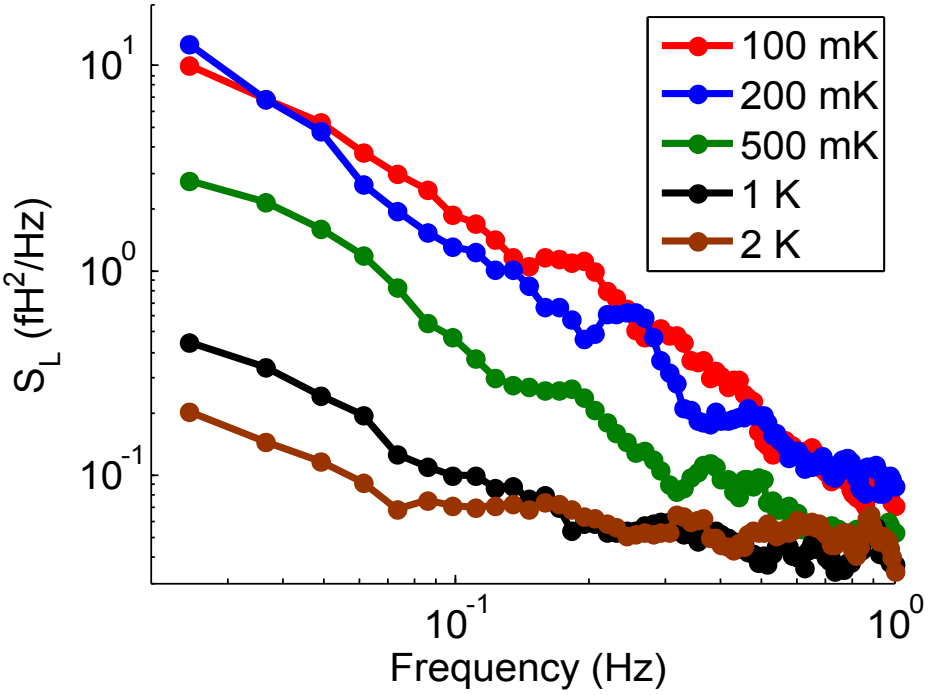

Figure 6.7: Temperature dependence of inductance noise. The noise increases as temperature is decreased and saturates around 200 mK.

magnitude of L' and L'' allow us to make some remarks about the fluctuators. Recall the expression for the susceptibility for a single spin from Equation 6.4. If a change in the inductance results from a change in susceptibility, then

$$\Delta L' = \frac{\Delta\chi_0}{1+\omega^2\tau^2} \tag{6.8}$$

$$\Delta L'' = \frac{\Delta\chi_0\omega\tau}{1+\omega^2\tau^2}. \tag{6.9}$$

The observation that $\Delta L'$ is independent of frequency for all frequencies considered, and that $\Delta L''$ scales linearly with frequency, indicates that the drive frequency is low compared to characteristic times $\omega\tau \ll 1$. However, the same limit also implies that $\Delta L'' \ll \Delta L'$, which is not consistent with observations. If we allow fluctuations also in τ then the equation for

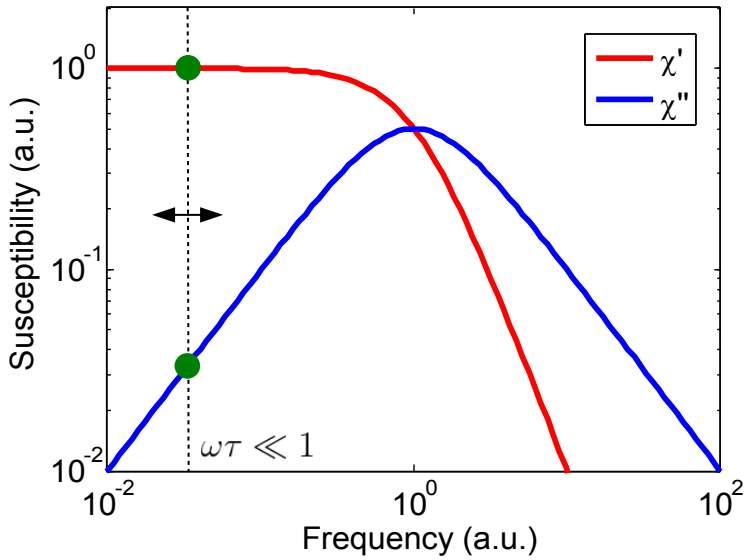

Figure 6.8: The vertical line represents the operating frequency. In the limit $\omega\tau \ll 1$ the real part of the susceptibility is independent of frequency, whereas the imaginary part depends linearly on frequency.

$\Delta L''$ is, by the chain rule,

$$\Delta L'' = \frac{\Delta\chi_0\omega\tau + \chi_0\omega\Delta\tau}{1+\omega^2\tau^2}. \tag{6.10}$$

In this situation $\Delta L''$ can be larger than $\Delta L'$, consistent with observations, if there are fluctuations of τ that are correlated with the fluctuations of χ_0.

This correlation is consistent with a simple picture of spin clustering where the formation of a larger cluster increases the susceptibility, but increases the characteristic time as well [5].

6.5.2 Spin Clusters

Further evidence for clustering behavior is present in the temperatures sweeps of the inductance. To estimate the size of the inductance contribution from independent spins, we consider a Curie-like model. The Curie susceptibility for N independent spins takes the

following form:

$$\chi_{Curie} = \frac{\mu_0^2 \mu^2}{k_B T} N. \tag{6.11}$$

Considering a simplified SQUID geometry with loop radius R and wire radius r populated by a density σ of spins, we infer a spin contribution to the real part of the inductance of:

$$L'_{spin} = \frac{\mu_0^2 \mu^2}{k_B T} \sigma \frac{R}{r}. \tag{6.12}$$

Plugging in the parameters $R/r = 20$, $\mu = \mu_B$, and $\sigma = 5 \times 10^{17} \mathrm{m}^{-2}$ yields a spin contribution of ~ 30 aH at a temperature of 1 K. In the temperature sweep experiments, discrete jumps were observed with magnitude $\Delta L' \approx 1$ fH, which is significantly larger than the total spin contribution predicted from the simple model. We interpret the magnitude of the inductance jumps as further evidence for the formation of clusters of spins with some ferromagnetic ordering, and the cluster size can be estimated from the data.

The formation of a ferromagnetic cluster of α spins results in N/α effective spins with effective moment $\mu = \alpha \mu_B$. Because the inductance contribution (Equation 6.12) is quadratic in moment, but only linear in number of spins, the formation of a cluster will increase the inductance contribution by a factor of α. To explain the magnitude of the jumps, therefore, requires α in the range of 10 to 100.

Cluster formation is often associated with a spin glass as the freezing temperature is approached. Although we do not always see telltale signs of a spin glass, such as a cusp in the susceptibility, this clustering is evidence to suggest that a spin glass is forming. For more information of spin glasses, see Section 5.5.3 of this thesis.

6.6 Connection to flux noise

It is natural to ask whether the observed inductance fluctuations are in fact the origin of the excess low frequency flux noise. During normal SQUID operation, there are currents of the order of the SQUID critical current flowing through the SQUID loop. Clearly, if the inductance of the SQUID was fluctuating, that would generate an apparent flux noise. For a SQUID biased at $\Phi_0/4$, the estimated flux noise, S_Φ, due to inductance fluctuations, S_L, is

$$\frac{S_\Phi}{\Phi^2} = \left(\frac{\beta_L^2}{16}\right)\left(\frac{S_L}{L^2}\right), \tag{6.13}$$

where $\beta_L = 2LI_0/\Phi_0$. For $\beta_L = 1$ and $S_L/L^2 = -120$ dB/Hz at 1 Hz, corresponding to a flux noise that is 100 times smaller than what is observed. This indicates that flux noise is not due to inductance noise alone.

6.6.1 Correlation measurements

To determine whether there is any kind of connection between the $1/f$ inductance noise and the $1/f$ flux noise, we have also performed a series of correlation measurements between the two. In these experiments, the imaginary part of the inductance, $L''(t; f_0 = 100\text{Hz})$, was recorded simultaneously with the flux, $\Phi(t)$. From the two time series, we compute the normalized cross spectral density

$$P_{L''\Phi} = \frac{S_{L''\Phi}}{(S_{L''}S_\Phi)^{1/2}}. \tag{6.14}$$

The result plotted in figure 6.9 shows that the flux and the inductance fluctuation are highly correlated at low temperatures, and the correlation decreases as the temperature is increased. This correlation indicates a common origin of the two phenomena; however, simple arguments complicate the picture.

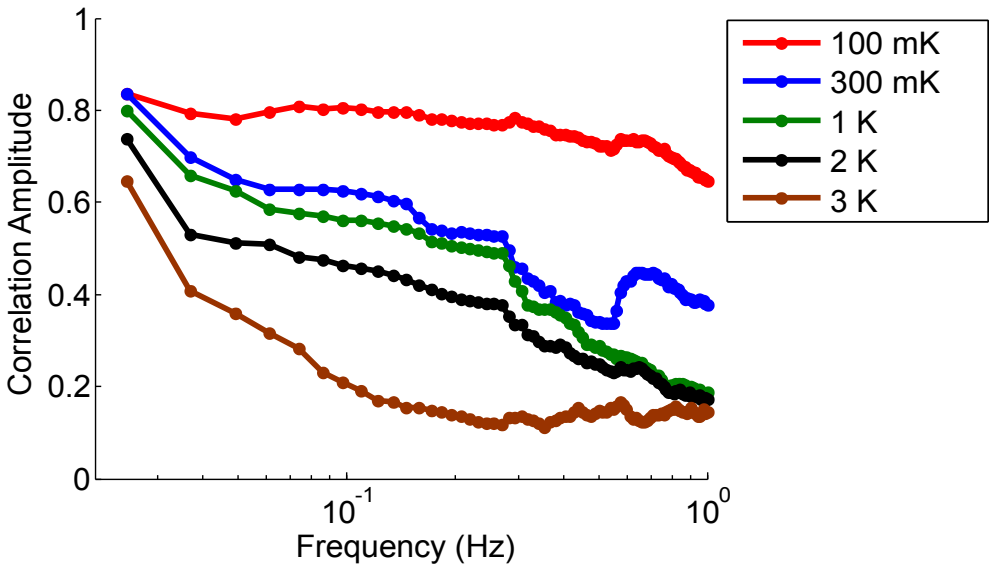

Figure 6.9: Inductance and flux cross spectrum. There is significant correlation measured at the lowest temperature and the correlation drops off as the temperature is increased.

Because flux is odd under time reversal and inductance is even, $S_{L\Phi}$ should go to 0 in the limit of a large number of fluctuators. This has been confirmed by Monte Carlo simulations of Ising spin glass systems [4]. This could indicate that there are a relatively small number of active fluctuators contributing to the noise, or possibly more complicated physics. This observation of correlation is the most strict limit on possible theoretical models for $1/f$ noise.

6.6.2 $1/f$ noise from fractal spin clusters

A very recent theoretical model by Kechedzhi, Faoro, and Ioffe [6] attempts to explain the inductance and flux correlation with electron spins and represents the current state of the art theory for $1/f$ noise in superconducting circuits.

A key feature of the model is the existence of a large fractal cluster of strongly coupled spins. The fractal cluster spans the entire sample but only contains a small fraction of the total number of spins. The rest of the spins form smaller, more localized, fractal clusters or isolated spins, all of which are free to fluctuate freely.

The fractional dimension of clusters results in a logarithmic scaling of the cluster flipping energy barrier on the cluster size. This distribution in turn leads to a power law flux noise spectrum, $S_\Phi \propto 1/f^\alpha$.

In addition, the response of the clusters to a sinusoidal excitation is dominated by active clusters with characteristic rates of the same order as the excitation frequency. These clusters in turn live in a local quasistatic field created by neighboring clusters that flip more rarely. When one of these clusters does flip, it changes the local field at the active clusters, which leads to a change in the response to the excitation. This causes susceptibility (inductance) and magnetization (flux) noise to be correlated. The results of numerical simulations show that the correlation increases as temperature is lowered and eventually saturates, consistent with the observations.

Bibliography

[1] R. Meservey and P. Tedrow, Journal of Applied Physics **40**, 2028 (1969).

[2] F. Wellstood, C. Urbina, and J. Clarke, Appl. Phys. Lett. **85**, 5296 (2004).

[3] C. Tesche and J. Clarke, Journal of Low Temperature Physics **29**, 301 (1977).

[4] Z. Chen and C. C. Yu, Phys. Rev. Lett. **104**, 247204 (2010).

[5] D. Huser, A. Van Duyneveldt, G. Nieuwenhuys, and J. Mydosh, Journal of Physics C: Solid State Physics **19**, 3697 (2000).

[6] K. Kechedzhi, L. Faoro, and L. Ioffe, arXiv preprint arXiv:1102.3445 (2011).

Chapter 7

Effect of dielectric encapsulation

Previous studies of $1/f$ flux noise in SQUIDs failed to reveal a clear dependence of noise on materials used to fabricate the devices. The first experiments by Wellstood measured SQUIDS made from niobium, lead, and lead indium with very little variation in noise [1]. These SQUIDs were fabricated on an oxidized silicon substrate and utilized a silicon oxide wiring dielectric and, on some devices, a silicon oxide passivation layer. These materials were not changed in those experiments. Later, qubits made of aluminum were observed to show compatible levels of flux noise [2, 3]. Qubits are typically fabricated on a silicon or sapphire (Al_2O_3) substrate, and they are left with no explicit dielectric encapsulation on the upper surface, which, for practical purposes, means that the native metal oxide is present there.

The common thread among all of these devices is the presence of oxygen in the encapsulating dielectric layers. To test the effect of oxygen on the $1/f$ flux noise level, we have fabricated and measured a series of aluminum SQUIDs with varying levels of encapsulation by silicon nitride (SiNx). SiNx has a couple of advantages in this application. First, it does not directly contain oxygen; moreover, SiNx is known to be a very good diffusion barrier against oxygen [4] so it should be able to provide a stable, oxygen-free interface.

We have found that the flux noise power from a nitride encapsulated SQUID is reduced

by more than an order of magnitude relative to an otherwise identical oxide encapsulated device. This data is the first clear example of a reduction of flux noise in a superconducting device. The reduction comes as a result of a specific material change and should pave the way for a deeper understanding of the origin of $1/f$ flux noise, as well as improved SQUID and qubit performance.

7.1 SQUID fabrication

The superconducting thin film that forms the SQUID loop in our process has both a top and a bottom dielectric encapsulation, with the side encapsulation making up a negligible area. As part of the fabrication process, first a layer of aluminum referred to as the base layer, is deposited, followed by a dielectric layer in which vias are etched for the junctions, followed by another layer of aluminum, referred to as the counter electrode (more details in A). In this way, the substrate composes the bottom encapsulation of the base layer, and the dielectric layer for the vias composes the top encapsulation of the base layer. Note that the counter electrode is encapsulated below by the dielectric layer and above by nothing. This means that not all metal is encapsulated by this process. However, the device is highly asymmetric with a large majority of the metal for the SQUID loop in the base layer. The unencapsulated areal fraction depends on the device geometry but is always $< 10\%$.

Four wafers were fabricated for this study. They have the following different dielectric encapsulations:

1. Thermal SiOx bottom and PECVD SiOx top
2. Thermal SiOx bottom and PECVD SiNx top
3. PECVD SiNx bottom and PECVD SiOx top
4. PECVD SiNx bottom and PECVD SiNx top

The thermal SiOx is 1500 Å thick. In the case of SiNx bottom layers, the commercial thermal SiOx is first removed with an HF dip immediately before the nitride deposition. Further details of the fabrication process can be found in Appendix A of this thesis.

Other than the encapsulation material, all of the devices are fabricated to be nominally identical in terms of critical current, normal state resistance, and SQUID loop inductance. The values in the following table represent estimates of these parameters for the four devices presented later.

Table 7.1: Measured device parameters

	Dielectric material:				
	Lower	Upper	$I_c(\mu A)$	$R_N(\Omega)$	L(pH)
Device 1:	SiOx	SiOx	3.5	15.2	39
Device 3:	SiNx	SiOx	3.7	23.0	47
Device 2:	SiOx	SiNx	4.7	17.4	42
Device 4:	SiNx	SiNx	4.0	15.0	41

7.2 Noise measurements

Noise in these devices was measured using a correlation amplifier setup as described in Section 3.7. This setup allows us to measure $1/f$ noise accurately over several orders of magnitude in frequency with a noise floor less than 0.1 $\mu\Phi_0/\sqrt{\text{Hz}}$. All data is taken at a temperature of 200 mK at the optimally sensitive bias point where the flux in the first stage is amplified by the second stage SQUID with gains in the range of 30-100.

The data shows a clear progression toward lower noise as more of the devices is encapsulated in the nitride based dielectric. The data can be fit to the functional form $S_\Phi = A/f^\alpha + B$ in order to extract the values for the magnitude of the noise A, the low frequency slope α, and the white noise level B. The results of that fitting appear in the following table. The noise power is characterized by the fitting parameter A. From the oxide encapsulation to

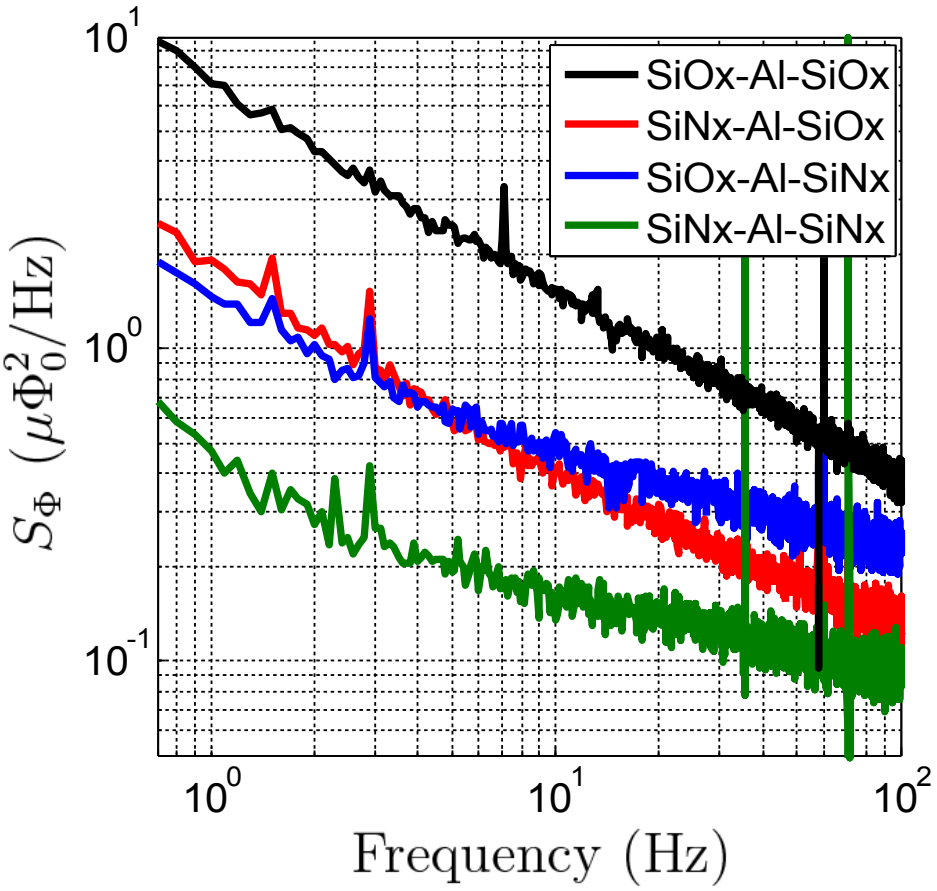

Figure 7.1: Comparison of SQUID flux noise power for nitride and oxide encapsulated devices. These devices are all nominally identical outside the dielectric encapsulation and have an aspect ratio of 25.

the nitride encapsulation there is more than an order of magnitude reduction in noise power. This reduction is compatible with the assumption that the nitride encapsulated areas are nearly noiseless, with the remaining noise coming from the $\sim 10\%$ of the SQUID loop that is unencapsulated. In addition, two separate dies were measured from each wafer to further verify the effect (see Figure 7.2). The reduction in noise appears to be robust across multiple dies on one wafer.

Note that the reduction in noise from encapsulating a single side of a device is larger than expected from a simple non-interacting spin model. In such a model, the spins on the top and

Table 7.2: Fit Parameters

Dielectric material:				
Lower	Upper	$\left[\frac{A}{(1\text{Hz})^{\alpha}}\right]^{1/2}(\mu\Phi_0/\sqrt{\text{Hz}})$	α	$B^{1/2}(\mu\Phi_0/\sqrt{\text{Hz}})$
SiOx	SiOx	2.6	0.59	0.50
SiNx	SiOx	1.4	0.73	0.26
SiOx	SiNx	1.1	0.62	0.41
SiNx	SiNx	0.57	0.42	0.24

bottom should contribute roughly equally to the noise power; therefore, the expectation for encapsulating a single side would be that half of the spins would be eliminated, resulting in a factor of two decrease in noise power. The measurement, however, indicates a factor of four reduction. The extra factor of two decrease could be explained if there is also a factor of two reduction in cluster size. In this case $\mu \to \mu/2$, and $\sigma \to 2\sigma$, and $S_\Phi \propto \sigma\mu^2 \to S_\Phi/2$. If the cluster size is decreasing when spins are removed from one surface only, this implies that there is strong correlation between spins at the upper and lower surfaces of the superconductor. This correlation is especially plausible for clusters at the edge of the wire. All of the current flows within a penetration depth λ of the edge. Here, the current is the strongest, providing a large coupling of these clusters to the SQUID.

The white noise level for these devices is set by the Johnson noise in the resistors shunting the junctions. Because these devices are all fabricated nominally identically and the normal state resistances, R_N, are all very similar, it is not expected that the white level would vary much, and indeed this is the case. There is no clear pattern in white noise level.

The value for the $1/f$ slope, α, ranges from $0.42 - 0.73$. However, there does not seem to be a systematic pattern here either. The highest slopes occur for the half nitride devices, both of the full encapsulated devices have a lower slope. Most likely this is due to statistical variations in the devices.

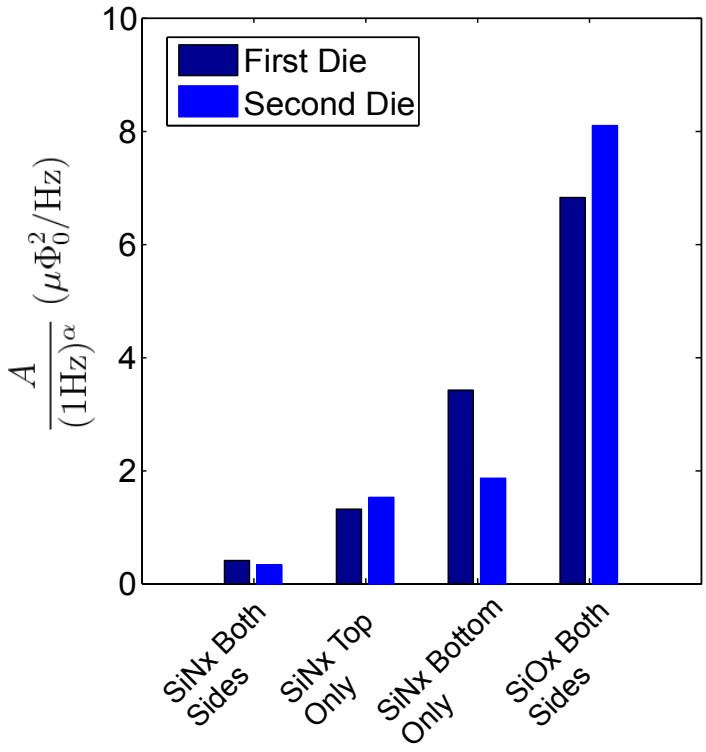

Figure 7.2: For each level of encapsulation, the measurement was repeated on two dies. Dark bars indicate the first die, and light bars indicate the second.

7.3 Aspect ratio dependence

We have also investigated the aspect ratio dependence of the noise. The aspect ratio in this case is the ratio R/r, where R is the radius of the SQUID loop and r is the radius of the wire. The SQUID mask (see Figure 7.3) has patterns for aspect ratios of 0.25, 10, and 25. Models of noise from surface spins (see Section 5.4) predict that the noise should scale with aspect ratio. This scaling has been observed for the oxide encapsulated devices; however, nitride encapsulated devices show much weaker scaling.

This is further evidence that the noise in the case of the nitride encapsulation is due to the unencapsulated part of the SQUID loop, because that area does not scale with aspect ratio.

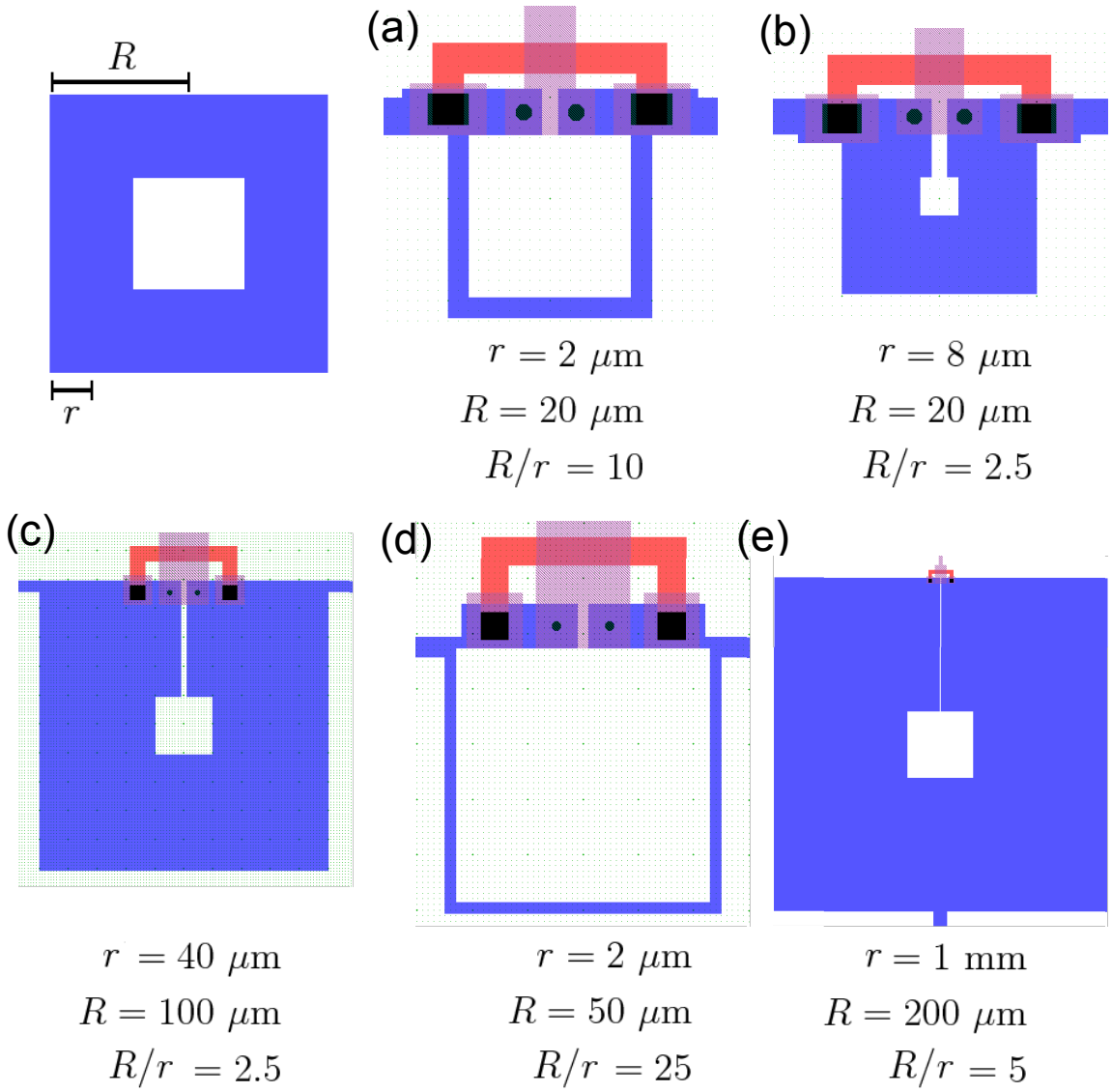

Figure 7.3: Mask patterns. (a)-(d) have the ability to inject current directly through one branch of the SQUID loop.

7.4 Interpretation

These results allow us to refine ideas about the origin of spins, which give rise to $1/f$ noise in SQUIDs and qubits. To date, there have been a few ideas proposed to explain the origin of the spins.

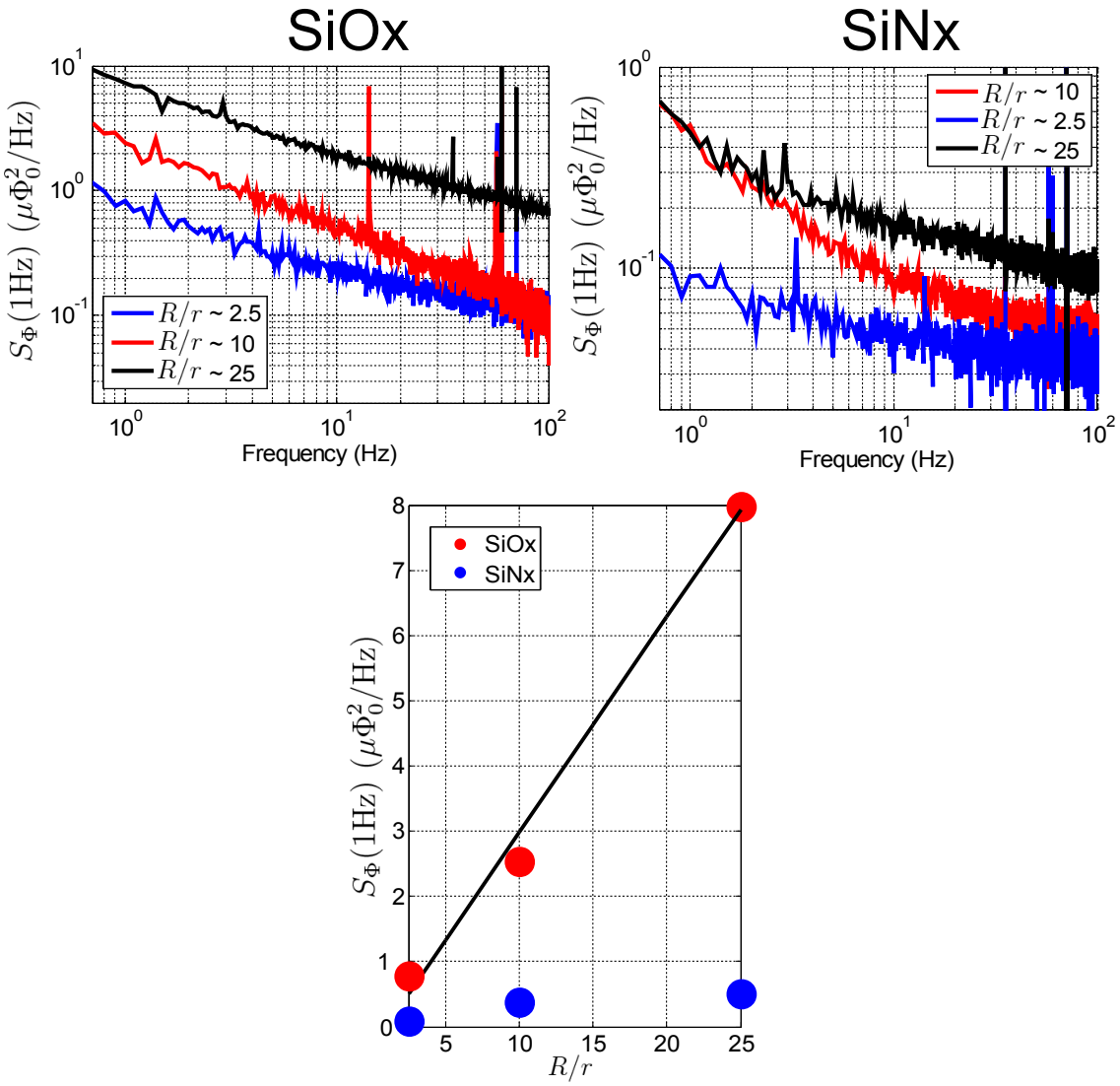

Figure 7.4: Aspect ratio scaling of SQUID flux noise. Top panels show full flux noise power spectra superimposed over each other for three aspect ratios. The lower panel is the noise power for each aspect ratio at 1 Hz. The black line is a linear fit to the oxide encapsulated data.

7.4.1 Chemisorbed Oxygen

A different explanation revolves around chemsorbed oxygen O_2^- at the interface between the metal and the encapsulation. Noise properties of chemisorbed oxygen in thin AlOx Josephson junction tunnel barriers have been measured by Buhrman *et al.* [5], and the

noise has been shown to decrease when oxygen is driven away by electron bombardment. Preliminary calculations by Ruquan Wu at UC Irvine have suggested that such an oxygen molecule on a surface will exhibit a paramagnetic spin that is oriented perpendicular to the plane of the surface. This spin can fluctuate and give rise to $1/f$ noise. Furthermore, calculations indicate that the energy barrier to reorientation of this spin is significantly higher on a silicon nitride surface than it is on a silicon oxide surface.

This barrier height to reorientation could be the explanation of the reduced flux noise result; however, one would expect little chemisorbed oxygen on the bottom surface of the SQUID due to an ion mill clean followed by an in-situ sputtering of aluminum. In this case, the bottom nitride would have no effect. The fact that there is significant reduction from changing only the bottom encapsulation to nitride casts doubt on this interpretation.

7.4.2 Oxygen vacancies

Another explanation is the creation of oxygen vacancies in the oxide encapsulation or in the native oxide of the metal at the metal-insulator interface. Recent experiments on HfO_2 thin film [6] and ZnO nanoparticles [7] have demonstrated room temperature ferromagnetism where the bulk samples of the materials are nonmagnetic. The appearance of these spins has been attributed to a surface effect where an oxygen atom or ion is missing from the crystal lattice and the resulting space is occupied by free electrons. In the crystal potential, two unpaired electrons are energetically favored to exist in the triplet state, where they would exhibit a magnetic moment. The precise details are very different for covalent bonds as opposed to ionic bonds [8], but the end result is similar.

It turns out that essentially all superconducting devices made to date have used an oxygen based encapsulation in some form or another. Sapphire, a common substrate, is Al_2O_3. Silicon substrates are typically thermally oxidized. SiO_2 is a very common wiring

dielectric, and even when a device is left unencapsulated, the native oxide of the metal contains oxygen. The presence of oxygen satisfies the universal nature of the noise that has been reported, and oxygen vacancies are a convenient source of unpaired magnetic moments. A reduction in noise when the device is encapsulated with silicon nitride is consistent with this model.

Further experiments to attempt to directly identify oxygen vacancies are ongoing. One experiment involves creating a hybrid dielectric on the upper interface of a SQUID. The dielectric would be a layer of SiNx capped by a layer of SiOx. By varying the thickness of the SiNx layer, keeping the total thickness constant, it will be possible to determine if the paramagnetic spins reside at the interface between the metal and the insulator, or on the surface. X-ray Magnetic Circular Dichroism (XMCD) can also be used to gain information about surface spins. XMCD is an element specific probe of surface magnetism that works by comparing X-ray absorption spectra taken with left and right circularly polarized light. This measurement could yield information such as the magnetic moment of magnetic defects, which should clarify the picture of the origin of spins that give rise to $1/f$ flux noise in superconducting circuits.

7.5 Implications for scalable superconducting qubits

It is expected that a reduction in flux noise will result in increased dephasing times in qubits. The qubit decoherence time T_2^* is proportional to the flux noise amplitude

$$T_2^* = S_\Phi^{-1/2} \left(\frac{df_{10}}{d\Phi} \right)^{-1}. \tag{7.1}$$

With this relation, the observed noise reduction of a factor of 20 in power with a nitride encapsulation, which corresponds to a factor of 4.5 in amplitude, should correspond to at

least a factor of 4.5 increase in qubit coherence time. It is also noted that a superconducting phase qubit typically has a very large aspect ratio. If the aspect ratio scaling persists, then the increase in T_2^* could be significantly larger than predicted from these SQUIDs.

To calculate the minimum coherence time needed to have a robust large scale quantum computer, the relevant scale is the error correction threshold. That threshold for recently developed surface codes is an error rate of $\sim 10^{-2}$ [9]. With $1/f$ noise causing dephasing, the error rate is roughly $(t/T_\Phi)^2$, where t is the operation time, and T_Φ is the pure dephasing time [10]. Taking the reasonable estimate of t=200 ns, this implies a minimum coherence time of 2 μs. Current phase qubits can achieve $\sim$ 500 ns, which is not sufficient. However, a successful nitride encapsulated qubit of the same design would be expected to have a coherence time in excess of 1.5 μs. We expect gate fidelities for such a device to be very near the fault-tolerant threshold.

Bibliography

[1] F. Wellstood, C. Urbina, and J. Clarke, Appl. Phys. Lett. **50**, 772 (1987).

[2] R. Bialczak, R. McDermott, M. Ansmann, M. Hofheinz, N. Katz, E. Lucero, M. Neeley, A. O'Connell, H. Wang, A. Cleland, and J. Martinis, Phys. Rev. Lett. **99**, 187006 (2007).

[3] F. Yoshihara, K. Harrabi, A. Niskanen, Y. Nakamura, and J. Tsai, Phys. Rev. Lett. **97**, 167001 (2006).

[4] V. Doo, Electron Devices, IEEE Transactions on **13**, 561 (1966).

[5] E. Tan, P. Mather, A. Perrella, J. Read, and R. Buhrman, Phys. Rev. B **71**, 161401 (2005).

[6] A. Sundaresan, R. Bhargavi, N. Rangarajan, U. Siddesh, and C. Rao, Phys. Rev. B **74**, 161306 (2006).

[7] H. Hsu, J. Huang, Y. Huang, Y. Liao, M. Lin, C. Lee, J. Lee, S. Chen, L. Lai, and C. Liu, Appl. Phys. Lett. **88**, 242507 (2006).

[8] G. Pacchioni, ChemPhysChem **4**, 1041 (2003).

[9] A. G. Fowler, M. Mariantoni, J. Martinis, and A. N. Cleland, Phys. Rev. A **86**, 032324 (2012).

[10] J. Martinis, S. Nam, J. Aumentado, K. M. Lang, and C. Urbina, Phys. Rev. B **67**, 094510 (2003).

Appendix A

SQUID fabrication

This section describes the SQUID fabrication process at the University of Wisconsin - Madison.

A.1 Device Patterns

Our SQUIDs are all patterned photolithographically and our standard mask has six patterns on it, along with test structures for room temperature probing of the junction normal state resistance and the junction shunt resistors. Four of the SQUID patterns are various sizes of SQUIDs with the ability to inject a current directly into the loop to provide an external flux to the device. Two are large area, wide linewidth, washer SQUIDs of a conventional Ketchen-Jaycox design [1]. All of the junctions are 2 μm^2. The mask was drawn in LEdit and the patterns are reproduced in Figure 7.3.

A.2 SQUID parameter targets

The primary consideration when fabricating these SQUIDs is avoiding hysteresis in the IV curve. To do this (see Section 3.1) we must have $\beta_c < 1$. In our fabrication process, we have control over the junction critical current I_c, and the shunt resistance R.

The shunt capacitance is dominated by the geometrical capacitance of the junction itself. This capacitance generally scales as A/d, where A is the area of the parallel plates, and d is the separation. The capacitance of the junctions is estimated to be $\sim$50 fF/μm^2.

The critical current of the junctions can be controlled by controlling the oxidation exposure, E, of the Al film forming the tunnel barrier, where the exposure is the product of the partial pressure of oxygen and the time. Experimentally, it is accepted that the critical current as a function of exposure scales as [2]:

$$J_c \propto 1/\sqrt{E} \tag{A.1}$$

The junction oxidation is the most variable part of the SQUID fabrication process. Simplifying the whole process is the fact that the junctions are fabricated before the resistors, and the junction critical current can be estimated by room temperature measurements. This allows the resistors to compensate for any wafer-to-wafer variability in J_c. The fact that the junction critical current can be calculated from its normal state resistance R_N is contained in the Ambegaokar-Baratoff relation [3]:

$$I_c = \frac{\pi\Delta}{2R_N}, \tag{A.2}$$

where Δ is the superconductor gap energy in units of electron volts. For aluminum, $\Delta \sim$ 190 μeV; thus the formula predicts 10 μA for a resistance of 30 Ω.

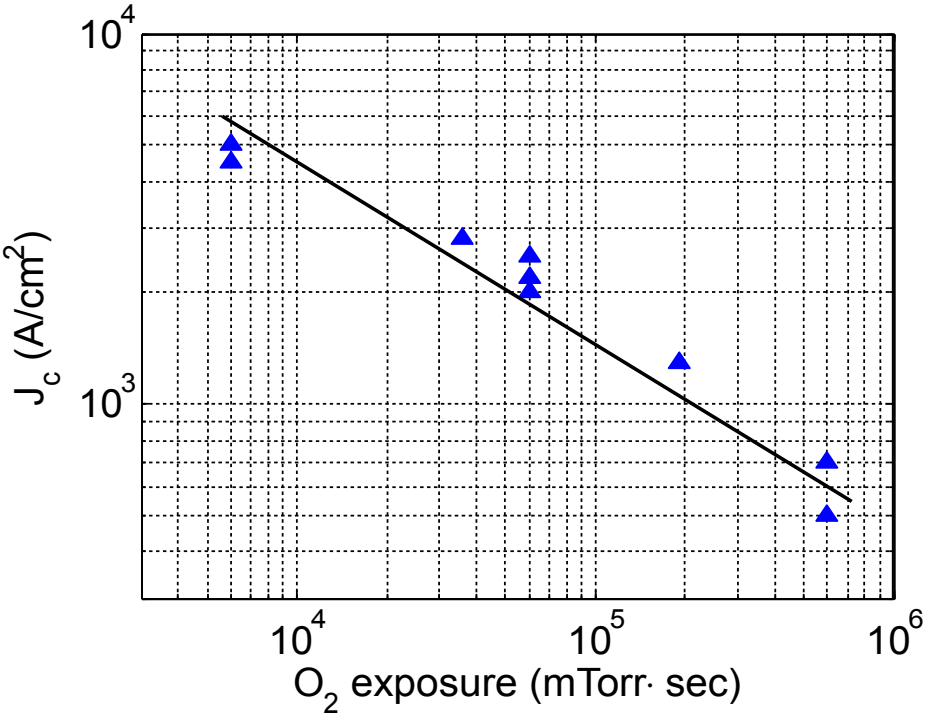

Figure A.1: Experimental results for a Nb-Al-AlOx-Nb junction process. The line is a fit to the square root functional form. Data courtesy of Shaojiang Zhu.

The mask contains test patterns for measuring the junction normal state resistance, and therefore estimating the junction critical current. Once this is known, a shunt resistance is chosen such that $\beta_c < 1$, typically $\beta_c = 0.5$.

A.3 Fabrication subroutines

The fabrication process includes a very large number of steps, many of them repeated several times during the entire run. This section defines some groups of steps that occur together and will be building blocks for the composite process.

A.3.1 Ion mill

An ion mill is a common step in the fabrication process. It is used to clean the surface of the wafer before deposition, or to remove a native oxide, leaving a fresh surface to be re-oxidized in a controlled way, or to clean a metal layer prior to the deposition of another to ensure good metal-to-metal contact.

During the ion mill, material is removed from the wafer by a physical etch process. Ions of gas, in our case argon, are generated in a plasma and accelerated toward the target, where they remove material on impact. The ion mill is performed at a low pressure of non-reactive argon, typically around 1×10^{-4} Torr, and the rest of the process steps are performed *in situ* after the clean without venting the chamber to the atmosphere. Ion milling is especially important when the intent is to avoid oxygen at the interfaces. Ion milling will remove surface atoms, including oxygen, leaving a clean surface for further processing.

Surface cleans and junction oxidations are done in our sputter system. The wafer is mounted on an aluminum platen and clamped in place with an aluminum ring around the wafer circumference. For a surface clean, we typically mill at a bias voltage of 800 V and a beam current of 20 mA, giving a mill rate of $\sim$1 nm/sec for 30 seconds. Prior to a junction oxidation, the mill time is increased to 45 seconds to ensure a good quality junction. During the mill process the wafer is rotated to provide a more even mill profile.

We also mill the metal just prior to depositing resistors to facilitate good metal-to-metal contact. This is done in our metal evaporator, but with similar 800 V bias and 30 mA beam current. In this case, the mill time is 18 seconds. This system does not have the capability of rotation.

In all cases, after the mill, the argon is pumped out rapidly and the next process begun as soon as possible. Even at pressures of 1×10^{-8} Torr there is enough oxygen to reform oxides in a matter of minutes.

A.3.2 Sputter deposition

The workhorse superconductor deposition system is the sputter system. Sputtering involves bombarding a metal target with energetic ions that eject atoms from the target; the atoms then deposit on the wafer and adhere, forming a thin film. Our sputter system is dedicated to aluminum and niobium sputtering with a built-in ion mill capability. The base pressure is 1×10^{-8} Torr, and sputtering takes place in an argon atmosphere of a pressure around 5 mTorr.

The sputter plasma is created with a constant power-regulated DC source and proceeds in two stages. The first stage is a clean of the target. This is done at a power of 200 W and lasts two minutes. During this time there is a shutter between the wafer and the target to prevent deposition. The deposition phase takes place at 110 W and proceeds until the desired thickness has been achieved. With these parameters, the deposition rate is 8 nm/min. The wafer is always rotating to ensure a uniform deposition over the wafer.

The thickness for the base layer is normally chosen to be 80 nm, while we use 100 nm for the counterelectrode. The base is thin and the counterelectrode thick to promote good step coverage.

A.3.3 Positive lithography

The first step in lithography is cleaning the wafer surface of large particles and other contamination. This is done by mounting the wafer on the chuck in the wafer spinner and spinning the wafer to 3000 rpm. Once spinning, the wafer is sprayed with acetone and then IPA and blown dry with nitrogen.

Next the photoresist is droppered onto the wafer. In our positive process, we use Shipley Microposit SPR955. The resist is spun at 3000 rpm for 30 s and then rapidly transferred to a hot plate for a 95° C pre-bake for 60 s.

The wafer is then transferred into the input holder of the wafer stepper for exposure of the pattern for the appropriate layer. The exposure dose on this machine is specified by a time; we find best results with an exposure around 240 ms. Alignment of the layers is automatic.

The next step is a post-bake of 60 s at 110° C, followed by development. The developer is MF-24A and the wafer is suspended resist-side down, held in a Teflon tripod, and gently agitated for 60 s. The developer does etch aluminum at a low rate, sufficient to etch 10-20 nm after the resist is developed away in the early areas. After the develop is complete, the wafer is transfered to a water rinse beaker, where it is allowed to soak for another $\sim$ 60 s. Once sufficiently rinsed, the wafer is blown dry by a stream of dry nitrogen.

A.3.4 Negative lithography

Negative lithography is similar to positive lithography apart from a few details. The negative resist is used for liftoff because the exposure and reversal results in an undercut which assists the solvent in removing the resist in a later step. The clean process is the same, but the resist used is AZ-5214, which is spun at a faster rate of 4000 rpm. The pre-bake is again 60 s at 95° C, and then the wafer is exposed, but the exposure is shorter for the thinner resist, with an optimal time of 75 ms.

Following the post-bake at 110° C for 60 s, there is an additional step. The post-bake is the step where the reversal takes place, hardening the exposed areas and softening the unexposed areas. In order to complete that process, the wafer is flood-exposed with UV light at a contact aligner for 60 s. Then the wafer is developed for 45 s, rinsed, and dried.

A.3.5 Wet etch

We use a wet etch process to define features in our aluminum films. A wet etch is fast and gives a very isotropic etch, which results in nicely sloped edges that make step coverage of future layers more reliable. The etching solution is a commercial acid, Transene A. It is prepared at an elevated temperature of 45° C. The wafer is etched pattern-up, suspended by the Teflon tripod. The pattern is up so that the etch can be visually monitored and stopped when the etch is complete. For a 100 nm film, this usually takes $\sim$ 20 s.

The wafer is then removed and quickly rinsed in a running stream of deionized water. The wafer is kept in the stream for $\sim$ 60 s to remove any trace of acid and then blown dry by a stream of dry nitrogen.

Finally, if the pattern is determined to be acceptable, the resist is stripped. This is done by immersing the wafer pattern down in a beaker of acetone and sonicating at a moderate power for 5 minutes. After sonication, the wafer is removed from the acetone, sprayed with IPA, and blown dry with nitrogen.

A.3.6 Dry etch

Dry etch, otherwise known as reactive ion etch (RIE), is a plasma etch that uses the reaction of the material with other chemical species to remove the material in a controlled way. We use RIE to etch dielectrics using CHF_3.

RIE can result in very anisotropic etch profiles, which can be difficult to cover with the next layer. One approach to get sloped sidewalls is to optimize the gas flows to have a similar etch rate in photoresist and the dielectric. In this way, the slope of the resist is transferred to the dielectric and the problem of having a sloped sidewall becomes one of having sloped resist. A sloped resist is accomplished by an extra bake of the resist after it has been developed. The bake at a high temperature (120° C) for a relatively long time (3

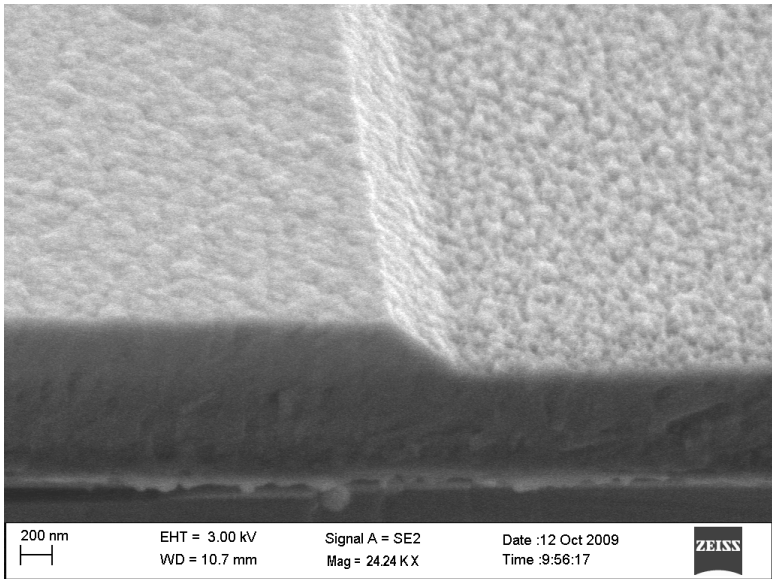

Figure A.2: SEM image of the etch profile on SiO_2 after 120° C, 3 min bake to flow the resist.

min) flows the resist a little bit, and surface tension creates a sloped profile near the edge of the pattern.

For these processes, we have seen better results using a graphite platen to set the wafer on in the chamber instead of the more common aluminum platen. Thus, the process begins by changing the platen and doing a 5 minute chamber clean using the standard O_2 process.

Next, the chamber is vented and the wafer is placed in the middle of the platen for etching. The process for nitride and oxide is the same. The active compound is CHF_3 flowing at 50 sccm. The process also contains O_2 flowing at 20 sccm. The gases are regulated to a pressure of 100 mTorr and the RF power is 150 W. The etch rate for SiO_x is ∼30 nm/min, and the etch rate for SiNx is ∼60 nm/min. Significant overetch is tolerable because the underlying aluminum has a negligible etch rate; thus, to ensure the 120 nm films are completely etched, the time for a SiO_x wafer is set to 7.5 min, and for the SiNx wafer, the time is 2.5 min.

After the wafer is etched, the resist must be cleaned. For the short etch, this is easily done with a 5 minute acetone and ultrasound bath. For the longer etch, the resist is more

difficult to remove. It gets hot during the etch and becomes baked onto the wafer. An effective process is to use the solvent 1165 and soak the wafer in an ultrasound bath for 30 minutes, with repetition if necessary to clean off all of the resist. The final step is the usual IPA spray and nitrogen dry.

A.3.7 PECVD deposition

PECVD stands for plasma enhanced chemical vapor deposition. This is a process where chemical molecules that contain elements of the intended deposition film are excited in a plasma. When they come into contact with a sufficiently hot surface, they react, creating a solid reaction product, which remains, and a gaseous reaction product, which is removed. This is a common way to deposit dielectrics, and we use it for silicon oxide and silicon nitride dielectrics. There is also some physical etching of the substrate during the initial stages of the process, which may play a very important role of cleaning the surface before deposition. The chamber is a Plasmatherm PT70, which has a parallel plate geometry. The film thickness is always nominally 120 nm. These layers are slightly thicker to avoid pinholes and also because they bear the brunt of ion mill cleans.

SiOx

The silicon oxide process has the following gases and flows: 900 sccm N_2O, 400 sccm SiH_4. The total pressure is 900 mTorr, the plasma power is 25 W, and the substrate temperature is 250° C. The deposition rate for this process is 36 nm/min.

SiNx

The silicon nitride process has these gases and flows: 900 sccm N_2, 375 sccm SiH_4, 50 sccm NH_3. The total pressure is 900 mTorr, power is 45 W, and temperature is 250° C. The

deposition rate is 20 nm/min.

A.3.8 Junction oxidation

Junction oxidation takes place in the sputter system so that the counterelectrode can be immediately deposited *in situ*. First, the wafer is ion milled for 45 s to remove the native oxide inside the vias. After that, oxygen is introduced into the system to form the tunnel barrier. Initially, the pumping of the chamber is maintained while a low pressure of oxygen is flowed through the system. This seed step generates 1 mTorr and is held for 2 minutes.

Then the chamber gate valve is closed and the oxygen pressure is allowed to rise to the final oxidation value. When making a SQUID, the target critical current is typically $3-5$ μA, for 2 μm^2 junctions; we get that by oxidizing at a final pressure of 200 mTorr for10 minutes. Finally, the oxygen is quickly pumped out and the counterelectrode is sputtered as soon as possible. The wafer does not rotate during the oxidation process.

A.3.9 Normal metal evaporation

A non-superconducting material is needed to make junction shunt resistors. This process uses palladium, with a thin titanium adhesion layer. These metals are deposited by electron beam evaporation. This is a process whereby a metal is heated in a vacuum by an electron beam to the point where the hottest atoms have enough energy to leave the bulk metal, and they fly off through the vacuum, coating everything within line of sight, including the wafer.

The evaporation process is very easy to monitor because film thickness is tracked by a quartz crystal monitor. As metal is deposited on the monitor, the resonant frequency of the crystal changes. The system tracks the changes in the frequency and provides a thickness at the location of the wafer with the aid of a separately calibrated tooling factor. Using this method, we deposit 3 nm of Ti for an adhesion layer, followed by whatever thickness of Pd is

required to create the resistance that is desired to keep the SQUID non-hysteretic, typically 15-50 nm.

Our palladium deposited in this way has a room temperature resistance, for a thickness of 50 nm, of $\sim 5\ \Omega/\square$. At low temperature, the resistance decreases. Because the SQUID is operating at low temperature, it is important to know what the resistance is at low temperature. RRR is thickness-dependent due to boundary scattering, and for the thicknesses employed here, RRR is in the range from 2.0-2.5.

A.3.10 Liftoff

The liftoff step is a step that removes metal from the surface of the wafer. The previous steps have created a negative pattern of resist on the surface of the wafer and deposited metal over the entire surface. Now, the resist is removed and any metal on top of resist is removed with it, or lifted off. The wafer is suspended pattern-down in a solvent, in our case acetone, for a period of time necessary to remove all the undesired metal, typically $\sim$1 hr. Any remaining resist is removed by a quick $\sim$10 s ultrasound treatment. Finally, the wafer is removed, sprayed with IPA, and blown dry with nitrogen.

A.4 Fabrication Process

With the steps defined above, the fabrication process can be described as follows:

1. Start with an oxidized silicon wafer. To use the silicon oxide as the bottom encapsulation, continue with the process. To use silicon nitride, first strip the silicon oxide in an HF bath and then quickly transfer to the PECVD chamber and deposit SiNx.

2. Sputter the aluminum base layer.

3. Pattern and wet etch the base pattern.

4. Deposit the upper dielectric with PECVD, either nitride or oxide.
5. Photolithographically pattern the vias.
6. Etch the vias using the dry etch process.
7. Transfer the wafer into the sputter system again to oxidize the junctions, and deposit the aluminum counterelectrode immediately thereafter.
8. Pattern and wet etch the aluminum layer with the counterelectrode pattern.
9. Probe the newly formed junctions to estimate their critical current and decide on a resistor thickness to engineer $\beta_c \leq 1$.
10. Pattern a negative resist layer to prepare for liftoff of the resistor material.
11. Evaporate palladium to the desired thickness.
12. Liftoff the resistor film. The devices are now complete.

All that remains is to dice the wafer and mount the chips for measurement.

Bibliography

[1] M. Ketchen and J. Jaycox, Appl. Phys. Lett. **40**, 736 (1982).

[2] A. Kleinsasser, R. Miller, and W. Mallison, Applied Superconductivity, IEEE Transactions on **5**, 26 (1995).

[3] V. Ambegaokar and A. Baratoff, Phys. Rev. Lett. **10**, 486 (1963).

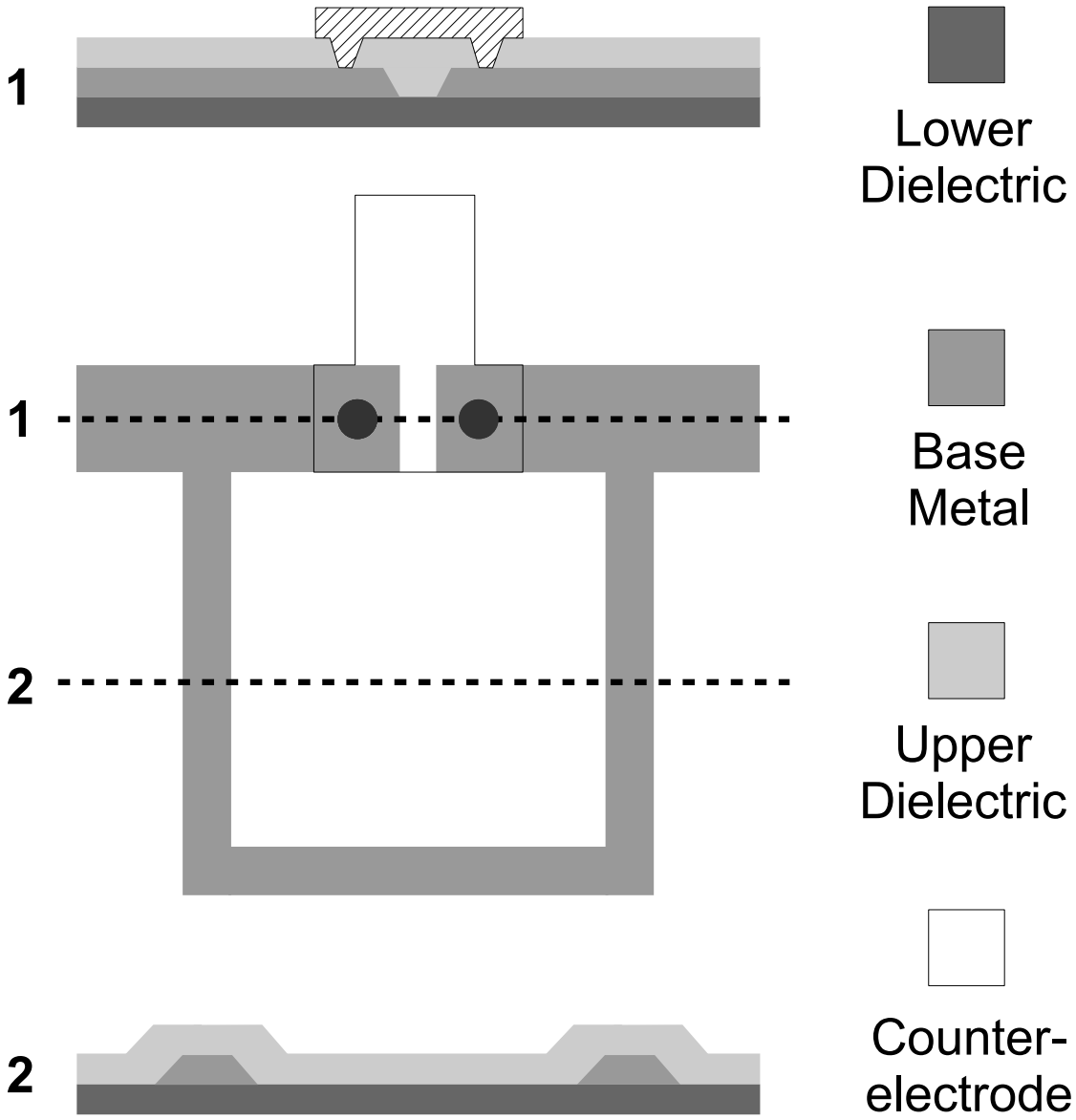

Figure A.3: SQUID Layout. Line cut (1) shows the layer stack profile through the junctions. Line cut (2) shows the layer profile through the SQUID loop.

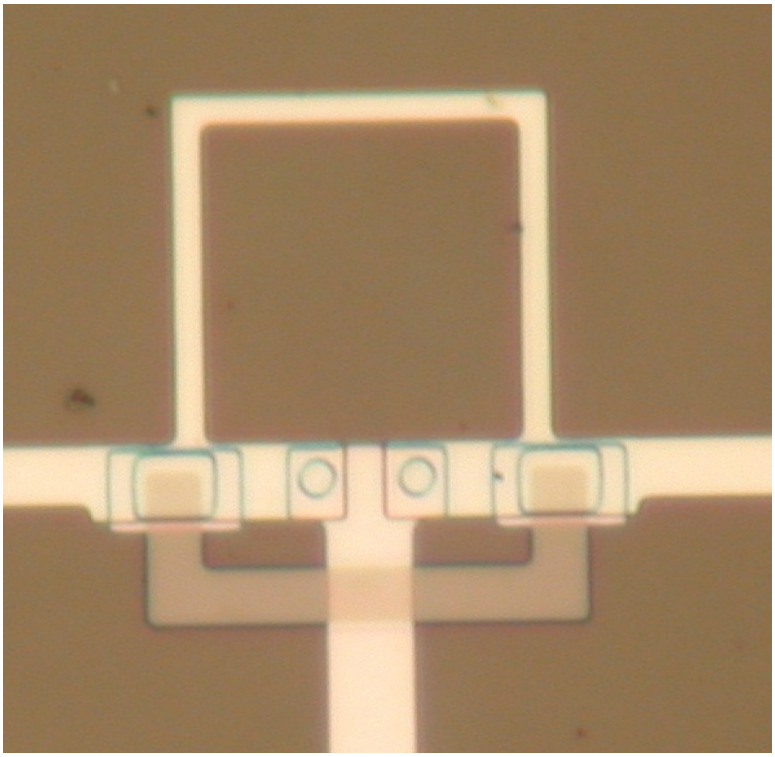

Figure A.4: SQUID optical image of a finished small narrow line device.